UNIVERSIDAD POLITECNICA DE VALENCIA

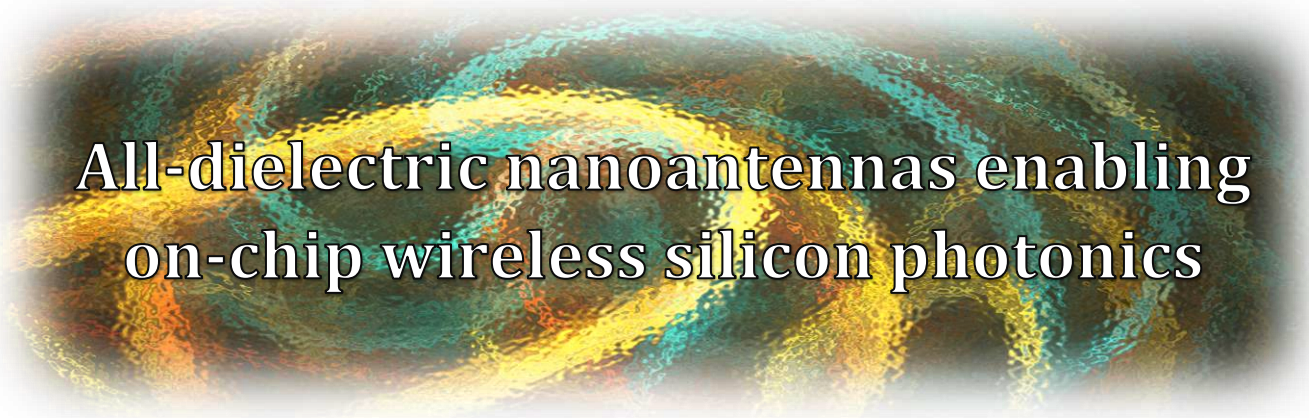

All-dielectric nanoantennas enabling on-chip wireless silicon photonics

Sergio Lechago Buendía

Supervisors: Carlos García Meca and Javier Martí

Doctoral thesis

Submitted for the degree of
Doctor of Philosophy in Telecommunication Engineering

Valencia, October 2019

CONTENTS

Objectives and structure of the thesis

1. Introduction 1

1.1 Silicon Photonics Framework 1

1.2 Advantages of on-chip wireless silicon photonics vs wired-based photonics 4

1.3 Engineering high-performance on-chip optical antennas 8

1.3.1 Efficient interfacing to plasmonic systems 10

2. Fundamentals of antenna design and fabrication 13

2.1 Antenna main parameters 13

2.2 Open-end waveguides enabling on-chip optical antennas 17

2.3 Reconfigurability and beam-shaping capacities 20

2.4 Fabrication overview 22

3. Our original contributions 27

PAPER A 29

PAPER B 63

PAPER C 81

4. General discussion and conclusions 101

Bibliography 105

Acknowledgement

First, I would like to say that I consider this thesis as a choral work that has been possible thanks to the close collaboration of many people. I want to express my utmost gratitude to my supervisors, Carlos and Javier. I perfectly remember how Javier gave me the chance to join the NTC team after having an informal interview with him several years ago. Since the very beginning, he trusted me, gave me responsibilities, guided me and provided the master lines that shaped the shell of this work, which could not be understood without his baton and global view. Thanks for showing and offering me the world of science, Javier. With respect to Carlos, I consider that he represents the best principles of a researcher: knowledge, excellence, preciseness and humbleness. This work would not be possible without his extreme creativity, sacrifice and guidance through all these years. These outstanding features that define him as a vocational science man are even irrelevant, if compared with his principles as human being, for all these reasons thanks for guiding me but above all, thanks for being my friend.

The applied spirit of this thesis was supported thanks to the NTC fabrication team lead by good friends Amadeu and Jose Ayúcar, thank you so much. I do not even have enough words to express my gratitude to all of them. A special mention deserve my partners from the 'sala diáfana'… Luis, Marghe, Álvaro, Pau, Andrés, Fran, Anita, Julito, Mario, Alba, Ángela, Kike, Diego, Raffaele, Sara, Nuria, Antoine, Elena, Javi, Alex, Pak, Jesús, Rubén… They have become like a second family for me, moving from workmates to become close friends… Thanks for giving me the opportunity to enjoy the best period of my life with all of you. Additionally, I want to show my gratitude to the 3 reviewers of this dissertation: Andrea Alù, José Manuel Taboada and Jorge Bravo. Their positive comments highlighting the strengths of this work have definitely encouraged us to keep working with a renewed energy in the quest of expanding the scientific goals here achieved. Finally, I want to thank the 3 members of my examining board, Borja Vidal, Andreas Håkansson and José Manuel Taboada, since they will have the deference to make time for attending and evaluating the defense of this dissertation.

Quiero terminar estos agradecimientos dedicando unas palabras en español a mi familia. Gracias a mis padres, Concha y Paco, por inculcarme los valores de la responsabilidad y la honestidad tanto en el trabajo como en la vida y a mis hermanos, Paco y Eugenio, por haberme cuidado y guiado en todas las fases de mi vida.

Gracias Marta, por ser lo mejor de mi vida, por ser amable, dulce y comprensiva, por todos tus sacrificios durante todos estos años y por haber hecho que ahora compartamos lo más bello que pueden compartir un hombre y una mujer que se aman… Nuestro hijo Sergio, un beso para ti, principito, por haber hecho que nuestra vida sea aún más plena.

Resumen

La revolución posibilitada por las aplicaciones fotónicas durante las últimas décadas ha dejado su impronta en la sociedad tal y como la conocemos actualmente. Ejemplos claros de este impacto están patentes en, por ejemplo, el enorme tráfico de datos generado por el uso de Internet o el empleo extendido de algunas técnicas biomédicas con fines diagnósticos o quirúrgicos, que no podrían entenderse sin el incesante desarrollo de los sistemas ópticos. La necesidad de combinar y miniaturizar estos sistemas para generar funcionalidades más avanzadas dio lugar al nacimiento de los circuitos fotónicos integrados (PICs), que es donde esta tesis comenzó a tomar forma. En este sentido, observamos limitaciones en términos de flexibilidad o reconfigurabilidad inherentes a la naturaleza guiada de la mayoría de los PICs realizados hasta el momento. En el caso de circuitos plasmónicos, observamos también limitaciones por las pérdidas que tienen las guías metálicas a altas frecuencias. La inclusión de estructuras inalámbricas (basadas principalmente en nanoantenas plasmónicas) en la capa fotónica surgió para mitigar estas pérdidas, abriendo también nuevas vías de investigación. Sin embargo, estos dispositivos aún presentaban rendimientos muy pobres como elementos puramente radiantes en el régimen de campo lejano. Para superar estas deficiencias, en este trabajo, introdujimos un enfoque novedoso en el desarrollo de dispositivos inalámbricos en la nanoescala, que dio forma a lo que llamamos *on-chip wireless silicon photonics*.

Este nuevo concepto se apoyó en el uso de nanoantenas de silicio compatibles con procesos CMOS, que constituyen las estructuras clave que posibilitan un vasto catálogo de aplicaciones en redes fotónicas de comunicación o en sensores ultra-integrados, así como para la interconexión de sistemas dieléctricos-plasmónicos avanzados. En el ámbito de las comunicaciones, gracias a las sencillas reglas de diseño para adaptar la directividad de estas nanoantenas a diversas aplicaciones, pudimos demostrar por primera vez transmisiones inalámbricas de datos (mediante el uso de antenas altamente directivas) en redes *on-chip* reconfigurables o desarrollar dispositivos para generar a voluntad focos electromagnéticos de manera dinámica en espacios bidimensionales (gracias a antenas con una directividad más baja). Por otro lado, en el campo del biosensado, diseñamos y fabricamos un dispositivo lab-on-a-chip para la identificación de micropartículas, basado en el uso de antenas dieléctricas –presentando un rendimiento equiparable a los mejores diseños desarrollados hasta el momento– que incluye el subsistema óptico más compacto demostrado hasta la fecha. Finalmente, fuimos capaces de conectar experimentalmente y de manera eficiente antenas basadas en silicio con estructuras plasmónicas para el desarrollo de nuevas aplicaciones en la nanoescala, aunando las ventajas del *on-chip wireles silicon photonics* para comunicaciones en chip, conformación dinámica de haces o biosensado con las ventajas de la plasmónica para la manipulación e interacción con luz.

Resum

La revolució habilitada per les aplicacions fotòniques durant les últimes dècades ha deixat la seua empremta en la societat actual tal com la coneixem. Exemples clars d'aquest impacte estan patents en, per exemple, l'enorme tràfic de dades generat per l'ús d'Internet o d'algunes tècniques biomèdiques amb fins diagnòstics o quirúrgics, que no es podrien entendre sense l'incessant desenvolupament dels sistemes òptics. La necessitat de combinar i miniaturitzar aquests sistemes per produir funcionalitats més avançades va donar lloc al naixement dels circuits fotònics integrats (PICs), que és on aquesta tesi va començar a prendre forma. En aquest sentit, observem limitacions en termes de flexibilitat o reconfigurabilitat inherents a la naturalesa guiada de la majoria dels PICs realitzats fins al moment. En el circuits plasmònics, tenim a mès les limitacions de les elevades pèrdues que les guies metàl·liques tenen a altes freqüències. La inclusió d'estructures sense fil (basades principalment en l'ús de nanoantenes plasmòniques) a la capa fotònica va sorgir per mitigar aquestes pèrdues, obrint també noves vies d'investigació. No obstant això, aquests dispositius encara presentaven rendiments molt pobres com a elements purament radiants en el règim de camp llunyà. Per superar aquestes deficiències, en aquest treball, vam introduir un enfocament innovador en el desenvolupament de dispositius sense fil a la nanoescala, que va donar forma al que anomenem *on-chip wireless silicon photonics*.

Aquest nou concepte està basat en l'ús de nanoantenes de silici compatibles amb processos CMOS, que constitueixen les estructures clau que possibiliten un vast catàleg d'aplicacions en xarxes fotòniques de comunicació o en sensors ultra-integrats, així com per a la interconnexió de sistemes dieléctrics-plasmònics avançats. En l'àmbit de les comunicacions, gràcies a les senzilles regles de disseny per adaptar la directivitat de les antenes a les diverses aplicacions, vam poder demostrar per primera vegada transmissions de dades *on-chip* (mitjançant l'ús d'antenes altament directives) en xarxes reconfigurables o desenvolupar un dispositiu per generar a voluntat focus electromagnètics de manera dinàmica en espais bidimensionals (gràcies a antenes amb una directivitat més baixa). D'altra banda, en el camp del biosensing, vam dissenyar i fabricar un sensor lab-on-a-chip per a la classificació de micropartícules, basat en l'emprament d'antenes dielèctriques amb un rendiment a l'avantguarda dels millors dispositius de l'estat de l'art, que inclou el subsistema òptic més compacte demostrat fins al moment. Finalment, vam ser capaços de connectar experimentalment i de manera eficient antenes basades en silici amb estructures plasmònics per al desenvolupament de noves aplicacions en la nanoescala, unint els avantatges del on-chip wireless silicon photonics per a comunicacions en xip, conformació dinàmica de feixos o biosensat amb els avantatges de la plasmònica per a la manipulació e interacció amb llum.

Abstract

The revolution sparked by photonic applications during the last decades has made its mark in society, as we currently know it. Clear examples of this impact are patent in, for instance, the colossal worldwide data traffic generated by the use of the Internet or the widespread utilization of some biomedical techniques for diagnostic or surgical purposes, which could not be understood without the ceaseless development of optical systems. The necessity of combining and miniaturizing these systems to enable advanced functionalities gave birth to the development of photonic integrated circuits (PICs), which is the main framework within which this thesis began to take shape. Along these lines, we noticed restricted limitations in terms of flexibility or reconfigurability inherent to the wired-based nature of most PIC implementations carried out so far. In the case of plasmonic circuitry, there are additional shortcomings arising from the prohibitive losses of metallic waveguides at very high frequencies. The inclusion of wireless structures (mostly based on plasmonic nanoantennas) at the photonic layer emerged to mitigate these limiting losses, also opening new research avenues. However, these devices still presented poor performances as purely radiating elements in the far-field regime. In order to overcome these lacks, in this work, we introduced a novel version to wireless approaches at the nanoscale in what we called *on-chip wireless silicon photonics*.

This new concept was built upon the use of CMOS-compatible silicon-based nanoantennas, which constitute the key enabling structures of a diverse catalogue of applications in photonic communication networks or ultra-integrated sensors as well as for interfacing advanced dielectric-plasmonic systems. In the scope of communications, thanks to the easiness to tailor the antenna directivity, we were able to experimentally demonstrate on-chip data transmission flows in reconfigurable networks for the first time (by using highly directive antennas) or to develop dynamically tailor-made interference patterns to create focused spots at will on a 2D arrangement (enabled by antennas with a lower directivity). On the other hand, in the field of biosensing, we experimentally implemented a dielectric antenna-based lab-on-a-chip device for microparticle classification with state-of-the-art performance, which included the most compact optical subsystem demonstrated so far. Finally, we were able to efficiently interface silicon-based antennas to plasmonic systems to develop new advanced functionalities at the nanoscale, by putting together the advantages of on-chip wireless silicon photonics for on-chip communications, beam-shaping tailoring or lab-on-a-chip sensing with the advantages of plasmonics for light concentration and manipulation.

Objectives and structure of the thesis

Nanophotonics [1] has become a key enabling technology since the mid-1980's to the present day, gearing up for numerous applications such as high-performance computing (HPC) [2], high-speed on-chip interconnects [3–6] and lab-on-a-chip sensors [7], amongst many others. The stamp of these outstanding applications is clearly patent in several areas ranging from medicine and biotechnology to aerospace. On this matter, conventional electronic technology has undergone a revolution during the last decades thanks to the emergence of photonic circuits, whose combination at the nanoscale gave birth to the so-called photonic integrated circuits (PICs), which are able to offer a disruptive performance in terms of speed, bandwidth or energy consumption [1]. However, exploring the literature related to PICs, we discovered that these devices are typically based on the use of guided-based interconnects, feature which definitely hampers the network-on-chip flexibility and reconfigurability, while additionally showing complex topologies and large footprints [8, 9]. Furthermore, a monolithic and pre-established waveguide-based layout limits or directly hinders the interaction of this kind of architecture with the outer medium at far-field distances to enable, for instance, different types of sensors and devices [10, 11], as well as applications related to microparticle control and acceleration (tweezing, sorting…) [12–14]. Clearly, moving away from conventional guided photonics is necessary to satisfy the requirements of some of the aforementioned applications as well as to boost the development of new functionalities in several scientific areas. The emergence of wireless devices at the nanoscale, mostly based on the use of plasmonic nanoantennas [15–25], arose as a solution to overcome the stringent limitations in terms of losses of metallic wired-based architectures, while in parallel opening new possibilities in the design of more flexible on-chip systems [23, 25], potentially fulfilling the requirements of the applications aforementioned. Despite the fact that plasmonic nanoantennas overcome the performance of their wired counterparts, they still render poor figures of radiation efficiency or directivity, well known parameters that determine the reach of any antenna. Other wireless approaches with better radiation capacities have been proposed, usually based on the use of dielectric nanoparticles [26,

27] or grating couplers [28–30]; the former being difficult to be experimentally implemented and the latter being more suited for off-chip radiation while usually exhibiting large footprints.

In the quest of overcoming the diverse limitations previously mentioned is how this dissertation was outlined, aiming to provide a novel standpoint change in the field of on-chip PICs. With this objective in mind, we engineered well-known silicon photonic wires, transforming them into high-performance on-chip integrated antennas. Thanks to these key enabling devices, we were able to experimentally demonstrate a vast number of applications – hardly manageable via waveguide-based architectures or by previous wireless schemes– in the frame of what we called *on-chip wireless silicon photonics*. The potential of this approach was showcased with the implementation of reconfigurable switching networks, lab-on-a-chip biosensors or efficient interfaces to plasmonic devices, proving their direct impact on nanoscale communications or ultra-integrated biosensing. With this new wireless platform, we have paved the path for a novel scenario in photonic integrated circuitry, which not actually supersedes wire-based schemes but supplements them in a synergistic way in order to open up radically new fields of applications in nanotechnology and nano-optics. Notably, in this thesis, we have had the chance to directly participate in every stage of the research process, including the development of the theory, the design of the different structures, the *in situ* fabrication process in a clean room and the experimental characterization of the different devices.

Concerning the structure of this dissertation, it was conceived as a collection of papers. Chapter 1 provides a brief introduction that puts into context the current state of the art of silicon photonics together with a motivation of the work carried out throughout this work, highlighting the necessity of incorporating wireless devices into the photonic layer and its main advantages versus wired-based schemes. Chapter 2 outlines the fundamentals that support the working principles of the proposed silicon nanoantennas, describes the main antenna radiation parameters and briefly sketches the main fabrication processes carried out in the experimental applications. In Chapter 3, after a succinct introduction of the main results, we directly include the three main papers that shape this thesis. In this sense, this chapter has been written as a self-contained piece that might be straightforwardly consulted by the reader without the necessity of reading previous chapters. In any case, in order to acquire an initial background and understanding of the global work here performed, we encourage those readers unfamiliar to the dissertation topic to explore this text sequentially, starting from the first chapter. Finally, Chapter 4 assesses the main results shown in Chapter 3 and examines the new possibilities and challenges set out in the scope of on-chip wireless silicon photonics.

Chapter 1
Introduction

1.1 Silicon Photonics Framework

Current technological advances in communications, energy, life sciences, aerospace or the widespread use of the Internet could not be understood without the discovery of the transistor in 1947, which has been the cornerstone of the ceaseless exponential growth of electronics and its applications since the second half of the 20th century. Nowadays, fulfilling the necessities of society in most of the aforementioned fields involves demanding applications, supported by increasingly complex integrated architectures and layouts. As predicted by Moore's law [31], the number of transistors on a single chip would double every two years, a well sustained rule that has enabled unprecedented and improved transistor performance and integration densities (allowing dramatically reduced footprints). However, it is well known that electronics is about to reach unavoidable physical limitations (current transistors below 10 nm are leading to quantum tunneling effects) as a result of this extreme transistor integration. For this reason, current trends are evolving towards a novel concept called "More than Moore" [32], adapting the new processors to satisfy the necessities of the applications that will run in the next generation of computers, smartphones, sensors and other intelligent devices. Instead of increasing the speed of each chip separately, the improvement here sought is to provide new and disruptive functionalities that are massively parallelized over several devices.

Is the microelectronic industry ready to face this challenge? In order to evolve towards this new technological paradigm, the use of photonic interconnects and devices has arisen as a promising option to mitigate this upcoming electronic bottleneck since they might provide a low-loss inexpensive energy-efficient platform with a huge bandwidth and signal stability [33]. Since the mid-1980's we have witnessed a tremendous momentum in the development of photonic applications and systems enabled by the use of silicon as a basic constituent material. This boom

has not just been limited to the research scope, but has also permeated the industrial environment. In this sense, within the European Union, the photonic industry directly employs 300.000 people (with a foresight of reaching 1 million by 2030) in more than 5.000 companies with a global market share higher than 15%, just behind China. Clearly, after more than 30 years of development, silicon photonics is still a burgeoning research spot with a consolidated repercussion in all the branches of life and applied sciences. Furthermore, it is expected that in the next few years, photonics in combination with plasmonics will bridge the gap from current nanoscale systems to future quantum systems [34, 35], opening unprecedented new avenues with the aim of fueling the scientific revolution of the near future.

The emergence of silicon-based photonics can be explained by two main reasons: 1) this group IV semiconductor material is transparent at the optical communication window (1300–1600 nm) and 2) silicon can be straightforwardly integrated in CMOS-like fabrication techniques for a low-cost mass production. More in depth, the pioneering work of Soref [36, 37] in the second half of the 1980's, demonstrated that light can be driven within Si-waveguides, thus opening the door to the implementation of multiple photonic devices such as switches or modulators [38–45]. From an industrial point of view and taking advantage of the well-established use of silicon in microelectronics, this material was proposed as an alternative for photonics mass production [46–51] due to its capacity for a high level of integration and low assembly costs (if compared to other group III-V semiconductors). Moreover, the high refractive index contrast existing between silicon and silicon dioxide (the typical insulator employed in silicon-based wafers), enables strong light confinement via total internal reflection in optical wires; feature which allows the implementation of these structures with sub-wavelength dimensions (in the nanometer scale). Thanks to this standard –the well-known silicon-on-insulator (SOI) platform– light can be driven within silicon waveguides, enabling interconnects with cross sections less than 0.125 μm^2 at telecom wavelengths (in contrast to standard single mode optical fibers with core cross sections surpassing 80 μm^2). Consequently, this reduced size allows the realization of highly-integrated photonic devices. Thanks to these features, it was demonstrated that silicon photonics could play a main role not only in long-distance optical communications (via by the widespread use of optical fibers), but also in the development of current photonic integrated circuits [52]. These components have emerged as crucial elements in current high-performance computers and data centers, on-chip optical networks, biochips and ultra-fast, ultra-compact, low-consumption optical signal processing devices. A PIC usually consists of different parts as for instance, laser sources, photodetectors and active components such as modulators and switches in charge of performing the optical processing of the information. In recent years, a strong investment in research and development has been made with the aim of improving the performance of each of the above-mentioned components by taking into account and emphasizing the next aspects:

- Losses and energy efficiency (the energy consumption of optical links must be less than that of their electronic counterparts).
- Integration density (potentially allowing for ultra-fast data streams close to Pbits·s^{-1} per chip by the end of the third decade of the century).
- Bandwidth (PICs must be able to operate in a large region of the spectrum to allow the above-mentioned ultra-high communication speeds).
- Material / technology (integrating the photonic layer into the electronic chip and using silicon together with group III/V materials (*e.g.* InP) to enable laser sources and photodetectors on the same silicon layer).

However, the techniques used for this improvement usually arise from the premise that the transport of light into the chip takes place in a guided way. Hence, most functionalities and devices are implemented through the combination of a few basic elements such as waveguides, bends, resonant rings [53, 54], crosses [55, 56] or couplers [57, 58] between different structures. While it is possible to slowly optimize the performance of PIC blocks by improving these basic structures and how they are combined, new approaches are needed if radical advances are to be made, as many of these devices still have shortages such as their large size or reduced bandwidth. In addition to optical communications, there is an increasing number of applications (namely, new lab-on-a-chip (LOC) biodevices and systems [59–63], as well as other applications requiring free-space radiation) that demand a high degree of control over the electromagnetic fields inside the chip that cannot be addressed via waveguide-based elements.

How can we make the next generation of PICs provide advanced functionalities in order to satisfy the aforementioned applications? What we propose in this thesis, as explained in the previous section, is changing the basic PIC building blocks without changing the underlying silicon photonics platform and fundamental fabrication processes. Specifically, we will illustrate the considerable advantages of incorporating wireless silicon devices (nanoantennas) as main building blocks to enable new functionalities out of the reach of typical waveguide-based photonics. Using this approach, new nanoantenna-based applications for CMOS-compatible reconfigurable networks and LOC biodevices will be demonstrated in the frame of what we called *on-chip wireless silicon photonics* [64–66]. Finally, we will show that via the use of smartly-engineered silicon-based nanoantennas we can implement efficient interfaces for plasmonic systems [66], bringing together the advantages of high-performance wireless schemes for long-reach on-chip reconfigurable communications, beam-shaping tailoring or LOC sensors, with the advantages of plasmonic structures for nanoscale light harnessing and manipulation.

1.2 Advantages of on-chip wireless silicon photonics vs wired-based photonics

During the last century, radiofrequency and microwave antenna technologies have enabled countless unprecedented applications (cellular and satellite communications, radar, biomedical imaging…). Similarly, being able to manipulate and radiate electromagnetic fields within a chip in a controlled manner would allow us to beat many of the limitations of current PIC technology, as well as to open the door to a wide range of new functionalities. Building on a new concept of silicon optical antennas (CMOS-compatible), we will show the feasibility of the devised model of on-chip wireless platform and the crucial advantages they provide. Obviously, there are particular functionalities for which guided photonics will always outperform wireless solutions. However, the opposite is also true in many situations. Hence, in this work, we are not pursuing to supersede wired-based photonics, but to synergistically combine the best of both worlds, showing that this combination is far superior to the use of the current guided approach alone. In the next lines, the main advantages that wireless schemes can provide to the photonic layer are summarized.

- **Reduced footprint:** As shown in Chapter 3, our designs have the potential to provide a reduction of up to one order of magnitude in certain communication applications and up to four orders of magnitude in some kinds of LOC devices with respect to previous approaches found in the literature (see PAPER A and PAPER B). The following reasons are behind this crucial advantage over waveguide-based solutions:

  - **Superposition principle:** In free space, infinitely many light beams can cross at the same position without perturbing each other. This brings us the possibility of implementing unguided crossings in many different configurations without perturbing the beam propagation or adding any undesired crosstalk, thus providing a much more flexible optical interconnect architecture. This potential of wireless transmission becomes apparent in complex configurations involving a high number of ports (see Figure 1). In this case, the solution adopted in guided technology consists of a combination of many single crossings, which results in complex topologies requiring a large number of crossings and bends, which yield either a large footprint or high values of crosstalk and insertion loss. Contrariwise, a wireless solution can result in a comparatively improved balance between footprint, crosstalk and insertion loss.

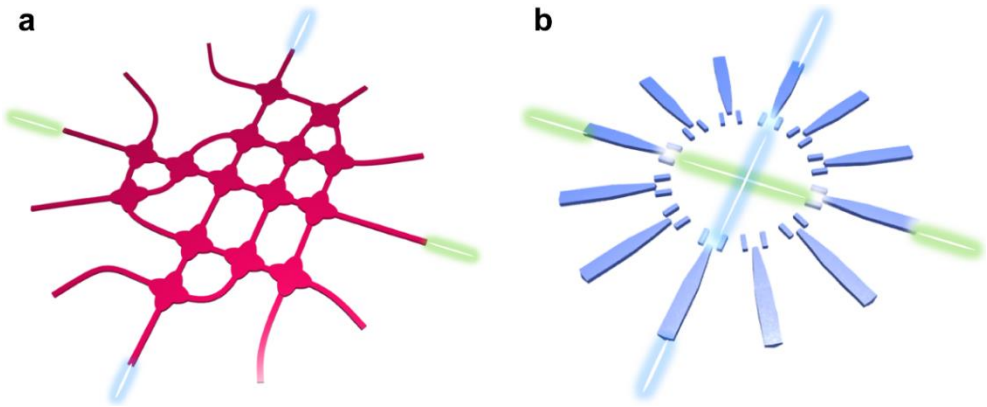

Figure 1. Artwork showing an example of a waveguide-based crossing (a) versus the equivalent wireless alternative proposed in this thesis (b).

- **Multiple signal interference:** Typical structures in integrated photonics are based on the interference of multiple signals. Optical switches are a paradigmatic example. The typical guided approach to this kind of devices is based on cascading basic building blocks that make two signals interfere at a time, to finally achieve the desired multi-signal interference. For instance, 1×*N* switches are constructed by cascading 1×2 switches. The size and complexity of the device rapidly grows with *N*, as $\log_2 N$ stages are required. In a wireless approach, all signals can be made to interfere just in one stage regardless of the value of *N* (with some limitations), greatly simplifying the circuit and reducing the footprint, see Figure 2.

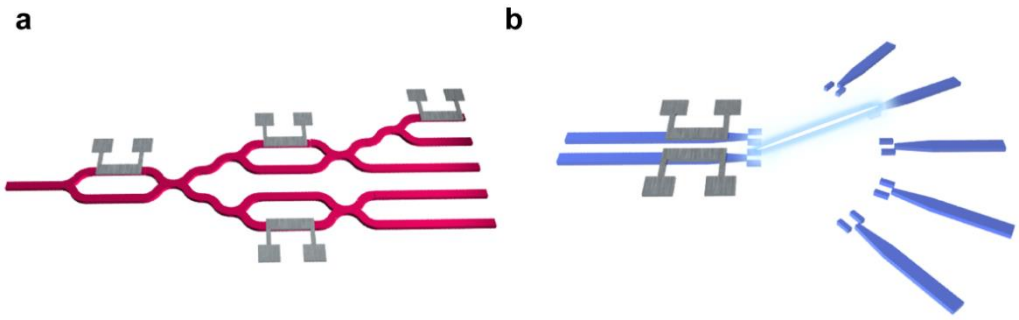

Figure 2. Artwork showing an example of a 1×5 waveguide-based switch requiring 3 stages (a) and a wireless single-stage alternative (b).

- **Seamless integration of light emitters and receivers**: many LOC devices and other on-chip functionalities require illuminating some part of the chip and sampling the scattered light at different positions [60, 63]. This is usually achieved via two different approaches. The first one is based on the use of multiple laser sources and/or optical fibers, as well as other optical elements such as collimators, resulting in bulky devices with potential losses and failure of discrete component interfaces. The second one, relies on the use of focusing components such as lenses or multimode interference devices (in order to achieve a

reduced beam waist and resolve small particles) with a typical lateral size in the mm-scale. The proposed antennas in this thesis (which will be deeply analyzed in the next chapters) can generate low-divergent focused beams with state-of-the-art precision (with a beam full width at half maximum ~1 μm) with dramatically smaller structures (< 0.64×14 μm^2 per antenna).

- **Flexibility, scalability and reduced crosstalk:** as mentioned in the previous point, the exploitation of the superposition principle allows us to reduce the crosstalk [67, 68] in complex interconnect configurations. Considering again the switch example, the guided approach is based on the use of cascaded 1×2 switches, for which crosstalk becomes preponderant and cumulative, swiftly degrading the system performance only after a few stages. Thanks to its single-stage feature, the wireless approach does not suffer from this drawback, yielding lower crosstalk values. It is clear that wireless links provide a more flexible and scalable photonic architecture. Along these lines, increasing by one output a 1×8 switch requires passing from 3 to 4 stages, with a consequent footprint rise and insertion loss. Furthermore, it also augments the unbalance between output ports (unless the number of outputs is a power of 2, the signal will go through a different number of stages depending on the output port in a guided switch), and the crosstalk (due to cumulative errors). However, in the wireless case, passing from 8 to 9 outputs just requires adding one emitting antenna (see Chapter 3, PAPER A), hardly affecting the mentioned features.

- **Extremely simplified fabrication process:** the chip area to be exposed is much smaller as propagation takes place in free space instead of waveguides, which do not need to be created. This implies less energy and time for the fabrication of a given device. Moreover, as we will see in the next chapters, in the wireless approach, the reconfiguration subsystem (*e.g.* to create a switch, usually based on silicon's thermo- or electro-optic effects) can be separated from the photonic subsystem, simplifying the device packaging in comparison to the guided solution (in which both subsystems are interlaced).

- **More robust and compact devices:** long waveguides are a source of fabrication errors. In the wireless approach, waveguides are directly eliminated. On the other hand, in the case of LOC devices, the use of on-chip antennas suppresses the need for bulky external optical elements such as fibers, simplifying the packaging and the automation of the manufacturing process, as well as eliminating the higher potential failure of discrete component interfaces.

- **Performance**: In this dissertation, we show that the silicon on-chip wireless photonic platform enables devices with a reduced *insertion loss* in some specific scenarios (see Chapter 3, PAPER C). Moreover, the aforementioned suppression of external elements such as fibers,

eliminates the higher losses of discrete component interfaces for LOC applications. In terms of *speed*, it is clear that the optical signal travels shorter paths, reaching the device output in less time. Additionally, the reduction in the insertion loss will result in higher allowed data transmission rates. From the point of view of the *energy efficiency*, the reduced required footprint and written area directly imply a reduction in the energy needed to fabricate the photonic structures. Finally, silicon optical antennas can be designed to have an extremely high *bandwidth* (more than one octave at a central wavelength λ of 1.55 μm).

- **Parallelization and system integration complexity:** as mentioned above, many LOC devices require the use of a high number of light emitters and receivers. The absence of large optical elements (whether external, such as optical fibers, or monolithically integrated, such as mm-scale lenses) enabled by the small size of the proposed antennas permits a much higher density of on-chip light emitters and collectors, see Figure 3. This allows, for instance, a finer scattered-field sampling angular resolution, the incorporation of a much larger number of optical instruments operating in parallel in the same chip and the possibility of performing a high number of simultaneous measurements.

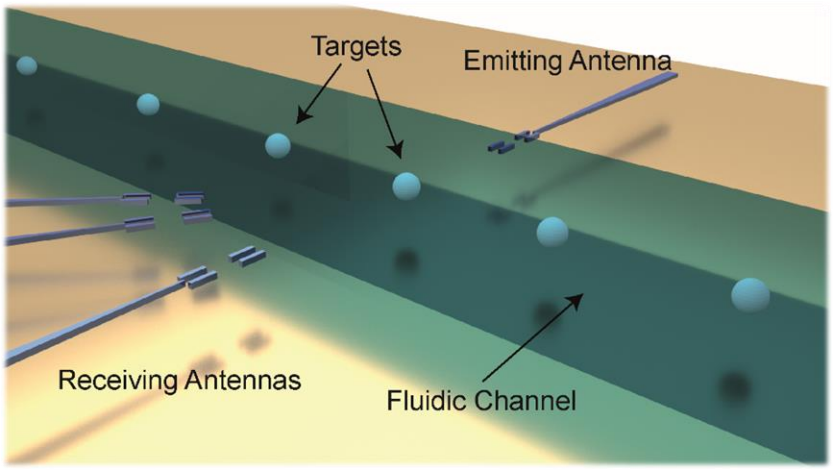

Figure 3. Artwork depicting a LOC sensor where an emitting antenna illuminates a target and the receiving antennas collect the scattered field in several angular directions. The reduced footprint of the proposed wireless devices allows the possibility of increasing the scattering detection area just by increasing the number of receiving antennas.

- **Beam shaping reconfigurable engineering:** As previously outlined in the multiple signal interference point, we demonstrate that by controlling the phase of an emitting nanoantenna array we can tailor custom-made light patterns at will (more details in Chapters 2 and 3). Thus, for instance, we are able to generate on-chip focused light spots with a fully reconfigurable in-plane position. This light spot generator can radiate behind 'obstacles', something not achievable with guided configurations, being insensitive to the presence of any imperfection or defect

between emitter and receiver. This beam-shaping approach opens new possibilities not reachable by waveguide-based schemes (see Chapter 3, PAPER A).

- **New functionalities:** Thanks to the antenna ability to interact with the outer medium at far-field distances, new devices such as dynamic light scattering sensors [11], Raman spectrometers [69] and flow cytometers can be accomplished, as well as applications related to microparticle control and acceleration, among others.

1.3 Engineering high-performance on-chip optical antennas

As already mentioned, the development of on-chip wireless silicon photonics is supported by the use of integrated optical antennas as main building blocks in order to provide new functionalities at the nanoscale. In this sense, the study of nanoantennas –mostly based on plasmonic approaches– is not new, since it has awaken a flourishing interest in the scientific community during the last 15 years. In this work, we considered necessary to provide an alternative to plasmonic nanoantenna designs, which are perfectly suited for applications related to the conversion from localized energy to radiated light [70] but that exhibit poor directivity and high losses, features which hinder their use for practical communication links. In order to overcome these shortcomings, we focused on the classical antenna theory approach (transducing guided to radiated fields and vice versa), studying the performance of typical silicon waveguides (strip- and slot-based approaches) as potentially radiating elements. In this sense, we decided to employ silicon as constituent material due to its low-loss nature and CMOS compatibility.

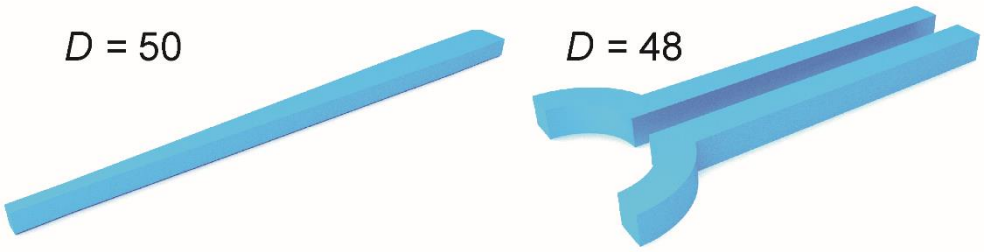

Figure 4. Strip-tapered and slot C-shaped antennas based on previous preliminary implementations of silicon standard wires. These designs already allow directivities of around 50, see Chapter 3, PAPER A and PAPER C for more details.

Using the Huygens' principle [71], we modelled this kind of structures as aperture antennas, in the same way that microwave metallic waveguides are analyzed. This simple approach links directly the radiation pattern of the waveguide with the propagating mode profile

providing simple design rules that surprisingly allow us to tailor the antenna directivity from values as low as 5, from a standard silicon strip waveguide working at λ = 1550 nm, to figures around 50 (linear units) by tapering strip wires or engineering the output facet of slot waveguides, see Figure 4. Moreover, thanks to the inclusion of some additional structures (directors), we were able to further increase the antenna directivity to figures exceeding 100 with a reduced impact in the final footprint of the wireless device (see PAPER A and PAPER C to examine the details in the design of the directors). The wide range of tuneability achieved with our silicon-based antennas was the key element that allowed us accommodating every design to fulfill the requirements of several applications, see Figure 5, not only focusing on communications but also on lab-on-a-chip schemes (see Figure 3).

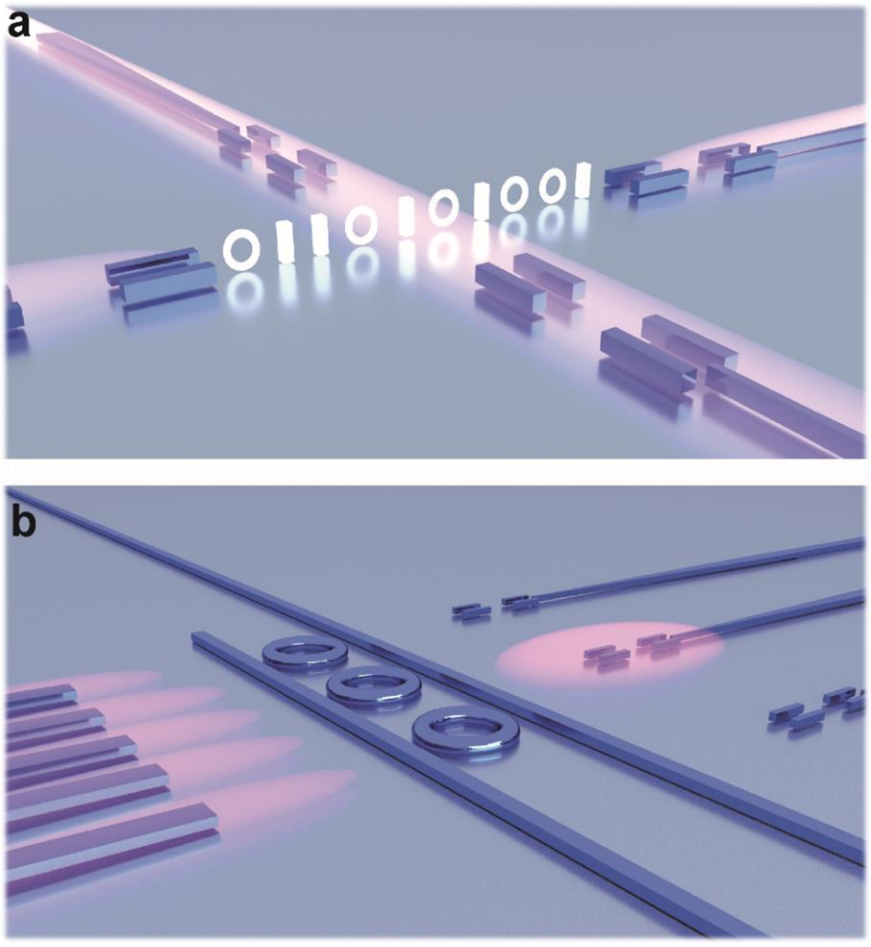

Figure 5. (a) Data transmission scenario where two pairs of antennas (including directors) are transmitting/receiving information. In this case, a high directivity is desirable to minimize the losses in the link. As shown in Chapter 3, PAPER A and PAPER B, a high directivity will be also required for lab-on-a-chip sensing applications. (b) An array of emitting antennas generates a 2D spot able to bridge obstacles in between (in this case, silicon ring resonators as an example) without perturbing their functioning. Unlike scenario (a), here we need less directive antennas to ease the interference patterns of the emitting system (supported on strip wires).

1.3.1 Efficient interfacing to plasmonic systems

The origins of plasmonics [72–77] date back to the first half of the 20th century with the works of Mie [78, 79] and Ritchie [80] on small particle optical scattering and electron beam diffraction at thin metals, respectively. These studies gained importance some decades later, when researchers paid attention to the interesting electromagnetic properties of metal/dielectric interfaces when excited with light. These kind of structures support coherent electron oscillations −known as surface-plasmons (SPs)− that lead to the spatial confinement of the fields in the above-mentioned interface, see Figure 6. Outstandingly, these surface waves exhibit a shorter wavelength than that of the incident light, feature which opened the door to the realization of subwavelength devices and applications at the nanoscale as proposed in [81], where the term 'plasmonics' was officially introduced.

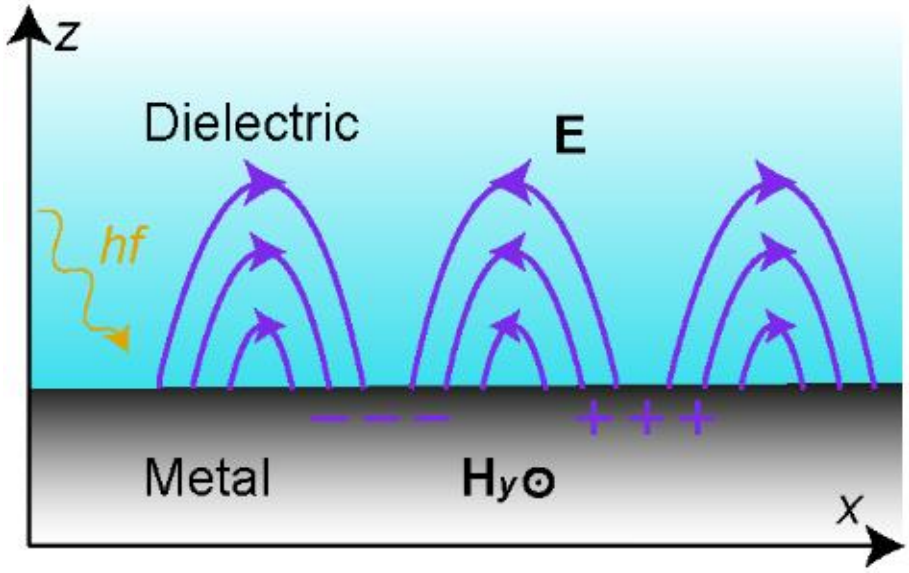

Figure 6. Illustration of the field components of a SP supported by a metal–dielectric interface. The electric field components are normal to the interface (*z*-axis) and propagate along the *x*-direction.

The strong research efforts carried out since the 1980s in the development of nanofabrication techniques such as electron-beam lithography or ion-beam milling as well as of nanocharacterization techniques such as near-field optical microscopy, paved the path towards the experimental implementation of the aforementioned subwavelength optical devices with footprints even below 100 nm. Among them, in the scope of integrated on-chip communications, we can highlight the realization of novel ultra-compact low-cost devices such as modulators, detectors or nanoscale chip sources, which are able to perform at very high operation speeds with low power consumptions [82]. Additionally, plasmonics has also enabled the development of different types of sensors [83, 84], initially based on surface plasmon resonances supported by

continuous interfaces, and later on localized surface plasmons (which arise by confining SPs in subwavelength-sized nanoparticles) [85], with a relevant importance in the field of health sciences. Plasmonics has also contributed to the development of other areas such as spectroscopy [86, 87] or near-field optical microscopy [88]. The outstanding features exhibited at subwavelength regimes to harness and engineer light at the nanoscale together with the different applications that can be realized, have positioned plasmonics as a main player in the current development of nanotechnology.

In this context, we considered necessary to explore the possibility of linking the advantages of on-chip wireless silicon photonics (explained in section 1.2) with all the potential applications and devices that plasmonics offers, thus allowing more advanced functionalities on nano-integrated technology. While it is true that the performance of plasmonic nanoantennas is rather limited in the far-field regime, it is also true that plasmonics, as mentioned above, offers the possibility of developing a vast catalogue of applications in different areas. Along these lines, in the final part of this thesis (see Chapter 3, PAPER C), we employed the acquired knowledge on silicon-based nanoantenna engineering to build up efficient interfaces for plasmonic schemes in the quest of achieving new advanced on-chip systems, see Figure 7.

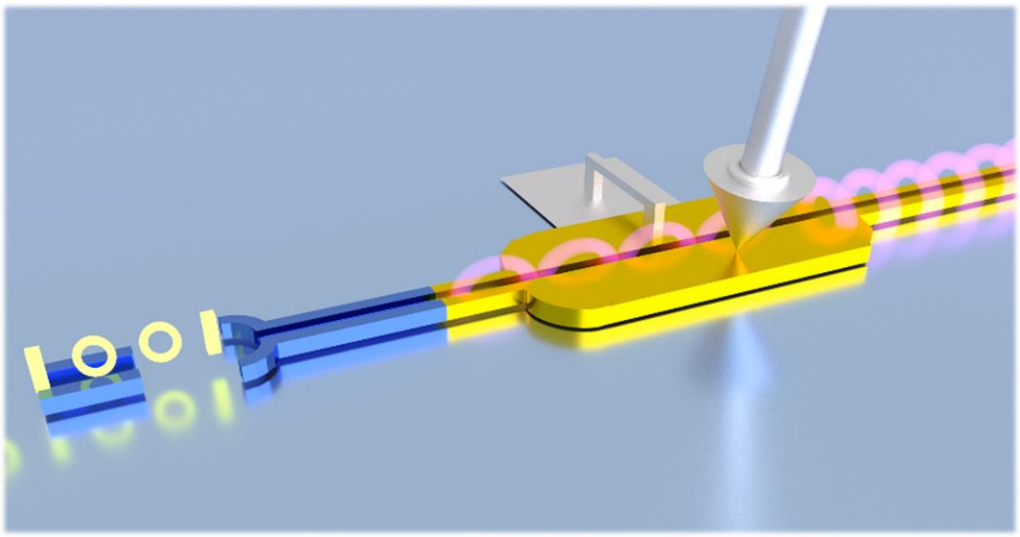

Figure 7. Envisioned scenario where an on-chip silicon antenna is connected to a plasmonic modulator, showing a direct interface between silicon- and plasmonic-based schemes.

Before demonstrating the wide catalogue of on-chip antenna-based applications, covering the areas of on-chip communications, lab-on-a-chip sensing or enabling efficient interfaces for advanced nanoscale systems, we will first introduce the antenna theory together with a brief explanation to their main fundamental radiation parameters. Along these lines, terms such as directivity or impedance matching as well as some others such as gain, radiation diagram or radiation efficiency will be explained in the next chapter.

Chapter 2

Fundamentals of antenna design and fabrication

2.1 Antenna main parameters

In this section, we will briefly define some antenna parameters so that the reader becomes familiar with several important terms often employed throughout this thesis. To this end, we rely on the well-known *145-2013 - IEEE Standard for Definitions of Terms for Antennas* [89] (these definitions are introduced via the use of quotation marks within this section), which provides succinct and clear definitions for "antennas and for systems that incorporate antennas". These terms including directivity, total efficiency or gain amongst others, perfectly describe the operation and radiation capabilities of an antenna and can be also applied to study the performance of on-chip optical antennas.

Directivity

Directivity (D) is defined as "the ratio of the radiation intensity (K) in a given direction of the antenna to the average of the radiation intensity (K_0) in all directions. The average radiation intensity is equal to the total power radiated (P_{RAD}) by the antenna divided by 4π. " This definition can be mathematically expressed as:

$$D(\theta,\varphi) = \frac{K(\theta,\varphi)}{K_0} = 4\pi \frac{K(\theta,\varphi)}{P_{RAD}} \tag{2.1}$$

(where θ and φ are spherical angular coordinates in space). If the direction is not specified, it is understood that the directivity refers to the direction of maximum radiation, which can be expressed as:

$$D = D(\theta,\varphi)\big|_{\max} = \frac{K_{\max}}{K_0} = 4\pi\frac{K_{\max}}{P_{\mathrm{RAD}}} \tag{2.2}$$

Directivity is therefore a measure that only describes the directional properties of the antenna, which are controlled by the radiation diagram (see the definition below). In this sense, an antenna with a low directivity emits approximately the same power in all directions, while an antenna with a high directivity, will radiate more intensively in certain directions.

Radiation diagram

The radiation diagram is defined as "a mathematical function or graphic representation of the radiation properties of the antenna as a function of the coordinated space". This diagram determines the radiation of the antenna in the far-field and is usually represented in polar or angular coordinates. Intuitively, diagrams are best understood by drawing their cross sections in two-dimensional or three-dimensional representations. The radiation property most typically represented is the spatial distribution of the radiated energy, although it is also common practice to represent field diagrams. For example, for ideal isotropic antennas, the radiation pattern is a sphere, and for a typical dipole, it is a toroid, see Figure 8.

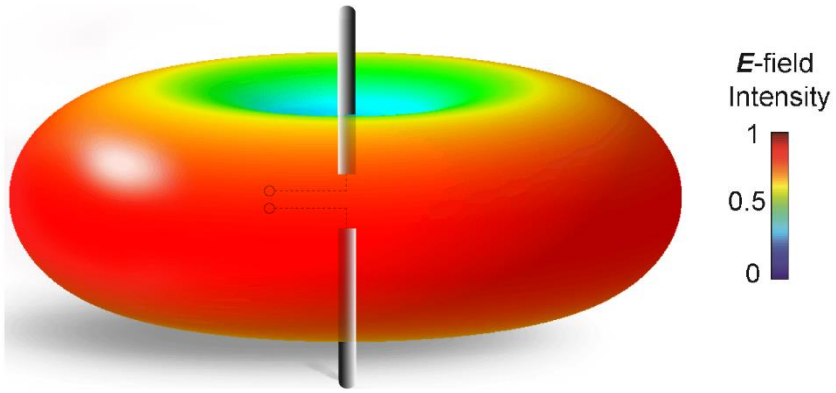

Figure 8. Toroidal radiation diagram of a dipole antenna.
Specifically, the normalized E-field distribution is depicted.

Radiation efficiency

This dimensionless quantity, represented by the Greek letter η, is defined as "the ratio of the total power radiated by an antenna to the net power accepted by the antenna from the connected transmitter". Mathematically:

$$P_{\mathrm{RAD}} = \eta P_{\mathrm{IN}}, \tag{2.3}$$

where P_{RAD} is the total power radiated by the antenna and P_{IN} the accepted power.

Impedance mismatch factor

This quantity, which we term τ, is defined as "the ratio of the power accepted by an antenna to the power incident at the antenna's terminals from the transmitter." That is, the backscattering loss is reduced by maximizing this factor, in which case we obtain an optimum *impedance matching*. High figures of τ guarantee that the antennas are conveniently matched to the surrounding medium to which the electromagnetic fields are radiated. Outstandingly, in the case of silicon-based on-chip antennas this is true for a wide working bandwidth as demonstrated in Chapter 3, PAPER A.

Total radiation efficiency

The total radiation efficiency, η_{TOT}, is defined as "the radiation efficiency of an antenna reduced by its impedance mismatch factor", which can be expressed as:

$$\eta_{TOT} = \tau\eta \tag{2.4}$$

With this definition, radiation efficiency takes into account any power loss mechanism related to the antenna, including the effects of backscattering [71].

Gain

Gain is one of the most important parameters in the design of antennas. The absolute gain of an antenna in a specific direction is defined as "the ratio of the radiation intensity in a given direction to the radiation intensity that would be produced if the power accepted by the antenna were radiated isotropically". The radiation intensity $K(\theta, \varphi)$ corresponds to the "power radiated from an antenna per unit solid angle in a given direction". Therefore, the gain in an arbitrary direction (θ, φ) is expressed as follows:

$$G(\theta,\varphi) = 4\pi \frac{K(\theta,\varphi)}{P_{\mathrm{IN}}} = \eta D(\theta,\varphi) \tag{2.5}$$

Gain is usually taken in the direction of the maximum radiation. This parameter is a measure that takes into account both the efficiency of the antenna and its directional radiation capabilities. Depending on the application, we must carefully choose a specific type of antenna with an appropriate gain. On the one hand, an antenna with a high gain figure can be useful in order to radiate most of the power in a given spatial direction, for instance, in a straight direct data communications link. On the other hand, this kind of highly-directive antenna would not be adequate if signals must be radiated on a wide area to supply several receivers or when implementing interference-based applications as the aforementioned beam shaping applications, which would require low-directive antennas.

Total gain

Also known as *realized gain*, this parameter is defined as "the gain of an antenna reduced by its impedance mismatch factor". Hence:

$$G_{\mathrm{TOT}}(\theta,\varphi) = \tau G(\theta,\varphi) = \eta_{\mathrm{TOT}} D(\theta,\varphi) \tag{2.6}$$

Bandwidth

It is defined as "the range of frequencies within which the performance of the antenna conforms to a specified standard with respect to some characteristic." This characteristic usually refers to gain or directivity. For example, one can define the antenna bandwidth at -3 dB as the spectral region within which the antenna gain does not fall below half of its maximum value.

Friis transmission equation

The Friis transmission equation is a widely used formula employed in wireless communications that allows us to calculate the fraction of the power supplied to an emitting antenna that can be extracted from a receiving antenna separated from the former by a distance d (with $d >> \lambda$), λ being the working wavelength of the system. The equation reads as follows:

$$P_{\mathrm{RX}} = P_{\mathrm{TX}} G_{\mathrm{TX}} G_{\mathrm{RX}} \left(\frac{\lambda}{4\pi d} \right)^2 \tag{2.7}$$

G_{TX} and G_{RX} being the total gain of the transmitting and receiving antennas, P_{RX} the received power and P_{TX} the power supplied to the emitting antenna. Thanks to this formula, we can easily determine the power efficiency of a given communication link just by knowing the gain of the involved antennas, the working wavelength, and the link distance.

2.2 Open-end waveguides enabling on-chip optical antennas

Following classical antenna theory, the silicon on-chip antennas that enable all the applications experimentally achieved in this thesis, were engineered using elemental silicon waveguides as a basis and analyzed as aperture antennas according to the field equivalence or Huygens' principle. This principle states that the radiated fields outside a closed surface *S* surrounding all electromagnetic sources can be obtained from the knowledge of the field tangential components on that surface [71]. In particular, the fields outside this surface are the same as the ones produced by the following electric and magnetic current densities

$$\mathbf{J} = \mathbf{n} \times \mathbf{H} \tag{2.8}$$

$$\mathbf{M} = -\mathbf{n} \times \mathbf{E} \tag{2.9}$$

Where **E** and **H** are the electric and magnetic fields over the surface *S* with normal **n**, see Figure 9. The radiated far fields can then be obtained from the following radiation vectors

$$\mathbf{N} = \int_S \mathbf{J} e^{i\mathbf{kr}} d\mathbf{s} \tag{2.10}$$

$$\mathbf{L} = \int_S \mathbf{M} e^{i\mathbf{kr}} d\mathbf{s} \tag{2.11}$$

We are mainly interested in the far-field radiated power, which is proportional to the radiation intensity $K(\theta,\varphi)$, which can be calculated from the radiation vectors as [71]:

$$K = \frac{\eta_B}{4\pi\lambda^2}\left(\left|\mathbf{N}_\theta + \left(\mathbf{L}_\varphi/\eta_B\right)\right|^2 + \left|\mathbf{N}_\varphi - \left(\mathbf{L}_\theta/\eta_B\right)\right|^2\right), \tag{2.12}$$

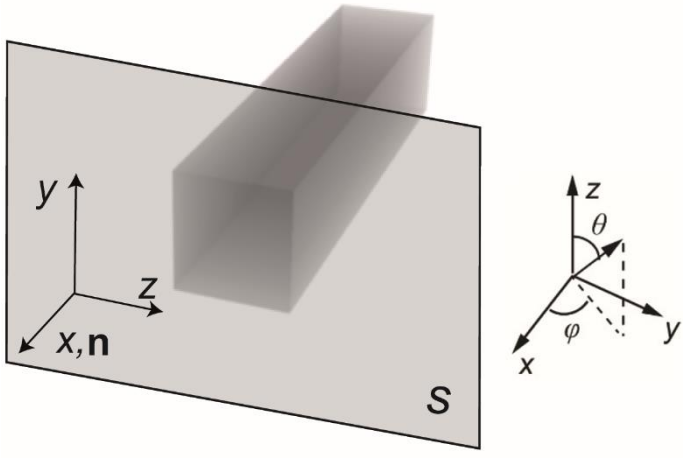

Figure 9. Example of Huygens surface *S* used in the calculation of the directivity of an elemental square waveguide. The effective currents associated with the fields radiated by the waveguide lie on *S*. In the chosen coordinate system, the normal vector **n** points in the *x*-direction.

from which the radiation pattern and directivity $D(\theta,\varphi)$ associated with **J** and **M** can be readily obtained (η_B is the background medium impedance) just by substituting (2.12) in (2.1).

Case of Study: Radiofrequency horn antenna

This technique is usually employed to calculate the radiation pattern of microwave aperture antennas (usually apertures in hollow metallic waveguides), since the main contribution to the fields over the surface that encloses the aperture and metallic waveguide comes from the fields on the aperture. Following these principles, we implemented an algorithm based on these previous formulas to calculate the final directivity of open-end apertures. To test the validity of this routine we applied it to different typical antennas and compared the result with their well-known directivity values. As an example, we include here the analysis of a radiofrequency pyramidal horn antenna operating at f = 10 GHz and fed by a hollow metallic waveguide with dimensions a = 2 cm and b = 1 cm, see Figure 10. From antenna theory, the directivity of a pyramidal horn antenna can be approximately retrieved from the next equation [90],

$$D(\theta,\varphi) = 6.4\frac{a_1 b_1}{\lambda^2}, \tag{2.13}$$

which provides a directivity $D(\theta,\varphi) \approx 17.25$ (linear units) for the considered values. Since this figure is just a coarse approximation given by the geometry of the horn, we additionally carried out a numerical calculation of the aforementioned directivity via the use of the commercial software CST Microwave Studio, yielding a value of $D(\theta,\varphi) = 21.9$. Finally, we applied our Huygens-based algorithm, calculating the final directivity from the **E** and **H** fields on the horn aperture, which were numerically calculated and introduced as matrices in the routine, giving a directivity $D(\theta,\varphi) = 20.8$, in very good consonance with the previous results, see Figure 10.

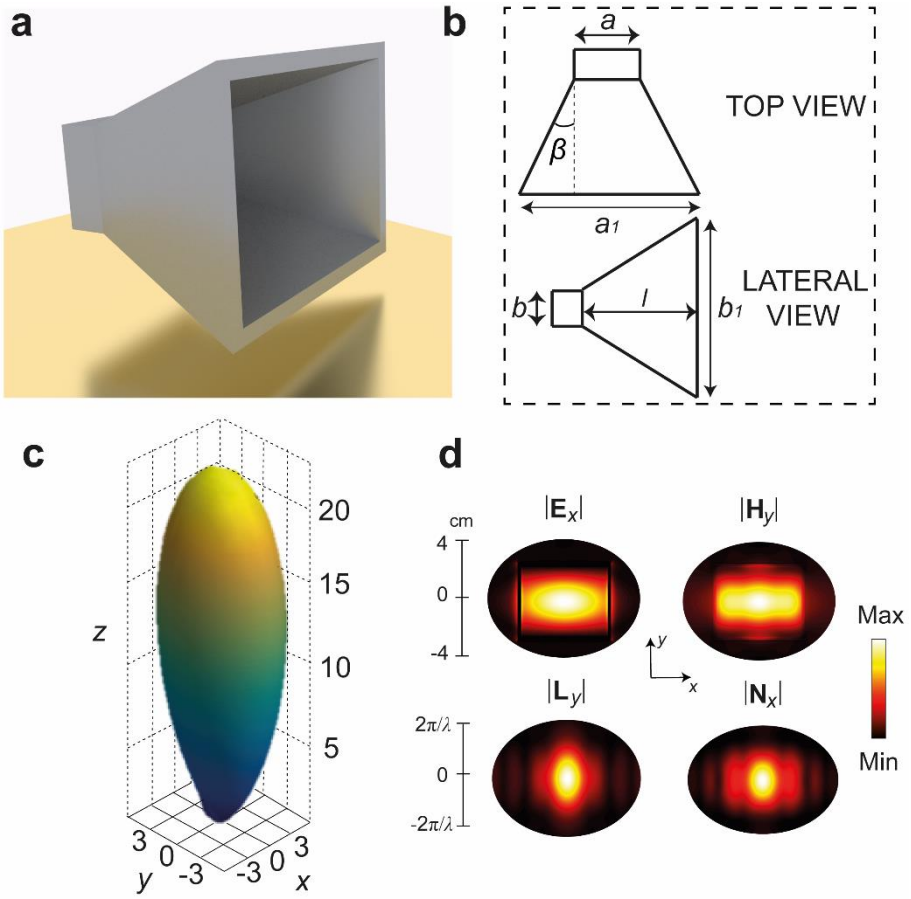

Figure 10. Pyramidal horn antenna directivity. (a) Artwork of the proposed antenna. (b) Schematic top and lateral view of the horn antenna with a_1=5.45 cm, b_1=4.45 cm, l = 3 cm and β = 30º. (c) Final directivity diagram (linear units) attained with the algorithm. (d) First row: Relevant components of the electric and magnetic fields of the fundamental mode supported by this antenna (outside this region, the fields are negligible). Second row: Corresponding radiation vectors of the horn antenna.

By using this method, we only need to calculate the two-dimensional mode profile on the considered waveguide to obtain the aperture directivity (as long as the aperture impedance is well matched to the surrounding medium, a condition that applies in this case as well as in the case of the designed on-chip silicon nanoantennas of this dissertation, see Chapter 3), avoiding computationally-intensive three-dimensional numerical calculations. Using the previous equations, we can calculate the radiation vectors associated with the fields at the waveguide output plane and hence the corresponding radiation pattern. In the optical regime, we will consider open-end dielectric waveguides as aperture antennas, so attaining the directivity of these structures will be straightforward by the using this technique. As mentioned above, these waveguides (mainly strip and slot designs) will be the basis from which engineering the directivity of the on-chip silicon antennas employed at every experimental application developed during this work.

2.3 Reconfigurability and beam-shaping capacities

As outlined at the beginning of the introductory chapter, developing silicon-based on-chip wireless reconfigurable networks is one of the novel applications experimentally demonstrated in this thesis. Specifically, we implemented a dynamically tunable antenna beam-steering system, which constituted a 1×3 switch, see Chapter 3. To this end, we took advantage of the fact that the refractive index *n* of the feeding waveguide of each of the antennas in an emitting array can be dynamically modified via different effects (*e.g.*, thermo-optic, electro-optic). Thanks to this, we can perform an independent tuning of the phase (and a potential amplitude control via interferometry) of each antenna. By combining the use of antenna arrays [71] with any of these effects, we can generate different radiation diagrams in almost any desired way. As an example, in Chapter 3, PAPER A, we employed silicon's thermo-optic effect [91−93] to achieve an active control of a four-element array.

Furthermore, thanks to use of antenna-based schemes we can engineer reconfigurable spots on a two-dimensional arrangement, see Figure 5, allowing the development of beam shaping devices. To this end, we take again advantage of the phase control that can be implemented in an antenna array. In particular, we can make the fields interfere constructively at a certain focal point (x_0, y_0) on a 2D plane by setting a hyperbolic phase profile given by the formula

$$\varphi_i = \frac{2\pi}{\lambda}\left(\sqrt{\left(x_i - x_0\right)^2 + \left(y_i - y_0\right)^2} - C\right) \tag{2.14}$$

where φ_i is the phase of the *i*-th antenna [located at (x_i, y_i)] and *C* is a constant that does not alter the focusing effect and that is usually taken to be $C = d_0 = (x_0 + y_0)^{1/2}$. As it will be demonstrated in Chapter 3, we employed standard strip waveguides (450-nm width, 220-nm height and directivity of 5.9) as the basic array antennas for this application, since low-directivity elements provide better results in this case. An example with and antenna separation $d \simeq 1$ μm in the *x*-axis between adjoining elements is shown in Figure 11. There, the ability to control the 2D focal position just by varying the array phase is demonstrated.

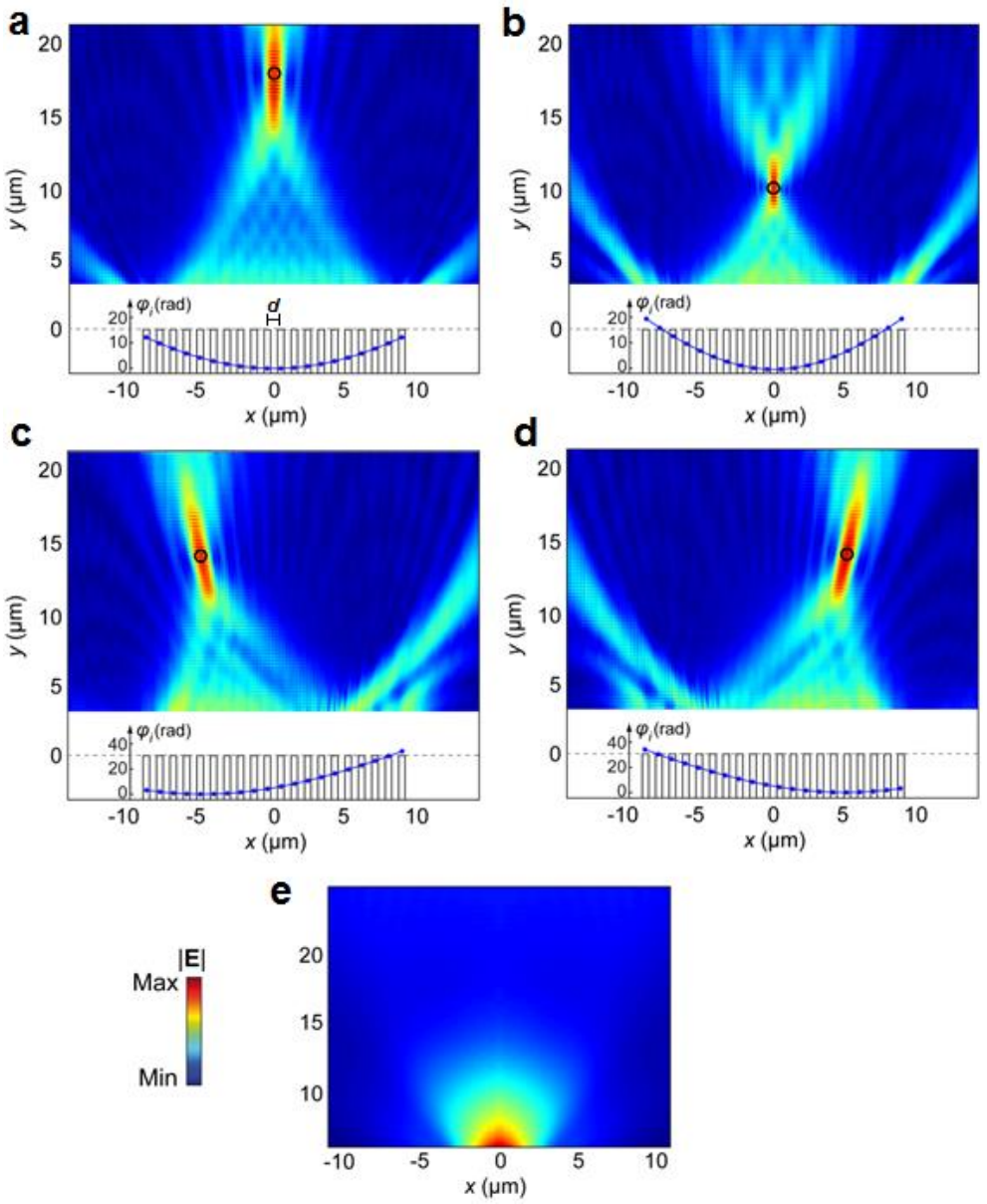

Figure 11. 2D focusing based on a phase-tunable strip antenna array. (a) (x_0, y_0) = (0, 18) μm. (b) (x_0, y_0) = (0, 10) μm. (c) (x_0, y_0) = (-5, 14) μm. (d) (x_0, y_0) = (5, 14) μm. The antenna array and the phase profile required for each focal position are also depicted. For simplicity, we simulated the field radiated by a single antenna in CST Microwave Studio and calculated the total field radiated by the array in MATLAB software. Although this method does not take into account the possible interaction between neighboring antennas, *d* is sufficiently large to neglect this effect. For instance, the excellent results on 2D beam focusing presented in Figure 7, Paper A, Chapter 3 (corresponding to the configurations in a and b) were obtained through full-wave simulations taking into account all possible interactions. (e) Field radiated by a single strip antenna (width of 450 nm, height of 220 nm).

2.4 Fabrication overview

In this section, we briefly review the main fabrication steps to develop not only the on-chip silicon antennas, but also the additional structures such as grating couplers, feeding waveguides, metallic heaters or plasmonic wires that were necessary to characterize the samples of the different applications implemented throughout this thesis, full details in Chapter 3.

Fabrication overview: Mask generation

Before carrying out the fabrication itself, we must generate a mask containing every structure needed to characterize the different parameters and the performance of the different applications. During the mask layout generation, we must consider the specific lithographic process limitations, which in our case, were essentially given by the aperture size (which limits the minimum size of the fabricated devices) of the electron-beam Raith150 tool employed at every design. Using the software provided together with the above-mentioned tool, we can generate graphic database system (GDS) files; see Figure 12 as example of this kind of layout, which is finally sent to the fabrication line.

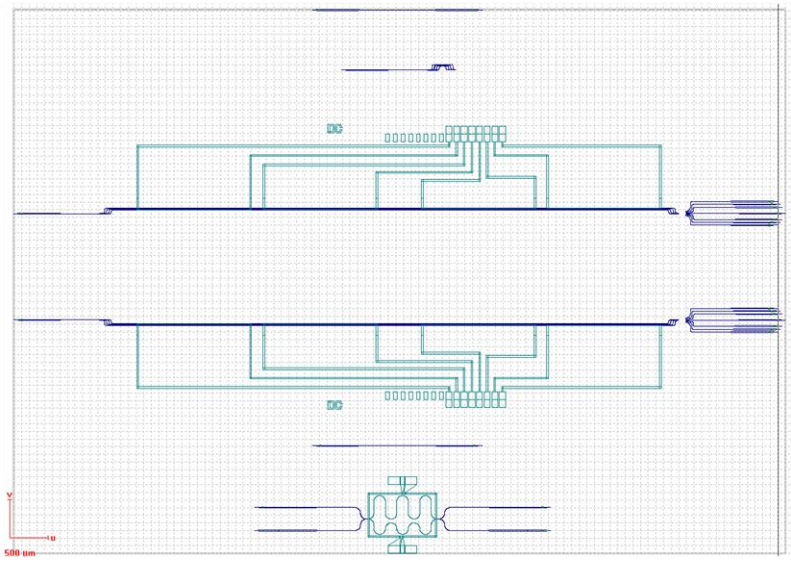

Figure 12. GDS including the different layers of several structures designed in order to experimentally characterize the proposed beam steering device, see Chapter 3, PAPER A.

Fabrication overview: Electron beam lithography

Electron beam lithography (EBL) is a technique that allows the nanofabrication of structures that would result challenging with conventional photolithographic processes. The current resolution of state-of-the-art EBL systems is in the boundary of 10 nanometers. This technique is based on the use of a highly focused electron beam that bombs the surface of a sample in order to write a previously designed pattern with different kinds of CAD software. The pattern is then carved out in an electron sensitive film (or resist) deposited onto the sample before exposure by spin coating, see Figure 13. Basically, the electron beam induces a change in the molecular structure and solubility of the resist film, which is developed in a suitable solvent to selectively dissolve either the exposed or unexposed areas of the resist.

After this step, the resulting structured resist layer placed atop the sample can be used as a mask or template for transferring the pattern into a specific structure. Two main pattern transfer techniques can be applied, see Figure 13. The first one involves etching away the material underneath the gaps in the resist layer, while the second one involves the deposition of a material (usually metal) spread onto the sample and dissolving away the remaining resist to 'lift-off' the deposited material on top. Thus, we only have the deposited material in the areas where the resist was not present.

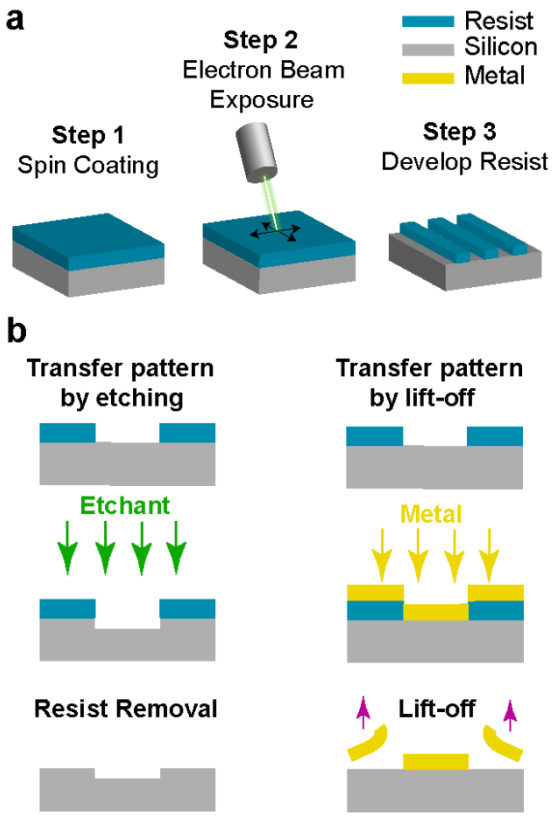

Figure 13. (a) Resist pattern schematic. (b) Schematic depicting the two main approaches to pattern transfer.

Facilities

The clear experimental vocation of this thesis would not have been satisfied without the outstanding facilities of the Valencia Nanophotonics Technology Center (NTC) and its 500 m^2 clean room class 10-100-10000, see Figure 14. This research center in Spain is recognized as a *Singular Scientific and Technical Infrastructures (ICTS)*. This kind of technological environments include large facilities, resources, equipment and services, unique in their kind, which are dedicated to cutting-edge technological research and development of the highest quality, as well as to encourage the transmission, exchange and preservation of knowledge, technology transfer and innovation. The NTC relies on a complete production line for the micro/nano fabrication on silicon with 6" CMOS compatible technology that allows the processing of photonic, electronic and electro-optic devices. Thanks to this, we were able to participle in not only the fabrication decision-making but also in the manufacturing process itself, working side by side with the clean room technicians.

The nanofabrication capacities at the NTC can be summarized as follows:

• 2 PECVD Applied Materials cluster tools (a-Si:H, Si3N4, TEOS-based B&P doped glasses)
• 3 PVD systems
• 4 tube Furnance
• Wet benches and Dry Rinse Spinner
• Dry Etching systems (RIE, ICP)
• Conventional & Rapid thermal annealing
• Lithography (e-beam & DUV "stepper")
• Resist and developer processing systems
• Ion implanter
• Coupling & Packaging full line
• Graphene Deposition (Aixtron Black Magic PRO 6 inches).

Additionally, the NTC also counts on several laboratories for photovoltaics, optical networks, systems analysis, biophotonics and a complete packaging area. Finally, diverse kinds of characterizations can be carried out, namely, physical characterization via scanning near-field optical microscopy (SNOM), scanning electron microscope (SEM) or atomic force microscopy (AFM) perfilometry, optical characterization (Fourier transform infrared (FTIR) and Raman spectroscopy) and electrical characterization (IV, EQE/IQE, Lifetime, Contact and Sheet resistance).

Figure 14. Clean room facilities at the Nanophotonics Technology Center in Valencia

Chapter 3

Our original contributions

As outlined in the first section, this thesis has been organized as a collection of papers. While Chapters 1 and 2 provide a brief but necessary background in order to better understand the work here shown, Chapter 3 directly includes the three main manuscripts that shape this dissertation as they were originally published, although using an unified format.

PAPER A (‘*On-chip wireless silicon photonics: from reconfigurable interconnects to lab-on-chip devices’*. ***Nature’s Light: Science & Applications*** 6, e17053 (2017)) represents the first and most relevant work of this thesis. Its importance is summarized as follows. Bringing the potential of classical radio communications to photonic chips, in this paper, we present the concept of *on-chip wireless silicon photonics* driven by a new concept of dielectric optical antennas as main building blocks from which experimentally realizing novel on-chip reconfigurable wireless optical systems. In this manuscript, we illustrate the potential of this new paradigm through several demonstrations. In the scope of communications, we highlight the first demonstration of an on-chip wireless optical data transmission link. Additionally, we carried out the first electrically-tunable on-chip beam steering demonstration, which can be regarded as a 1-to-3-port switch. Finally, within the biosensing area, a fully-integrated lab-on-a-chip version of a flow cytometer with micrometric planar optics was implemented, a device able to count and classify several kinds of microparticles.

PAPER B (‘*High signal-to-noise ratio ultra-compact lab-on-a-chip microflow cytometer enabled by silicon optical antennas’*. ***Optics Express*** 26, 25645–25656 (2018)) notably expands the work developed in PAPER A in the scope of optical integrated lab-on-a-chip biodevices.

Building upon the novel concept of integrated all-silicon nanoantenna shown in PAPER A, we design and experimentally demonstrate a label-free micro-optofluidic on-chip cytometer that exhibits an unprecedented combination of high signal-to-noise-ratio (SNR) —feature which enhances the reliability of on-chip detection— and ultra-compact footprint. Thanks to the reduced size of the employed silicon-based antennas and the needle-like beams radiated by them, we were able to realize the most compact optical subsystem in this kind of lab-on-a-chip biodevice with a performance comparable to the best state-of-the-art previous works.

Finally, PAPER C ('*All-Silicon on-chip optical nanoantennas as efficient interfaces for plasmonic devices*'. ***ACS Photonics*** 6, 1094–1099 (2019)), paves the way towards the combination of wireless silicon photonics together with plasmonic devices in order to provide new applications at the nanoscale. Trying to overcome the shortages in the crucial conveyance of light to/from these devices when using nanowires or plasmonic nanoantennas, we present an alternative solution supported by the principles of on-chip wireless silicon photonics. In particular, we introduce a new low-loss highly-directive silicon slot-waveguide-based nanoantenna able to be directly and efficiently coupled to plasmonic circuits. To test the performance of this scheme, we experimentally demonstrated the first on-chip plasmonic-dielectric interconnect over distances as high as 100 μm, clearly outperforming previous plasmonic approaches in terms of link efficiency and effective gain.

PAPER A. ON-CHIP WIRELESS SILICON PHOTONICS: FROM RECONFIGURABLE INTERCONNECTS TO LAB-ON-CHIP DEVICES

On-chip wireless silicon photonics: From Reconfigurable Interconnects to Lab-on-Chip Devices

Carlos García-Meca*, Sergio Lechago*, Antoine Brimont, Amadeu Griol, Sara Mas, Luis Sánchez, Laurent Bellieres, Nuria S. Losilla and Javier Martí

Nanophotonics Technology Center, Universitat Politècnica de València, 46022 Valencia, Spain.
* These authors contributed equally to this work.
Correspondence: J. Martí, Email: jmarti@ntc.upv.es

ABSTRACT

Photonic integrated circuits are developing as key enabling components for high-performance computing and advanced network-on-chip, as well as other emerging technologies such as lab-on-chip sensors, with relevant applications in areas from medicine and biotechnology to aerospace. These demanding applications will require novel features, such as dynamically reconfigurable light pathways, obtained by properly harnessing on-chip optical radiation. In this paper, we introduce a broadband, high-directivity (>150), low-loss, and reconfigurable silicon photonics nanoantenna that fully enables on-chip radiation control. We propose the use of these nanoantennas as versatile building blocks to develop wireless (unguided) silicon photonic devices, which considerably enhance the range of achievable integrated photonic functionalities. As examples of applications, we demonstrate 160 Gbit·s^{-1} data transmission over mm-scale wireless interconnects, a compact low-crosstalk 12-port crossing, and electrically reconfigurable pathways via optical beam steering. Moreover, the realization of a flow micro-cytometer for particle characterization demonstrates the smart system integration potential of our approach as lab-on-chip devices.

INTRODUCTION

The advent of photonic integrated circuits (PICs) promises to revolutionize high-performance computing (HPCs) and high-speed on-chip interconnects, because they are able to overcome the limits of conventional electronic technology in terms of speed, bandwidth, and energy consumption (1). In addition, as the possibilities offered by integrated photonics develop, a number of additional utilities, such as biosensing (2), optical beamforming (3), or metasurfaces for different applications (4), are emerging. However, current PIC devices typically rely on fixed layout guided interconnects that yield stringent design rules and limit network-on-chip reconfigurability, usually leading to complex topologies and large footprints (5, 6). Moreover, the strong confinement of the electromagnetic fields to the guiding structures prevents their

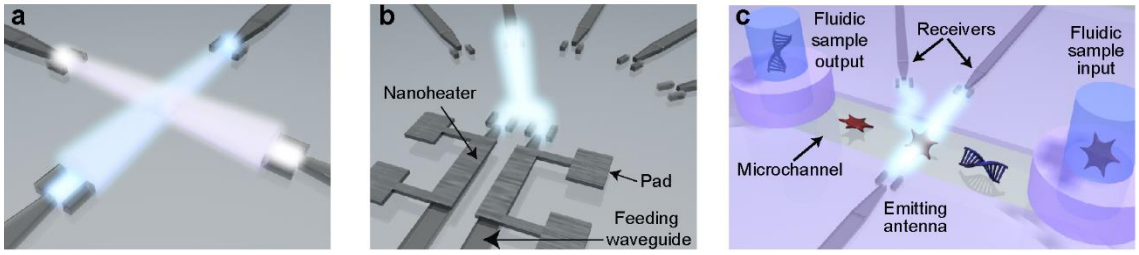

Figure 1. Envisioned scenarios for on-chip wireless optical systems. (**a**) Flexible networks: the use of highly directive antennas could allow for a variety of interferenceless wireless crossing configurations, favoring more flexible intra- and inter-core communications (11, 12). (**b**) Reconfigurable pathways and beam shaping: the radiation properties of antenna arrays (*e.g.*, radiation direction) depend on each antenna's phase, which can be electrically controlled by modifying the corresponding feeding waveguide temperature (benefiting from silicon's high thermo-optic effect) through the voltage applied over a nanoheater. This could be used for complex on-chip field pattern generation or traffic routing (6, 13). (**c**) Lab-on-a-chip: the proposed antennas can replace bulky light emitters and receptors, providing an ideal platform for the miniaturization and smart integration of sensors and voluminous lab equipment (7, 8). As an example, we show a fully integrated flow cytometer consisting of a microfluidic channel through which a sample containing several analytes of interest (platelets, DNA segments) can flow and be simultaneously illuminated by an antenna. The scattered light collected by other antennas provides information on each analyte.

interaction with the outer medium at far-field distances, a feature required in a variety of sensors and devices (7-9), as well as in applications related to microparticle control and acceleration (10), among others. Just as radio frequency and microwave antenna technologies have enabled countless unprecedented applications (cellular and satellite communications, radar, and biomedical imaging, among others), the ability to radiate electromagnetic fields within a chip in a controlled manner would allow us to overcome the aforementioned limitations and open doors to a wide range of new functionalities. As an illustration, envisioned scenarios where on-chip wireless systems could deliver great potential are sketched in Figure 1. Although a wide variety of optical antenna implementations can be found in the literature, they suffer from different shortages that hamper their use as building blocks for the anticipated model of a wireless optical system. Plasmonic nanoantennas, on the one hand, have emerged as a key component in many nanophotonic applications (14-19) due to their capacity to concentrate optical energy at very high frequencies (20) and to provide a more efficient alternative to plasmonic wires (21-23). Unfortunately, they exhibit poor directivity values and high absorption losses at optical frequencies. Additionally, the excitation of these nanoantennas usually requires complex feeding elements such as nanodipoles, off-plane laser sources, or quantum dots (14, 23, 24), which in practice represents an additional technological challenge. On the other hand, we can also find studies based on the use of dielectric antennas, employing either arrays of grating couplers (25-27) or scatterers (28). However, both configurations are only suitable for off-chip radiation. Furthermore, grating coupler arrays lead to large footprints, while scatterers show poor directivity values. In this article, we build on a new concept of silicon optical antennas compatible with complementary metal-oxide-semiconductor (CMOS) technology to show the feasibility of the

devised model of an on-chip wireless system. We provide proof of the power of our approach by experimentally demonstrating a diverse range of applications.

MATERIALS AND METHODS

Antenna theory and design

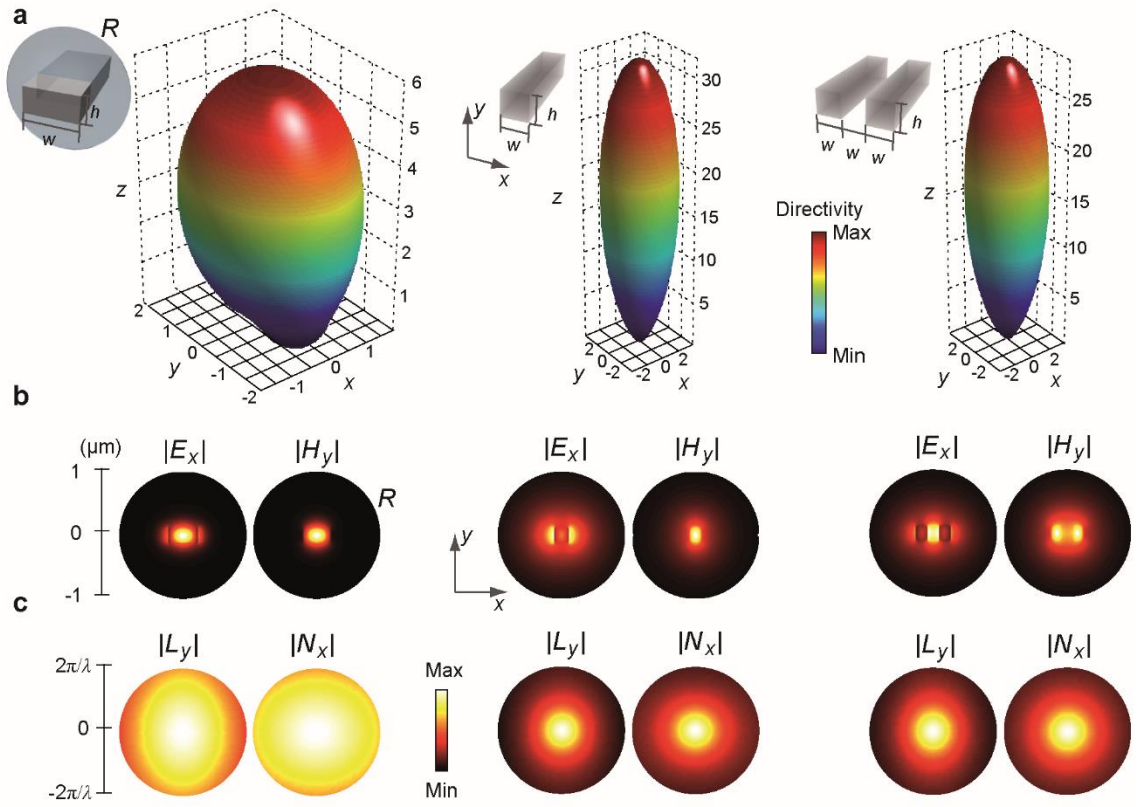

Figure 2. Properties of dielectric waveguides as radiating elements. (**a**) Directivity diagrams (linear units) of different waveguides with height *h* and width *w*. (**b**) Relevant components of the electric and magnetic fields of the modes supported by these waveguides in *R* (outside this region, the fields are negligible). (**c**) Corresponding radiation vectors (see Supplementary Information). 1st column: standard strip (*h* = 220 nm, *w* = 450 nm). 2nd column: square strip (*h* = 220 nm, *w* = 220 nm). 3rd column: designed slot (*h* = 220 nm, *w* = 180 nm).

The first step to achieve the desired architecture is to develop a type of antenna exhibiting low loss and low reflection, and whose directivity can be tuned to have a wide range of values able to accommodate different applications, while maintaining a reduced transverse size. In this work, we focus on applications such as mm-scale wireless optical links and on-chip contactless sensing, which require very high directivity values (>50) for good performance. Recent studies show that nanoantennas based on dielectric nanoparticles exhibit lower losses and higher directivity than metallic structures (29, 30), although the directivity is still too low for the above-mentioned applications. Moreover, these structures present important fabrication challenges. Here, we studied the possibilities of open-ended silicon-on-insulator (SOI) waveguides (31) as potential radiating elements that could solve these shortcomings. We modeled this type of structure using Huygens' principle (32), *i.e.*, the radiated fields outside a closed surface *S* surrounding all

electromagnetic sources can be obtained from the fields' tangential components on *S* (see Supplementary Information), a technique usually employed to calculate the radiation pattern of microwave metallic aperture antennas. Since the fields at the antenna output plane (normal to the propagation direction and containing the waveguide end) are concentrated in a small spatial region *R*, we can apply Huygens' principle by taking *S* to be this plane, knowing that only the region *R* will be relevant in the calculations (Figure 2a,b). Moreover, if reflections at the waveguide open end are negligible (which is the case in the studied structures), the fields on *S* are essentially equal to those of the infinite waveguide mode. Hence, this simple approach directly links the waveguide radiation pattern with its two-dimensional (2D) mode profile, which can be easily calculated using a 2D eigensolver. Specifically, the direction-dependent radiation intensity can be obtained straightforwardly from the so-called radiation vectors, which are the Fourier transform of the mode tangential electric and magnetic fields (see Supplementary Information). Therefore, less confined modes lead to higher directivities, since as the spatial extension of the mode increases, the angular extension of the radiation vectors decreases (a property of the Fourier transform); that is, energy is radiated in a smaller set of directions. Remarkably, the mode extension of the studied guiding structures can be readily controlled by varying their transverse dimensions, which gives us an intuitive and simple method for tailoring the antenna directivity. In addition, it can be shown that, from moderately high directivity values, these waveguide-based structures support weakly confined modes that favor impedance matching, resulting in very low reflections. Finally, the use of dielectric materials guarantees the desired low losses. Using these ideas, we designed several structures based on standard SOI photonic waveguides (31), namely, strip and slot configurations, ensuring a simple fabrication process and avoiding complex feeding structures. The directivity patterns, mode profiles, and radiation vectors of several of the studied configurations are depicted in Figure 2. It is clear that a strip waveguide with standard dimensions shows a strong confinement. Consequently, the radiation vector values within the circle of propagating wavenumbers are quite uniform, resulting in a low directivity. However, if the strip width is reduced, the mode profile spreads over a wider region, reducing the angular spectrum extension and enhancing the structure's directivity. For instance, a square strip shows a less confined mode with a directivity of approximately 30. Regarding the slot waveguide, we verified that wide-gap versions of this structure propagate less confined modes than standard strip/slot configurations. This analysis allowed us to design a slot waveguide displaying similar directivity values to that of the square strip (Figure 2a).

In practice, we can obtain a reflectionless transition from a standard 450-nm-wide strip waveguide to a custom-width radiating end (exhibiting directivities that can be higher than 100) through an inverted taper. Since the elements required for coupling light to the designed slot

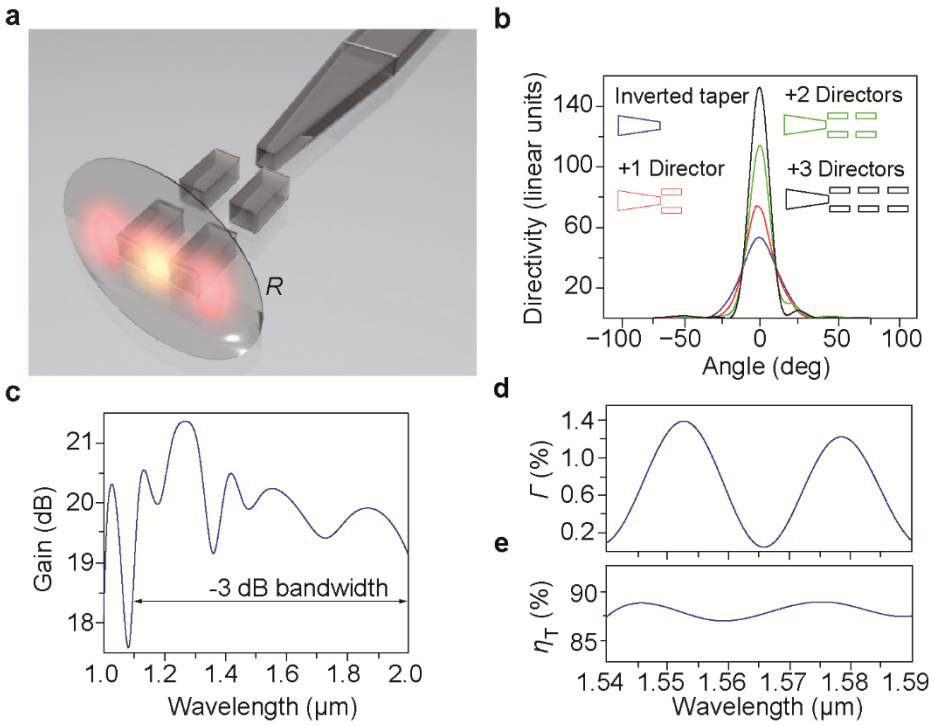

Figure 3. Designed antenna and main parameters. (**a**) Illustration of the inverted-taper antenna with two directors and the fields in the region *R* employed in Huygens' method. (**b**) Directivity of the designed antenna as a function of the number of directors. (**c**) Theoretical antenna gain and -3 dB bandwidth. (**d**) Simulated reflectance Γ within the window of the experimental measurements. (**e**) Total efficiency $\eta_T = \eta_R(1-|\Gamma|^2)$, where η_R is the antenna radiation efficiency. Calculations were performed with CST Microwave Studio.

waveguide usually add larger power penalties to the system, we focused on the strip configuration. For the sake of fabrication simplicity and to avoid long taper structures, we fixed a minimum taper tip width of 150 nm, which allowed us to attain directivities higher than 50. Moreover, inspired by Yagi-Uda antennas (16, 33), we studied the effect of using different planar structures as directors to further improve the directivity of the designed inverted taper antenna while maintaining a reduced size. Since the electromagnetic response of such structures cannot be addressed analytically, its dimensions were determined numerically. Nonetheless, Huygens' method still applies for directivity calculations, although 3D simulations are required to obtain the fields at *R*. Note that in our experiments, the fabricated antennas are covered with a SiO_2 layer to improve their performance. The finite size of the resulting SiO_2 embedding matrix was also considered in the directivity calculations (see Supplementary Information). After an optimization process (see Supplementary Information), we obtained a director configuration consisting of two symmetric silicon strips. In addition, we analyzed the effect of using several directors (up to three), whose separation was optimized as well (Figure 3b). The resulting antenna (inverted taper + directors, Figure 3a) can be engineered to display directivity values between 5 and 150, providing an extremely high design flexibility. The directivity improvement associated with the third director is moderate (~33%) compared to the improvement achieved by the second director

(~54%). For simplicity, we chose a two-director configuration (directivity of 114), which already satisfied the requirements for all the considered applications. Note that recent dielectric antennas reach directivity values up to 12 (29), while typical plasmonic nanoantennas exhibit lower values (21-23). The designed antennas have another important feature: a large bandwidth. Specifically, the calculated gain of the designed antenna exhibits a -3 dB bandwidth higher than 900 nm (Figure 3c). The reason is that these structures do not rely on resonant phenomena. In contrast, they display almost perfect impedance matching in a wide spectral region, thus yielding low reflections (Figure 3d) as well as a total efficiency close to 90% (Figure 3e). Therefore, unlike in typical plasmonic works, auxiliary resonant matching elements are not required, avoiding the bandwidth limitation they introduce. Let us now see how the proposed low-loss, broadband, and highly directive antenna configuration can provide efficient solutions in many different situations.

Fabrication of the optical devices

The antenna-based links were fabricated on standard SOI samples from SOITEC (Bernin, France) wafers with a top silicon layer thickness of 220 nm (resistivity ρ ~1-10 $\Omega \cdot cm^{-1}$, with a lightly p-type background doping of ~10^{15} cm^{-3}) and a buried oxide layer thickness of 2 μm. The fabrication is based on an electron-beam direct-writing process performed on a coated 100 nm hydrogen silsesquioxane (HSQ) resist film. The mentioned electron-beam exposure, performed with a Raith150 tool, was optimized to reach the required dimensions employing an acceleration voltage of 30 KeV and an aperture size of 30 μm. After developing the HSQ resist using tetramethylammonium hydroxide, the resist patterns were transferred onto the SOI samples employing an optimized inductively coupled plasma-reactive ion etching process with fluoride gases. Finally, a two-micron-thick silicon dioxide upper cladding was deposited on the SOI sample by using a plasma enhanced chemical vapor deposition system from Applied Materials (except in the beam steering experiment, in which a one-micron-thick layer was used to improve the efficiency of the nanoheaters).

Fabrication of the nanoheaters

The nanoheaters were fabricated using a direct writing electron beam process to transfer the patterns onto a 300-nm-thick Poly-methyl methacrylate resist layer. The thin titanium layer evaporation was performed prior to a lift-off process using N-Methyl-2-pyrrolidone. The high thermo-optic coefficient of silicon enables large refractive index (n) changes produced by local temperature (T) variations $\partial n / \partial T = 1.86 \cdot 10^{-4}$ K^{-1}. As an example, a temperature variation of only 10°C (readily available in our configuration) can lead to a local refractive index variation of $\Delta n = 1.86 \cdot 10^{-3}$, implying that a full π-phase shift can be achieved over a length of L_π = 417 μm, assuming a uniform distribution of the heat across the waveguide. In our configuration, we

employed 1.5-mm-long heaters to ensure full control over the phase. Interestingly, because the thermo-optic effect only affects the real part of the refractive index, current-dependent absorption mechanisms, which could affect the output intensity of each individual antenna (and hence create distortion of the overall radiation pattern), do not take place. This is in contrast to the widely used free-carrier plasma dispersion effect, where both the real and imaginary parts of the refractive are altered.

Fabrication of the microfluidic system

For the fabrication of the fluidic channel, a Cr layer of 35 nm was first deposited on the SOI sample by using electron beam metal evaporation. A direct writing electron beam exposure of the channel was then performed on a layer of 100 nm of PMMA 950K positive resist. After the resist development, Cr was removed from the channel area using a wet Cr etchant process based on CR-7 ($HClO_4 + C(NH_4)_2(NO_3)_6 + H_2O$). Afterwards, an ICP-RIE process was carried out to open the channel through the SiO_2. Finally, the sample was cleaned to remove the organic residues using a mixture of H_2SO_4 and H_2O_2 (3:1) for 20 minutes and then washed by deionized water (DIW). This cleaning procedure was also used to regenerate the device after sensing experiments. To prepare the employed PDMS thin substrates (Sylgard 184 Silicone Elastomer Down Corning), the PDMS mixture (10:1) was spin-coated on glass cover slides and cured at 60°C for 1 hour to obtain a thin (150 μm) PDMS layer on the glass slide. After the curing process, the PDMS was peeled off from the glass slide and washed in absolute ethanol to clean the surface. Finally, the PDMS substrate was positioned and aligned on top of the fluidic channel. The polystyrene microparticles used in the experiments were obtained from Sigma-Aldrich and have a size of 1 and 2-μm with a standard deviation less than 0.05 μm.

RESULTS AND DISCUSSION

As an initial demonstration, we experimentally achieved the first wireless transmission through on-chip links. Moreover, we demonstrated high-speed data transmission over mm-scale distances. For this purpose, several links consisting of two identical antennas (see Figure 4d for final antenna dimensions) with different gap distances d (0.1, 0.2, 0.4, and 0.8 mm) were fabricated on an SOI platform, see Figure 4e and (see Supplementary Information). We measured the link power efficiency $\eta_P = P_{RX}/P_{TX}$ (P_{RX} and P_{TX} are the received and transmitted power, respectively) as a function of d by injecting light into standard 450-nm-wide strip waveguides (connected to the antennas) using conventional grating couplers and tapers (Figure 4a). The experimental antenna gain was also determined and found to be in good agreement with our theoretical estimation (Figure 4b). Digital data transmission over the 0.4-mm link was

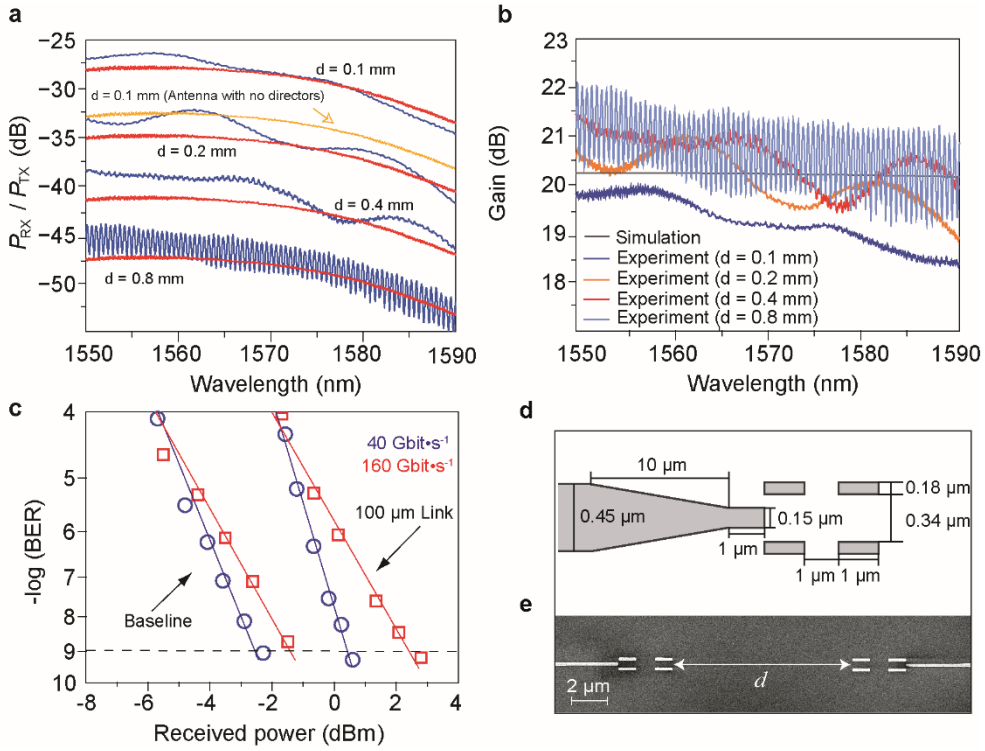

Figure 4. Experimental high-speed long-reach wireless data transmission. (**a**) Experimental (blue) and theoretical (red) power efficiency for different distances *d*. The theoretical efficiency is obtained as $\eta_P = (D\eta_T\eta_G)^2 C_R$, where D is the antenna, η_G accounts for the experimental grating coupler insertion losses, and C_R for the reflections at the top and bottom SiO_2 interfaces (see Supplementary Information). For comparison purposes, the simulated efficiency corresponding to a bare tapered antenna with no directors is also included for the 100-µm link. (**b**) Simulated and experimental (retrieved from the measurements with the previous formula) antenna gain, defined as $G = D\eta_T$. (**c**) BER measured with an error analyzer and evaluated as a function of the decreasing optical power received by the photodetector for a baseline configuration where the wireless link was replaced with a silicon straight waveguide (left) and for a 100-µm wireless link (right). The 160 Gbit·s^{-1} BER corresponds to the demodulation of channel 34 when transmitting channels 33 to 36. The crosstalk produced by surrounding channels (33, 35 and 36) introduces low penalties. (**d**) Schematic top view of the antenna and directors. (**e**) SEM image of a point-to-point link with d = 10 µm.

demonstrated by sending 40 Gbit·s^{-1} pseudo-random bit sequences at 38 different ITU channels evenly spaced by 0.8 nm, ranging from 1534.25 to 1563.86 nm (a complete description of the employed setup can be found in Supplementary Information). Clean eye diagrams (see Supplementary Information) and bit error rates (BER, number of detected bit errors over the total number of transmitted bits) below 10^{-9}, *i.e.*, sufficiently low to rule out forward-error correction schemes often related to an increase in chip complexity, were measured in all cases, verifying the abovementioned broadband features. This performance shows the feasibility of attaining terabit-per-second data streaming over mm-scale distances by using wavelength multiplexing. To illustrate this possibility, we transmitted 160 Gbit·s^{-1} data streams consisting of four de-correlated 40-Gbit·s^{-1} sequences at wavelengths ranging from 1548.52 nm to 1550.92 nm (0.8 nm evenly distributed), obtaining the same performance in terms of BER (Figure 4c). Remarkably, the

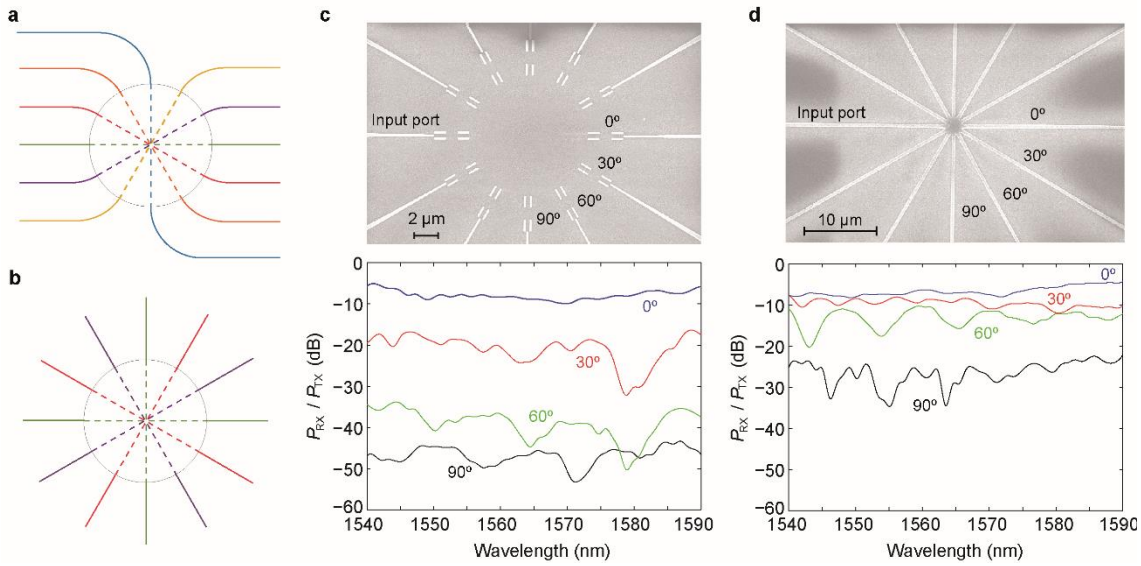

Figure 5. Comparison of wireless and guided 12-port crossings. (**a-b**) Two different utilities of the device. (**c-d**) SEM images and measured transmission efficiency for the receiving ports at 0°, 30°, 60° and 90° associated with the fabricated (**c**) wireless and (**d**) guided implementations of the device (*i.e.*, dashed connections inside the gray circles).

demonstrated directive behavior could permit the implementation of unguided crossings in many different configurations (as in Figure 1) without perturbing the beam propagation or adding any undesired crosstalk (and even leads us to envisage the possibility of achieving efficient inter-core on-chip wireless interconnects), thus providing a much more flexible optical interconnect architecture.

Along this line, so far, research efforts have focused on optimizing single (two-waveguide) crossings, achieving an excellent performance both in terms of crosstalk and insertion loss (34). While an equivalent wireless crossing could show a negligible crosstalk (due to the high directivity of the proposed antennas), it would be extremely difficult to surpass the insertion loss performance obtained with state-of-the-art guided approaches. The potential of the wireless approach, however, becomes apparent in more complex configurations involving a high number of ports. In this case, the solution adopted in guided technology consists of a combination of many single crossings (5, 34). Unless using rectangular grids (crossing of two arrays of parallel waveguides), this results in complex topologies with different drawbacks. Consider, for instance, the configuration in Figure 5a. It consists of six input waveguides whose outputs are vertically flipped. This configuration can also be understood as three single crossings (red, green, and blue) that at the same time, cross each other, see Figure 5b. Even with a crossing-aware routing algorithm, a guided implementation of this device would require a large number of crossings and bends (5), yielding either a large footprint or high values of crosstalk and insertion loss. To reduce the footprint, the best option is to use a direct star crossing, whether wireless as in Figure 5c or guided as in Figure 5d. To analyze these alternatives, we fabricated and optically characterized both (same antenna configuration as in the data transmission example). It is worth mentioning

that we have not found any previous work on multiple simultaneous crossings with more than four ports. Hence, we have used a direct crossing for the guided device. In any case, due to the small (and fixed, if a symmetric behavior is desired) angle between adjacent waveguides, it would be challenging to optimize this crossing using tapered waveguides as in the single crossing case. The measured device transmission efficiency between the input port and the output ports located at 0° (direct interconnect), 30°, 60° and 90° is shown in Figs. 5c-5d. Note that the wireless signal transmitted to the output ports at 120° and 150° was so low that it was outside the detector range. Regarding the crosstalk, it is evident that the antenna-based configuration outperforms its guided counterpart. Specifically, looking at the most critical output ports (those at ±30°), a crosstalk figure between -10 dB and -24 dB (mean value of -13 dB) is obtained within the experimental window for the wireless crossing, while unacceptable crosstalk values between 0 and -6 dB (mean value of -2.9 dB) are obtained for the guided case. Moreover, the direct interconnect transmission efficiency (or, equivalently, the insertion loss) is similar in both cases, which is explained by the much higher crosstalk and scattering of the guided device. Therefore, the better performance and compact feature (facing antennas separated by 10 μm) of the wireless solution provides a superior solution for footprint-constrained applications.

The increasingly indispensable requirement for reconfigurable on-chip networks motivated a second application: a dynamically tunable antenna beam-steering system. To this end, we benefited from a distinctive feature of the proposed architecture, *i.e.*, the excitation scheme based on silicon waveguides. The fact that the refractive index *n* of these structures can be modified dynamically with different effects (*e.g.*, thermo-optic, electro-optic) permits the independent tuning of the phase (and ultimately the amplitude via interferometry) of each waveguide's output signal and, therefore, the phase of the antenna it feeds. Consequently, the use of antenna arrays (32) in combination with any of these effects makes it possible to mold the in-plane radiation diagrams in almost any desired way. In particular, an array in which all elements are fed with the same amplitude and an α progressive phase delay shows a maximum in the direction θ_{max}, with $\alpha = -kd_A \cos\theta_{max}$ (d_A representing the separation between neighboring antennas). Thus, we can steer the radiated beam at any direction through a proper choice of α. As an example, we exploited silicon's thermo-optic effect (35) to achieve an active control of a four-element array (separation between emitting antennas d_A = 1.65 μm). Note that as the single-antenna directivity increases, the maximum directivity of the full array decreases more quickly with $|\theta_{max}|$, limiting the device angular range. However, low-directivity antennas result in low full-array directivities even for small values of θ_{max}, increasing the crosstalk between adjacent receiving antennas. Finally, we used bare inverted taper antennas, as this configuration yields very high directivities (see Supplementary Information) and enables us to steer the beam by ±15º

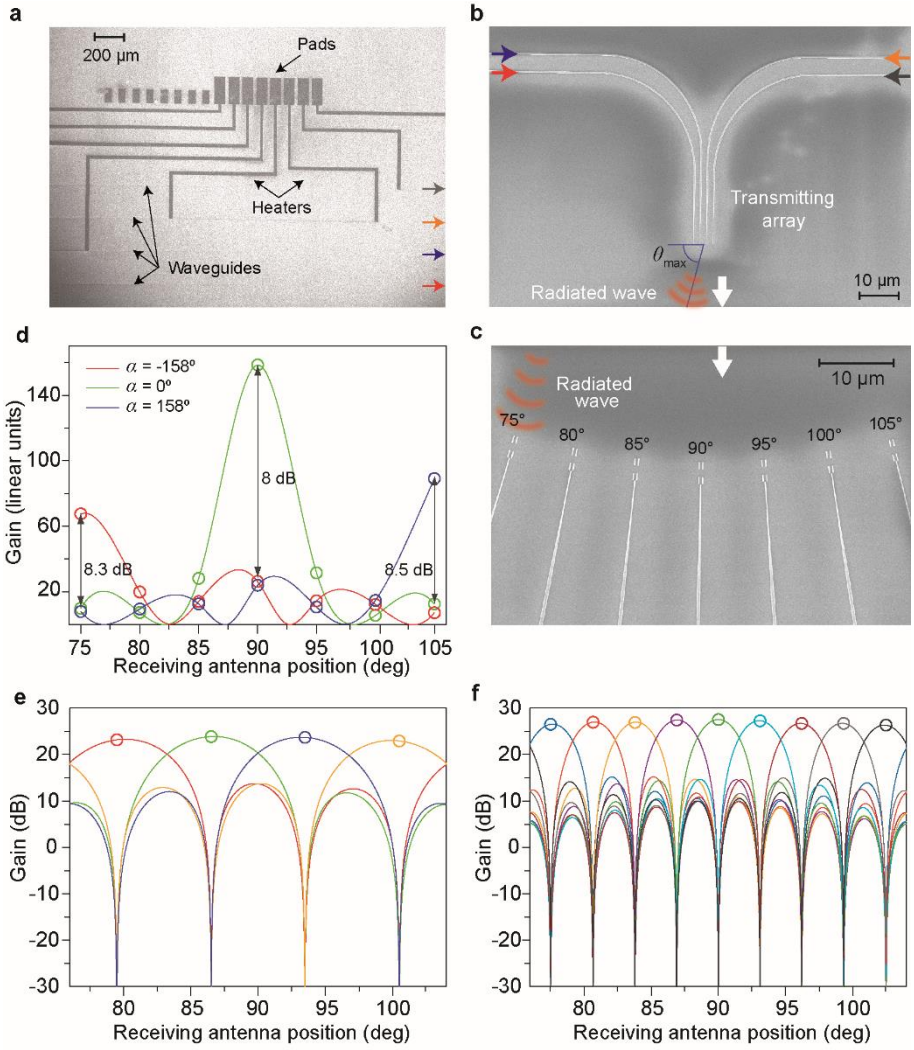

Figure 6. Experimental electrically reconfigurable beam steering. (**a**) SEM image of the nanoheaters with their corresponding pads and the underlying feeding waveguides. (**b**) SEM image of the waveguides used to feed the 4-antenna emitting array (colored arrows indicate the waveguides paths in A and B). (**c**) SEM image of the receiving subsystem consisting of 7 antennas placed at different angles. The antennas at 75°, 90° and 105° are taken as the device output ports. The values of α that allow us to steer the beam to each of these ports were estimated to be -158°, 0° and 158°, respectively (see Supplementary Information). (**d**) Total array gain associated with each receiving antenna (d = 100 μm, λ = 1550 nm) for the three values of α. Circles indicate measured values at each antenna position. The crosstalk at the output ports is highlighted, with values always higher than 8 dB. (**e-f**) Simulated total array gain associated with two different wireless 1×N switches for each of the N optimized values of α (each with a different color). The zeros of the corresponding radiation diagrams determine the N angles at which the receiving antennas are located. At each of these positions, the radiated power is zero for all values of α except one, for which the radiated power is almost maximum (marked with a circle). (**e**) N = 4. (**f**) N = 9.

with a maximum intensity radiation drop of ~3 dB. This 30° range, together with the high link distances enabled by such high directivities allows us to place a considerable number of receiving antennas at different angles. Since reception always occurs at normal incidence, we employed an *inverted taper + 2 director* configuration for the receiving antennas (Figure 6b,c). After covering the fabricated antennas and waveguides with a 1-μm-thick SiO_2 layer, we deposited a 100-nm-

thick titanium nanowire or nanoheater (terminated by two pads) on top of each feeding waveguide (Figure 6a). The electrical current flowing through each nanoheater is converted to heat via the Joule effect, which propagates through the SiO_2 layer down to the corresponding silicon waveguide, modifying its local temperature (T), and inducing a refractive index change given by $\partial n / \partial T = 1.86 \cdot 10^{-4} \mathrm{K}^{-1}$. The temperature variation is determined by the intensity of the electrical current, which is controlled by the voltage applied across the corresponding pads. With this technique, we experimentally demonstrated a reconfigurable 30-degree beam-steering system over 100-μm links (λ = 1550 nm). This steering device can be regarded as a 1-to-3-port switch. Along this line, we estimated its switching time: 5.2 μs, and its switching power: 8.3 mW per nanoheater (three simultaneous active heaters are required to aim the beam at any of the side antennas). This results in a figure of merit (switching power times the switching time) of 43.16 mW·μs, which is in agreement with current state of the art (see Supplementary Information). The aim of this demonstration is to illustrate the capabilities of the proposed reconfigurable wireless links in terms of reach and angular range and therefore the device was not optimized to work as a switch. In this sense, there are several aspects that can be easily improved by a proper choice of the system parameters. First, the 3-dB relative power loss between adjacent ports can be reduced by decreasing the steering angular range (*e.g.*, by increasing d_A). Second, although the sharp beams radiated by our highly directive antennas yield a crosstalk value below -8 dB (Figure 6d), which would be acceptable for some applications (*e.g.*, by using forward error correction schemes), it would not be for others. Here, we can achieve a dramatic improvement by exploiting an important feature of antenna arrays. In particular, the directivity of an array of N antennas is periodic as a function of $\psi = kd_A \cos\theta$ with N-1 equally spaced zeros per period. The phase delay α shifts the directivity diagram in ψ (32). Hence, there are N values of α associated with N different principal radiation directions, for each of which the radiated power is nearly maximum, while being zero for the remaining N-1 directions. Therefore, by using N-antenna arrays, we can theoretically obtain a 1×N switch with no crosstalk. Lastly, the link distance and the separation between receiving antennas can be considerably reduced to minimize the footprint and the radiation loss.

To illustrate these ideas, we designed and numerically simulated two different optimized switches. In both cases, we considered a value of d_A = 2.2 μm and a spacing of 3 μm between adjacent receiving antennas. As a first example, we demonstrate that the proposed 4-antenna array can be easily tuned to build a high-performance 1×4 switch by placing the receiving antennas at the angles shown in Figure 6e, which depicts the total array gain for each optimum switch state (value of α). As can be observed, a negligible crosstalk with less than 1 dB relative loss is obtained. It is clear that fabrication imperfections will result in a non-zero crosstalk. However, the good agreement between our theoretical calculations and the experimental results obtained for the fabricated switch confirms that our simulations constitute a good prediction of the device's

experimental performance. Hence, very low crosstalk is expected for this new design. The employed receiving antenna separation and angle span determine a link distance of d = 23 μm, yielding a wireless subsystem footprint (including the antennas) of approximately 48 × 14 μm^2. As a second example, we designed a 1×9 switch with similar features and a corresponding footprint of 80 × 30 μm^2 (d = 55 μm), see Figure 6f.

To calculate the overall footprint, the heated regions must also be taken into account. However, it should be noted that our work is focused on the photonic subsystem and we did not optimize the heating subsystem. Nonetheless, our device has no special heating requirements, and any state-of-the-art heater designed for a typical strip waveguide is also valid for our system. For instance, considering the heaters of Ref. 36, a rough estimation provides a total footprint of 45 × 113 μm^2 (this value is approximately three times lower than the most compact design we have found in the literature (36-38)) and 120 × 155 μm^2 for the 1×4 and 1×9 switches, respectively.

There are two additional potential advantages of our approach. First, our system only requires one stage regardless of the number of output ports. The guided approach is based on the use of cascaded 1×2 switches (36), for which crosstalk becomes preponderant and cumulative, swiftly degrading the system performance only after a few stages (39). Consequently, the wireless switch is more versatile and easily scalable. For example, to increase by one output, a 1×8 switch requires passing from 3 to 4 stages, while in the wireless case, only adding one antenna to the input and output arrays is required. Furthermore, unless the number of outputs is a power of 2, the signal will go through a different number of stages depending on the output port in a guided switch, which will give rise to an additional unbalance. Second, in the proposed approach, the heating and wireless subsystems are separated. This can simplify the packaging of the device in comparison to the guided solution, in which the heaters are distributed throughout the whole system.

It has been shown that the radiative crosstalk between neighboring elements may be important in guided devices due to structure imperfections (40, 41). Therefore, a discussion regarding the radiative crosstalk associated with wireless components naturally follows. There are two main factors suggesting that this parameter could be negligible in most situations. First, the devices outside a given antenna angular range are not particularly affected since the radiated power rapidly decreases away from the principal radiation direction (*e.g.*, the gain of a two-director antenna falls by almost 20 dB at ~20°). Second, for the devices within this range, it must be considered that the radiated power decreases as $1/d^2$. At d = 20 μm, the power efficiency at 0° for a single two-director antenna is below -20 dB. In our wireless devices, this is compensated by using a high-directivity receiving antenna (>20 dB). However, typical guided devices will exhibit a very low directivity and collect almost no radiated energy.

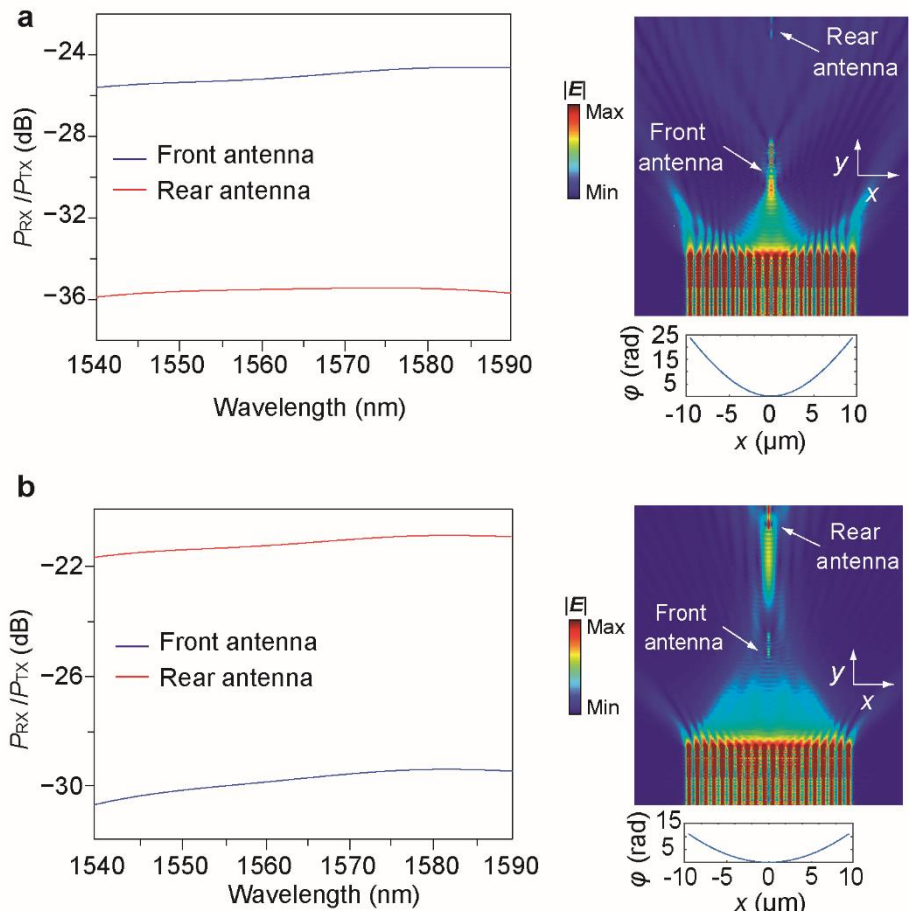

Figure 7. Depth-selective bridging transmission scheme (CST simulations) (**a**), (**b**). By varying the input phases φ of a 20-antenna array, radiated energy can be focused not only at different angles (as in beam steering) but also at different depths. As an example, two receiving antennas are placed at (**a**) (x = 0, y = 10) μm and (**b**) (x = 0, y = 25) μm. Depending on the employed phase profile, the radiated power is sent to the front or rear antenna, see left column. The E-field distribution (λ = 1550 nm) and the associated phase profile for both configurations is shown in the right column

To further illustrate the possibility of controlling radiated beams via wireless silicon photonics, we theoretically developed a device able to generate reconfigurable tailor-made interference patterns. To this end, we designed a 20-element array of a new configuration of tapered antennas with a tip width of 300 nm, engineered to exhibit a directivity of ~10 dB. This lower directivity value is more convenient in this case to favor the creation of multiple-interference waves and fully exploit the optical antenna array concept. We concentrated on achieving light focusing with a reconfigurable focal point position by imposing a hyperbolic phase profile on the emitting array antennas (see Supplementary Information). Such a device can confine radiated energy not only in angle but also in depth, as shown in the example of Figure 7. Here, we show that by tuning the phase of the antennas, it is possible to send radiated energy either to a nearby detector or to a second one behind it (in which case the first detector is bridged), with a crosstalk of approximately -10 dB in both cases. Consequently, one could implement

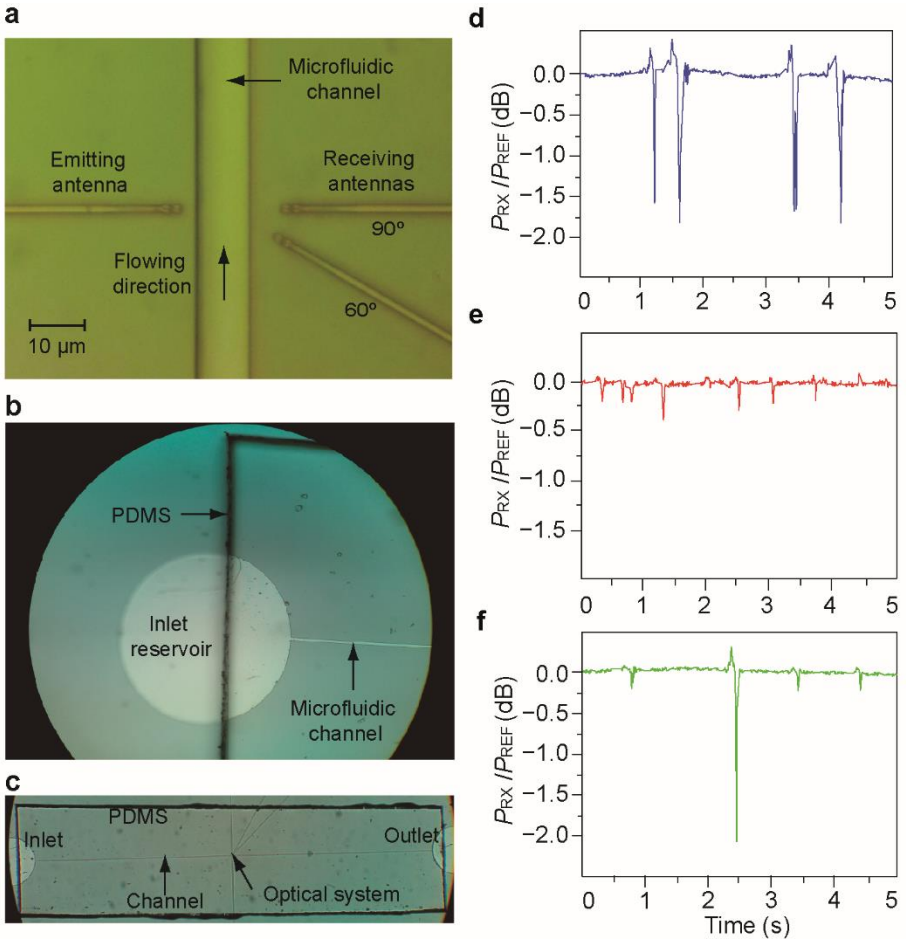

Figure 8. Experimental flow cytometer for microparticle characterization. (**a**) Optical microscope image of the fabricated device. (**b**) Optical microscope image of the inlet reservoir and part of the microfluidic channel. The border of the top PDMS layer can also be observed. (**c**) Complete microfluidic system. The position of the optical system (not visible at this scale) is also indicated. (**d-f**) Power time-dependent efficiency measured at 60° for 2-µm (d), 1-µm (e), and a mixed solution of polystyrene microspheres (f). The received power when no particles are flowing is taken as the reference (P_{REF}).

functionalities not addressable by guided photonics, such as on-chip 2D-selective optical detection schemes (as opposed to the 1D-selective capacities of beam-steering devices), radiating behind "obstacles", or 2D-space mapping.

As a final example, we conducted an additional experiment to demonstrate the potential of the proposed wireless architecture for lab-on-a-chip applications. Inspired by the technique employed in flow cytometry (7), we designed and fabricated an on-chip hydrodynamic parametric analysis system in which different types of microparticles can flow through a microfluidic channel and be simultaneously illuminated by a narrow beam. The main goal was to classify the flowing particles according to their unique time-dependent scattered-field signatures. To this end, we incorporated an optical subsystem into the chip consisting of a highly directive emitting antenna (inverted taper + 2 directors) and two identical receiving antennas connected to standard strip waveguides (Figure 8a). One of the receiving antennas collects the power at 90° and is used for

alignment/calibration purposes. The second receiving antenna measures the scattered field at 60°, which enables us to classify the particles. In addition, a microfluidic channel was built to allow the particles to flow in between the antennas. To build the channel, a 10-μm-wide 4-μm-deep trench was opened in the SiO_2 region between the emitting and receiving antennas, and subsequently sealed by placing a 150-μm polydimethylsiloxane layer atop (Figure 8b). A couple of inlet and outlet reservoirs providing access to the channel completes the microfluidic subsystem (Figure 8c). To test the device, we used polystyrene microspheres (a standard benchmark for calibrating flow cytometers) with two different diameters (1 and 2 μm) in an aqueous solution with a concentration of 1:100 (2% solids). Capillary forces ensure that the solution fills the channel and the microspheres flow between the antennas when casting a solution drop into the inlet reservoir. To learn the characteristic scattered-field signature of each kind of microsphere, we prepared two different solutions including either 1-μm spheres or 2-μm spheres alone. Both signatures appear in the form of a dip, of approximately 2 dB in the case of the large microspheres and 0.25 dB in the case of the small ones (Figure 8d,e). The signatures are exclusive, as no 2 (0.25) dB peaks were observed when flowing the 1-μm (2-μm) sphere. Finally, a flow of an equally mixed solution containing both types of particles was used (Figure 8). In this case, we were able not only to detect when a particle goes through the optical link (due to the presence of a dip) but also easily classify the particle, *i.e.*, identify its size, depending on the magnitude of the measured dip. Since the optical system is not in physical contact with the target, it can be reused an unlimited number of times.

Currently, there are two main approaches to microflow cytometers. The first one uses optical fibers to illuminate the particles and collect the scattered field (8, 42), resulting in bulky devices with potential losses and failure of discrete component interfaces. A second more compact and integrated approach uses focusing components such as lenses or multimode interference devices (to achieve a reduced beam waist and resolve small particles) with a typical lateral size in the mm-scale (42-44). Outstandingly, the directive nature of our illuminating antenna implies that low-divergent focused beams can be generated (the beam full width at half maximum for our experimental configuration is ~ 4 μm at the center of the channel). This allows us to resolve very small particles (1-μm diameter microspheres remain as the smallest target detected so far with integrated on-chip devices) without requiring large focusing structures (42), which entails a promising solution for sub-micron particle detection. Therefore, the proposed device constitutes a low-cost chip-integrated type of flow cytometer, whose main advantage over existing solutions is its extremely reduced footprint (only a few 0.64×14 μm^2 antennas), while exhibiting state-of-the-art precision. Specifically, a dramatic footprint reduction of four orders of magnitude with respect to the most compact previous designs is achieved (42-44), significantly minimizing fabrication time, energy and potential errors. Moreover, the absence of optical fibers in our device simplifies both the packaging and the automation of the manufacturing process. The use of SOI

fully integrated structures enables the possibility of easy fabrication, assuring a prompt mass production of point-of-care devices. Finally, the high density of detectors allowed by the small size of the antennas permits a finer scattered-field sampling angular resolution, resulting in a more accurate classification system.

A final comment on the role of the employed antenna directors: Although the measured ~5-dB link efficiency enhancement provided by these elements (~3 dB/antenna according to our calculations, see Figure 3b) could have a limited impact on the global system performance for long links with high propagation losses (*e.g.*, with $\eta_P \approx 47$ dB for $d = 0.8$ mm), for short links with low propagation losses (*e.g.*, for crossings or short-link switches), a 5-dB improvement can be crucial, for example, to fulfill a given BER specification. Additionally, the enhancement provided by the directors affects other important features of the proposed devices. For instance, a bare inverted taper antenna exhibits a broader radiation pattern and, consequently, introduces higher crosstalk values in applications such as the proposed crossing structure (the crosstalk at 30° associated with the inverted taper antenna without directors would be ~6 dB higher than that associated with the 2-director antenna). For the same reason, the directors also influence the lateral size of the radiated beam. For example, without the directors, the beam waist in the studied cytometry application would increase from 4 to 6 μm, considerably limiting the minimum resolvable particle size.

CONCLUSIONS

The proposed model of a wireless optical system provides a CMOS-compatible on-chip platform supporting a wide range of application scenarios that are less manageable using traditional guided architectures or previous plasmonic or dielectric antenna configurations. In addition to the construction of flexible and reconfigurable networks for classical and quantum HPCs and high-speed communications, these systems could find applications in other fields, such as the generation of complex beams for material processing and optical tweezing (10). From a lab-on-a-chip perspective, the compact and versatile nature of the proposed approach could facilitate a high-density, robust and resilient integration of different laboratory equipment – in addition to flow cytometry, dynamic light scattering, Raman spectroscopy and gas chromatography are interesting possibilities – together with signal processing systems and other functionalities on the same chip (with the potential of performing a large number of simultaneous measurements), that paves the way to point-of-care clinical diagnosis and portable chemical, biological or medical research equipment.

CONFLICT OF INTEREST

The authors declare no conflict of interest.

ACKNOWLEDGMENTS

This work was supported by the EU-funded FP7-ICT project PHOXTROT (n° 318240) and Generalitat Valenciana's PROMETEO grant NANOMET PLUS (PROMETEO II/2014/34). C.G.-M. acknowledges support from Generalitat Valenciana's VALi+d postdoctoral program (exp. APOSTD/2014/044). We thank David Zurita for his help in the design of the data acquisition code for the sensing application and Francisco Cuesta for useful discussions.

AUTHOR CONTRIBUTION

C.G.-M. and S.L. proposed the new dielectric antenna concept, developed the theory, designed and conducted the experiments, analyzed the data and prepared the manuscript. A.B. designed the experimental modulation set-up. A.G. and L.B. developed the fabrication process of the silicon samples. A.B., S.M. and L.S. contributed to the simulations and experiments. N.S fabricated the PDMS layers and participated in the development of the sensing experiment. J.M. conceived and proposed the concept of multipurpose on-chip wireless optical systems, analyzed the data and suggested improvements to the manuscript. All authors discussed the results.

REFERENCES

1. Kirchain R, Kimerling R. A roadmap for nanophotonics. *Nat. Photonics* **1**, 303-305 (2007).
2. Fan XD, White IM. Optofluidic microsystems for chemical and biological analysis. *Nat. Photonics* **5**, 591-597 (2011).
3. Zhuang LM, Roeloffzen CGH, Meijerink A *et al*. Novel ring resonator-based integrated photonic beamformer for broadband phased array receive antennas—Part II: experimental prototype. *J. Lightw. Technol.* **28**, 19-31 (2010).
4. Yu NF, Capasso F. Flat optics with designer metasurfaces. *Nat. Mater.* **13**, 139-150 (2014).
5. Condrat C, Kalla P, Blair S. Crossing-aware channel routing for integrated optics. *IEEE Trans. Comput-Aided Design Integr. Circuits Syst.* **33**, 814-825 (2014).
6. Lee BG, Rylyakov AV, Green WMJ *et al*. Monolithic silicon integration of scaled photonic switch fabrics, CMOS logic, and device driver circuits. *J. Lightw. Technol.* **32**, 743-751 (2014).
7. Robinson JP, Roederer M. Flow cytometry strikes gold. *Science* **350**, 739-740 (2015).
8. Mao XL, Nawaz AA, Lin SC *et al*. An integrated, multiparametric flow cytometry chip using "microfluidic drifting" based three-dimensional hydrodynamic focusing. *Biomicrofluidics* **6**, 024113 (2012).
9. Schurr JM. Dynamic light scattering of biopolymers and biocolloids. *CRC Crit. Rev. Biochem.* **4**, 371-431 (1977).
10. Padgett M, Bowman R. Tweezers with a twist. *Nat. Photonics* **5**, 343-348 (2011).

11. Haurylau M, Chen GQ, Chen H *et al*. On-chip optical interconnect roadmap: challenges and critical directions. *IEEE J. Select. Top Quantum. Electron.* **12**, 1699-1705 (2006).
12. Chan JN, Hendry G, Biberman A *et al*. Architectural exploration of chip-scale photonic interconnection network designs using physical-layer analysis. *J. Lightw. Technol.* **28**, 1305-1315 (2010).
13. Vlasov Y, Green WMJ, Xia FN. High-throughput silicon nanophotonic wavelength-insensitive switch for on-chip optical networks. *Nat. Photonics* **2**, 242-246 (2008).
14. Novotny L, van Hulst N. Antennas for light. *Nat. Photonics* **5**, 83-90 (2011).
15. Fischer H, Martin OJF. Engineering the optical response of plasmonic nanoantennas. *Opt. Express* **16**, 9144-9154 (2008).
16. Dregely D, Taubert R, Dorfmüller J *et al.* 3D optical Yagi-Uda nanoantenna array. *Nat. Commun.* **2**, 267 (2011).
17. Ni XJ, Emani NK, Kildishev AV *et al*. Broadband light bending with plasmonic nanoantennas. *Science* **335**, 427 (2012).
18. Koenderink AF, Alù A. Polman A. Nanophotonics: Shrinking light-based technology. *Science* **348**, 516-521 (2015).
19. Polman A. Plasmonics applied. *Science* **322**, 868-869 (2008).
20. Brongersma ML, Shalaev VM. The case for Plasmonics. *Science* **328**, 440-441(2010).
21. Alù A, Engheta N. Wireless at the nanoscale: optical interconnects using matched nanoantennas. *Phys. Rev. Lett.* **104**, 213902 (2010).
22. Solís DM, Taboada JM, Obelleiro F *et al*. Optimization of an optical wireless nanolink using directive nanoantennas. *Opt. Express* **21**, 2369-2377 (2013).
23. Dregely D, Lindfors K, Lippitz M *et al.* Imaging and steering an optical wireless nanoantenna link. *Nat. Commun.* **5**, 4354 (2014).
24. Curto AG, Volpe G, Taminiau TH *et al.* Unidirectional emission of a quantum dot coupled to a nanoantenna. *Science* **329**, 930-933 (2010).
25. Sun J, Timurdogan E, Yaacobi A *et al*. Large-scale nanophotonic phased array. *Nature* **493**, 195-199 (2013).
26. Van Acoleyen K, Bogarets W, Jágerská J *et al.* Off-chip beam steering with a one-dimensional optical phased array on silicon-on-insulator. *Opt. Lett.* **34**, 1477-1479 (2009).
27. Van Acoleyen K, Rogier H, Baets R. Two-dimensional optical phased array antenna on silicon-on-insulator. *Opt. Express* **23**, 13655-13660 (2010).
28. Rodríguez-Fortuño FJ, Puerto D, Griol A *et al.* Sorting linearly polarized photons with a single scatterer. *Opt. Lett.* **39**, 1394-1397 (2014).
29. Krasnok AE, Miroshnichenko AE, Belov PA *et al*. All-dielectric optical nanoantennas. *Opt. Express* **20**, 20599-20604 (2012).
30. Filonov DS, Krasnok AE, Slobozhanyuk AP *et al.* Experimental verification of the concept of all-dielectric nanoantennas. *Appl. Phys. Lett.* **100**, 201113 (2012).
31. Cárdenas J, Poitras CB, Robinson JT *et al.* Low loss etchless silicon photonic waveguides. *Opt. Express* **17**, 4752-4757 (2009).
32. Balanis CA. *Antenna Theory: Analysis and Desig*n. New York: Wiley, 1982.

33. Kosako T, Kadoya Y, Hofmann HF. Directional control of light by a nano-optical Yagi-Uda antenna. *Nat. Photonics* **4**, 312-315 (2014).
34. Subbaraman H, Xu XC, Hosseini A *et al.* Recent advances in silicon-based passive and active optical interconnects. *Opt. Express* **23**, 2487-2511 (2015).
35. Della Corte FG, Esposito Montefusco M, Moretti L *et al.* Temperature dependence analysis of the thermo-optic effect in silicon by single and double oscillator models. *J. Appl. Phys.* **88**, 7115-7119 (2000).
36. Chu T, Yamada H, Ishida S *et al*. Compact 1 × *N* thermo-optic switches based on silicon photonic wire waveguides. *Opt. Express* **13**, 10109-10114 (2005).
37. Wang WJ, Zhao Y, Zhou HF *et al*. CMOS-Compatible 1 × 3 silicon electrooptic switch with low crosstalk. *IEEE Photon. Technol. Lett.* **23**, 751-753 (2011).
38. Cui KY, Zhao Q, Feng X *et al.* Ultra-compact and broadband 1×4 thermo-optic switch based on W2 photonic crystal waveguides. Proceedings of 2005 Opto-Electronics and Communications Conference; 28 June-2 July 2015; Shanghai. IEEE: Shanghai, 2015.
39. Lee BG, Dupuis N, Pepeljugoski P *et al.* Silicon photonic switch fabrics in computer communications systems. *J. Lightw. Technol.* **33**, 768-777 (2015).
40. Song WW, Gatdula R, Abbaslou S *et al*. High-density waveguide superlattices with low crosstalk. *Nat. Commun.* **6**, 7027 (2015).
41. Melati D, Morichetti F, Gentili GG *et al*. Optical radiative crosstalk in integrated photonic waveguides. *Opt. Lett.* **39**, 3982-3985 (2014).
42. Zhang YS, Watts BR, Guo TY *et al*. Optofluidic device based microflow cytometers for particle/cell detection: a review. *Micromachines* 7, 70 (2016).
43. Kotz KT, Petrofsky AC, Haghgooie R *et al.* Inertial focusing cytometer with integrated optics for particle characterization. *Technology (Singap. World Sci.)* 1, 27-36 (2013).
44. Hunt HC, Wilkinson JS. Multimode interference devices for focusing in microfluidic channels. *Opt. Lett.* 36, 3067-3069 (2011).

Supplementary Information
On-chip wireless silicon photonics: From Reconfigurable Interconnects to Lab-on-Chip Devices

Carlos García-Meca*, Sergio Lechago*, Antoine Brimont, Amadeu Griol, Sara Mas, Luis Sánchez, Laurent Bellieres, Nuria S. Losilla and Javier Martí

Nanophotonics Technology Center, Universitat Politècnica de València, 46022 Valencia, Spain.
* These authors contributed equally to this work.
Correspondence: J. Martí, Email: jmarti@ntc.upv.es

Numerical simulations

To verify the reliability of the directivity calculation of the antenna and the dielectric waveguides based on Huygens principle, we simulated the directivity of some of the studied structures in CST Microwave Studio, obtaining a good agreement between both methods. The simulation and optimization of the response of the designed antennas and directors was also performed using CST Microwave Studio. This includes the calculation of electromagnetic fields (from which the directivity can be obtained with the Huygens method) and the antenna total efficiency and reflectance. Finally, this commercial suite was also employed to obtain some of the results related to the beam steering and sensing applications. In all simulations, CST's time domain solver and a hexahedral mesh were used. Standard waveguide ports were set up at the input and output facets to simulate infinitely long waveguides. The input ports were configured to excite the fundamental TE mode of the feeding waveguides, while the output ones collect the power transmitted to the corresponding output waveguides. The rest of the computational domain was terminated by perfectly matched layers (open boundaries) to avoid undesirable reflections (see Figure S1).

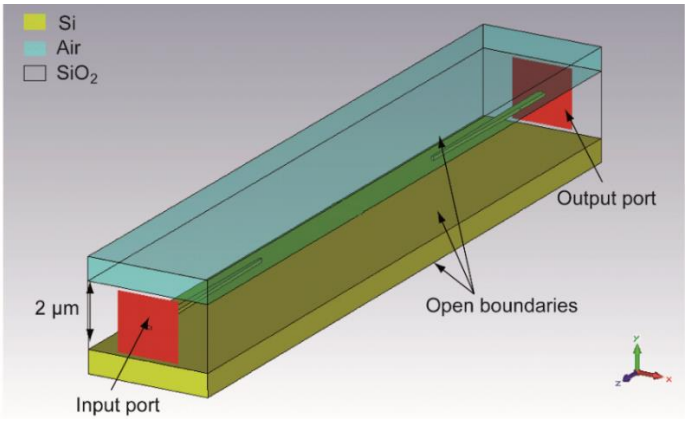

Figure S1: Example of the simulation set-up used in CST Microwave Studio.

Modulation setup and data transmission measurements

Figure S2 shows a scheme of the set-up employed for the experiment on data transmission. Measurements were carried out using a commercial $LiNiBO_3$ modulator fed with a 40 Gbit·s^{-1} non-return to zero (NRZ) pseudo-random bit sequence (PRBS 2^{31}-1) delivered by a bit pattern generator (SHF BPG 44E). The electrical signal was amplified through a broad bandwidth driver amplifier (DC to 40 GHz) to achieve a voltage swing of ~5 V_{pp} and combined to a 1.7 V DC offset to ensure the modulator is biased at quadrature. The input Gbit·s^{-1} modulated signal was then coupled in and out the silicon chip (DUT) via grating couplers, with typical insertion losses below 9 dB at λ = 1550 nm (see Figure S3). In addition, silicon tapers were employed to couple light from the grating to standard 450 nm-wide strip waveguides and vice versa. These elements add an almost negligible penalty (as compared to the rest of the system) lower than 0.5 dB. The signal transmitted through the link was photodetected by a 40 GHz Digital Communication Analyser (Infiniium DCA-J 86100C).

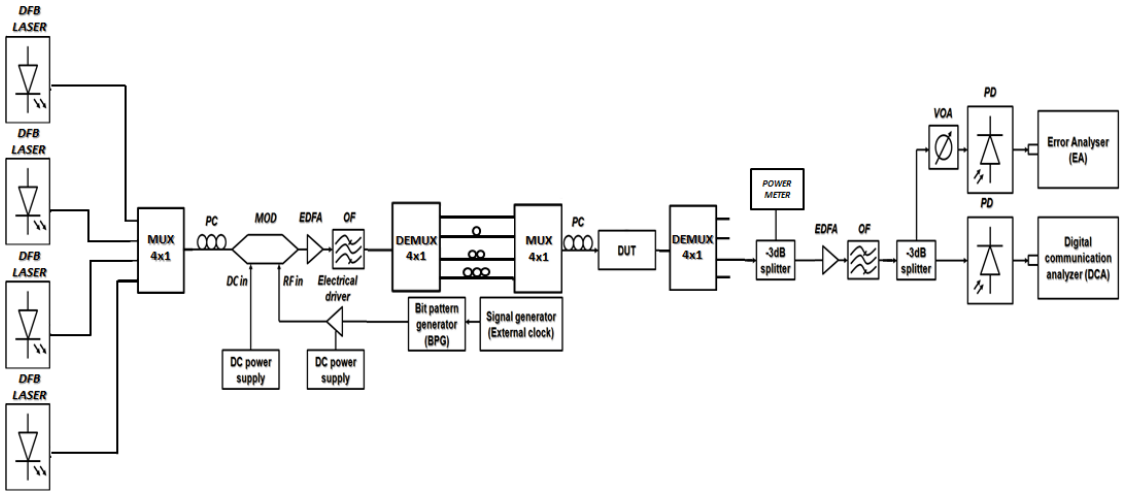

Figure S2: Experimental setup for data transmission

The bit-error rate was then measured by means of a 75 GHz photodiode connected to the Error Analyser (SHF EA 44) and evaluated as a function of decreasing optical power received at the photodetector. Four distributed feedback lasers (DFB) centred at the ITU wavelengths ranging from 1548.51 nm (CH 36) to 1550.92 (CH 33) were employed to inject light up to 160 Gbit·s^{1} in the modulator. Note that it was not possible to carry out a data transmission performance at higher rates (we are able to modulate up to 40 Gbit·s^{-1} with a single laser) due to the number of DFB lasers available in the laboratory. Experimental eye diagrams [pattern formed by an oscilloscope, which consists of repetitively sampled superimposed random digital data transitions ("0" to "1" and "1" to "0") produced by a given device] were retrieved for both data transmission rates (Figure S3). It is worth mentioning that to obtain the results in Figure 4a, an external cavity tuneable laser

(ECL) with a launch power of 1 mW (0 dBm) was used to measure the experimental performance of the wireless links. By means of the ECL we are able to scan frequencies that are not available with the use of DFB lasers as a result of their lack of tuneability.

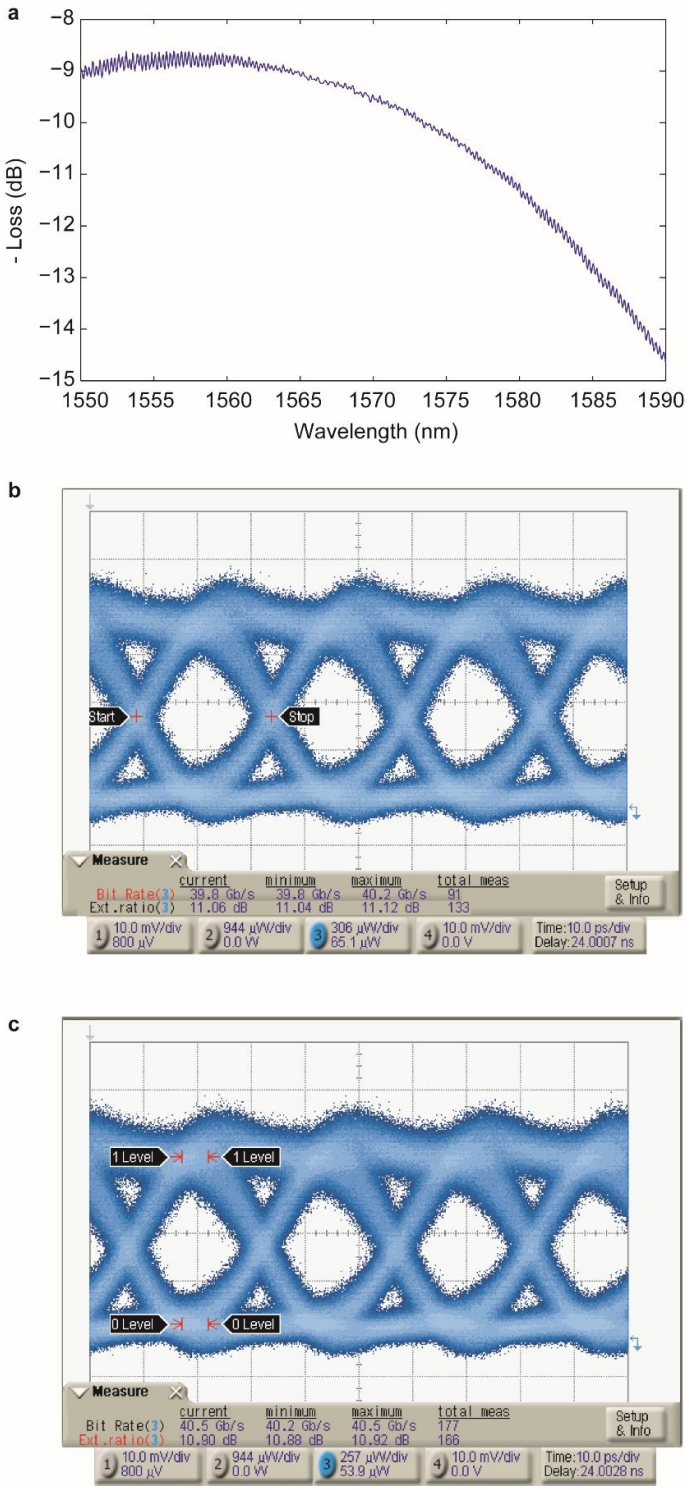

Figure S3: Measured grating coupler loss and eye diagrams. **a**, Measured wavelength-dependent losses introduced by a fabricated waveguide-based link, including the input and output grating couplers. The couplers were optimized to reach a minimum around 1550 nm. **b**, Eye diagram for the 40 Gbit·s^{-1} data transmission experiment. **c**, Eye diagram for the 160 Gbit·s^{-1} data transmission experiment.

To conclude, it is worth mentioning that there appears a low-amplitude ripple in the measurements of Figure 4. This kind of oscillation typically arises as a result of the cavity formed between the output fiber-grating coupler interface and another point in the device. Although reflections at the receiving antenna are very low, this is probably the other end of the cavity, since the periodicity or free spectral range (FSR) of the measured oscillations (~0.5 nm) agrees with the theoretical FSR = $\lambda^2 / (2n_g l_C)$ of a cavity with the same length l_C as that between the antenna and the grating (1050 μm), assuming an overall group index n_g = 2.305 (equal to that of a strip waveguide at λ = 1550 nm).

Calculation of the switching power

In order to measure the switching power, usually defined as the power required to produce a phase shift of $\boldsymbol{\pi}$ under DC conditions, we fabricated a Mach-Zehnder Interferometer (MZI) with a nanoheater (identical to those employed in the reconfigurable beam steering device) placed over one of the MZI arms. As shown in Figure S4, this parameter was found to be 8.3 mW. The reconfigurable beam steering device requires three simultaneous active heaters and the total power needed to aim the beam at any of the side antennas was approximately twice the MZI switching power. Regarding switching time, we estimated the MZI rise (10% to 90% of the output optical power) and fall (90% to 10%) times by applying a 33 KHz RF square wave voltage signal to the heater. We employed a BK 3011B source to produce the RF signal and a Rigol DG1000Z oscilloscope to monitor the MZI output power. It is worth mentioning that special RF probes are required to drive the heaters in this case. The measured rise and fall times were 5.2 μs and 1.5 μs, respectively (see Figure S4), with an extinction ratio of 17 dB. Note that we could not directly measure these values on the beam steering device, as we do not have enough RF probes available in our laboratory to drive all the heaters simultaneously. In any case, the beam steering device time response is expected to be very similar to that of the MZI. As mentioned in the main text, the measured values of both switching power and time are considerably low, yielding a very good figure of merit of 43.16 mW·μs, which is in line with current state of the art[1-4].

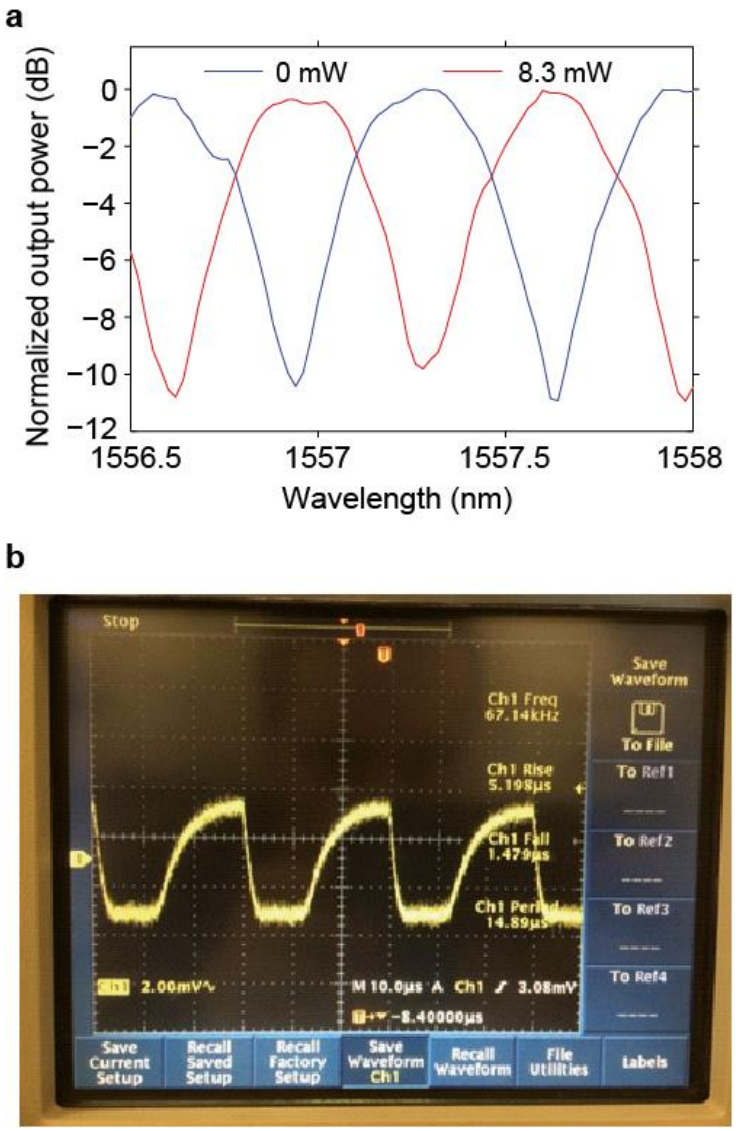

Figure S4: Switching power and switching time. **a**, Normalized MZI output power as a function of wavelength for the case in which no driving electrical power is applied and for the case in which an 8.3 mW DC signal is applied, which induces a π phase shift. **b**, Response of the MZI to a square wave voltage signal applied to the heater. The rise and fall times are shown.

Directivity calculation using Huygens method

According to the field equivalence or Huygens principle, the radiated fields outside a closed surface *S* surrounding all electromagnetic sources can be obtained from the knowledge of the field tangential components on that surface[5]. In particular, the fields outside this surface are the same as the ones produced by the following electric and magnetic current densities

$$\mathbf{J} = \mathbf{n} \times \mathbf{H}$$

$$\mathbf{M} = -\mathbf{n} \times \mathbf{E},$$

where **E** and **H** are the electric and magnetic fields over the surface *S* with normal **n** (Figure S5).

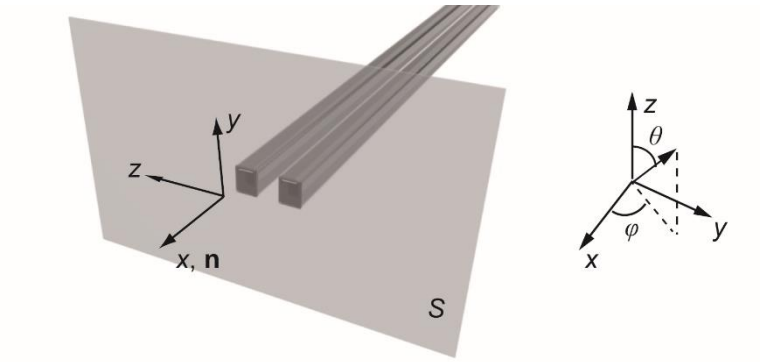

Figure S5: Example of Huygens surface *S* used in the calculation of the directivity of a slot waveguide. The effective currents associated with the fields radiated by the waveguide lie on *S*. In the chose coordinate system, the normal **n** points in the *x*-direction.

The radiated far fields can then be obtained from the following radiation vectors

$$\mathbf{N} = \int_S \mathbf{J}\, e^{i\mathbf{kr}} \boldsymbol{ds}$$

$$\mathbf{L} = \int_S \mathbf{M}\, e^{i\mathbf{kr}} \boldsymbol{ds}$$

We are mainly interested in the far-field radiated power, which is proportional to the radiation intensity $K(\theta,\varphi)$ (the power radiated from an antenna per unit solid angle in a given direction[6]):

$$K = \frac{\eta}{4\pi\lambda^2}\left(\left|\mathbf{N}_\theta + \left(\mathbf{L}_\varphi/\eta\right)\right|^2 + \left|\mathbf{N}_\varphi - \left(\mathbf{L}_\theta/\eta\right)\right|^2\right)$$

from which the radiation pattern and directivity $D(\theta,\varphi)$ associated with **J** and **M** can be readily obtained (η is the background medium impedance), where $D(\theta,\varphi)$ is defined as the ratio of the radiation intensity in a given direction from the antenna to the radiation intensity averaged over

all directions K_0 (note that, by definition, $K_0 = P_{rad}/4\pi$, P_{rad} being the total power radiated by the antenna)[6]

$$D(\theta,\varphi) = \frac{K}{K_0} = 4\pi\frac{K}{P_{rad}}$$

Using the previous equations we can calculate the radiation vectors associated with the fields at the waveguide output plane and hence the corresponding radiation pattern. It is worth mentioning that the directivity of more complex structures with variable transverse dimensions, such as the designed inverted-taper antenna, can be obtained with the Huygens method as well. On the other hand, note that the homogeneous SiO_2 matrix in which the fabricated antennas are embedded has upper and lower bounds. Specifically, its top and bottom interfaces are in contact with air and the Si layer of the SOI wafer, respectively (see Figure S6). Therefore, the secondary rays reflected at these interfaces that reach the receiving antenna might become important. To account for this effect, we calculated the theoretical contribution of these rays using the angle-dependent antenna directivity and the Fresnel reflection coefficients at both interfaces. This results in an additional correction factor C_R for the power efficiency. We chose a value of the SiO_2 uppercladding thickness t_{UP} such that the combined contribution of both reflected rays is almost negligible. However, note that we could engineer t_{UP} so as to use these reflections to our advantage and increase the received power. Finally, we would like to remark that the electromagnetic field at the antenna output surface is mainly concentrated on the SiO_2 core and almost vanishes at the claddings. Consequently, as a very good approximation, the directivity can be calculated from this field assuming that the antenna is embedded in an infinite SiO_2 background.

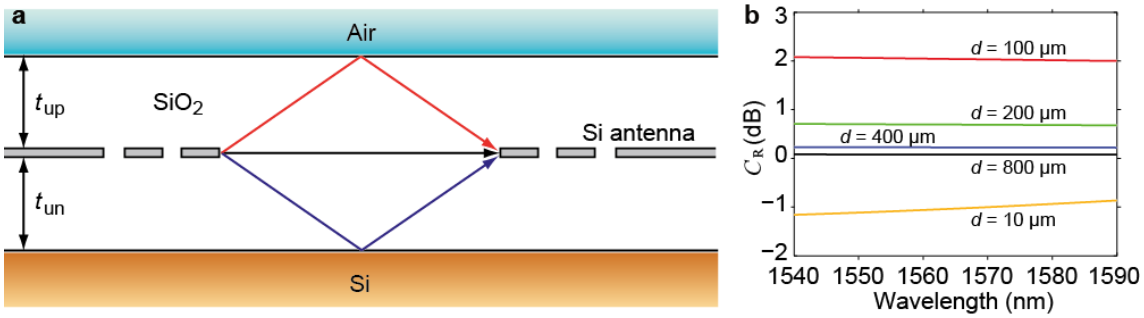

Figure S6: Reflections at the upper and lower interfaces of the SiO_2 matrix in which the antennas are embedded. a, Schematic representation of the employed configuration. The air and Si layers are separated from the antenna by distances $t_{UP} = t_{UN} = 2$ µm. **b,** Coefficient C_R as a function of the wavelength for all the considered link distances. In general, the values of C_R are quite low in all cases and exhibit negligible oscillations that hardly affect the system bandwidth in the considered spectral region.

Design and impact of antenna directors

Trying to mimic the behavior of antenna directors from radiofrequency and microwaves, we studied the possibility of placing different planar structures in front of the inverted-taper antenna to further improve the final directivity, without compromising the overall size. Inspired by previous works on metallic antennas[7,8,9,10] we studied the effect of using a piece of slot dielectric waveguide as a director for the final inverted-taper antenna designed previously (see Figure S7). As mentioned in the main text, since the director electromagnetic response cannot be addressed analytically, its dimensions were optimized numerically. Given the high number of variables, a multi-parametric analysis is not feasible, so we applied a sequential procedure, optimizing one variable at a time. Regarding the separation between both director strips s_D, a very high value will clearly produce no effect, while a too small separation results in a field scattering in undesired directions (Figure S7a). A value of $s_D = 0.34$ μm provided the best results in the final configuration (Figure S7b). As for w_D (strip width), while very narrow strips hardly enhance the directivity (Figure S7c), large values generate strong discontinuities and make the field to concentrate in the strips (Figure S7d). However, we found that the best results are obtained when the field is concentrated on the slot. A good trade-off was obtained for $w_D = 0.18$ μm. In our analysis, we found the director length l_D to be a key design parameter. This can be clearly observed in Figure S7e, where the directivity of the antenna + director configuration is depicted as a function of this parameter. As expected, we verified that, as l_D grows, the system directivity converges to the directivity of an infinite slot waveguide with the dimensions of the director (55 in the studied case), while for very small values of l_D, the directivity is mainly that of the inverted-taper antenna (around 50). However, there is a given length l_{Dopt} in between (approximately 6 μm in this case) for which the system reaches an optimum directivity value higher than 80. This result establishes an important design rule to fix the director length. Aimed at further improving the directivity without increasing the director size, we finally considered the effect of splitting the slot director into several pieces, as in the arrangement of directors in Yagi-Uda antennas. Specifically, we studied a two-cut configuration in which the length of director pieces l_{DP} and cuts l_{DC} was optimized, setting a maximum overall length equal to l_{Dopt}. In the final design with $l_{DP} = l_{DC} \approx 1$ μm, the introduction of the cuts increases the total directivity (see Figure 3 in the main text). Additionally, we have also carried out a study on the impact in the final directivity that single strip waveguide segments would yield when acting as directors. Once again, we have followed a sequential procedure in the optimizations. In particular, we have considered two and three-segment configurations (with no gap between the tapered waveguide and the first segment). We have fixed a maximum overall directors length of 5 μm. The better directivity results were obtained for $l_{DP} \approx l_{DC} \approx 1$ μm (as in the slot case) and narrow strip directors with $w_D = 0.1$ μm (due to fabrication constraints, we did not consider lower widths), being very similar for both

configurations (the three-segment configuration provided an improvement of less than 5% over the two-segment one). For instance, with a 3-segment arrangement, the slot configuration renders a directivity 1.4 times higher than the one produced with a strip scheme (114 versus 82). This justifies the use of the slot configuration for the directors. The influence of w_D in a 3-segment arrangement is shown in Figure S8 for a $l_{DP} \approx l_{DC} \approx 1$ μm configuration.

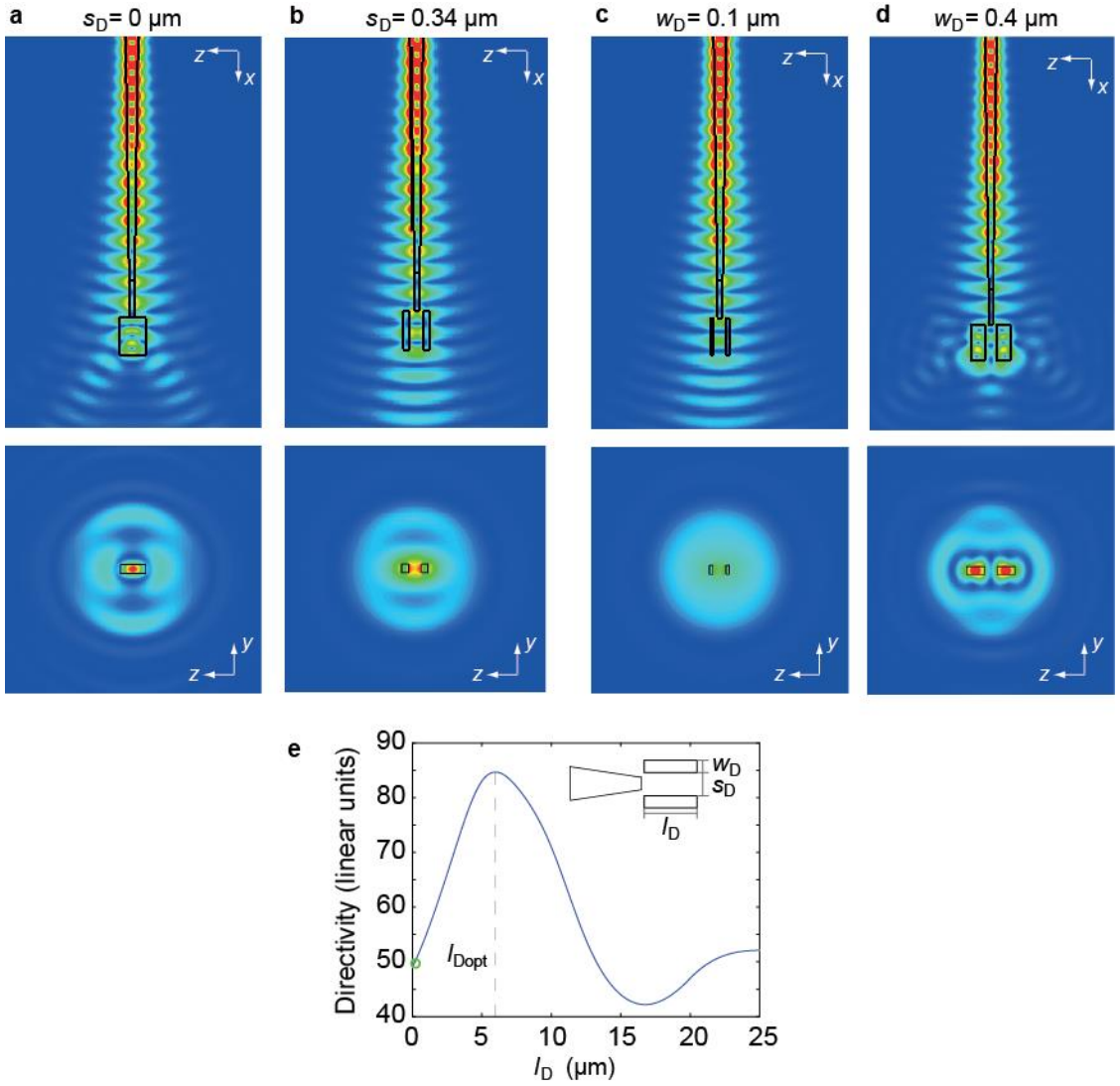

Figure S7: Design of the antenna directors. a, **b**, Influence of s_D. The radiated field is shown for two different values of s_D, keeping the other dimensions unchanged ($s_D + w_D = 0.7$ μm, $l_D = 1$ μm). As in the shown no-gap configuration ($s_D = 0$), small values of s_D give rise to fields radiated in undesired directions. A highly directive beam is obtained for $s_D = 0.34$ μm. **c**,**d**, Influence of w_D. The radiated field is shown for two different values of w_D, keeping the other dimensions unchanged (s_D= 0.34 μm, $l_D = 1$ μm). Low values of w_D (as in **c**, where w_D = 0.1 μm) hardly affect the beam radiated by the inverted taper, which is not as collimated (directive) as in B, where the optimum values of s_D and w_D are used ($s_D = 0.34$ μm, $w_D = 0.18$ μm). In the opposite side, for high values of w_D, the fields concentrate on the strips instead of on the slot, resulting again in undesired high radiation intensity for off-angle directions. An optimum performance was found to occur for w_D= 0.18 μm. **e**, Influence of l_D. The maximum directivity is depicted as a function of l_D for the optimum configuration ($s_D = 0.34$ μm, w_D = 0.18 μm). There is an optimal director length l_{Dopt} that maximizes the directivity. The green circle depicts the directivity of the bare tapered antenna (with no directors).

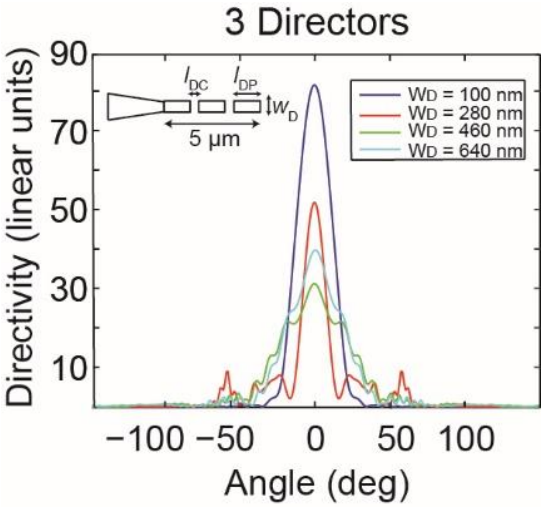

Figure S8: Directivity with strip directors. The influence of w_D in a 3-segment arrangement is shown for a $l_{DP} \approx l_{DC} \approx 1$ μm configuration.

Design of the reconfigurable beam steering device

From classical antenna theory[5], we know that the field radiated by an antenna array is the product of the field radiated by a single antenna and the so-called array factor $\mathrm{AF}(\theta,\varphi)$. Thus, the directivity of the array is

$$D_{\text{array}}(\theta,\varphi) = D_{\text{antenna}}(\theta,\varphi) D_{\text{AF}}(\theta,\varphi) \tag{1}$$

According to the definition of directivity:

$$D_{\text{AF}}(\theta,\varphi) = \frac{\left|\mathrm{AF}(\theta,\varphi)\right|^2}{\int_0^{2\pi}\int_0^{2\pi}\left|\mathrm{AF}(\theta,\varphi)\right|^2 \sin\theta d\theta d\varphi (4\pi)^{-1}}$$

For an *N*-element linear array of equally-spaced identical antennas placed along the *z* axis in which all of them have uniform amplitude with a α progressive phase delay between adjacent antennas, the array factor is given by

$$\mathrm{AF}(\theta,\varphi) = \mathrm{AF}(\theta) = \sum_{n=1}^{N} e^{jn(kd_A\cos\theta+\alpha)},$$

where d_A is the distance between adjacent antennas and *k* is the wavenumber of the radiated medium. In this case, $D_{\text{AF}}(\theta,\varphi) = D_{\text{AF}}(\theta)$ shows a maximum in the direction $\theta_{\max}$, which is related to the progressive phase delay by

$$\alpha = -kd_A\cos\theta_{\max} \tag{2}$$

As mentioned in the main text, for our experiments we used a four-element array ($d_A = 1.65$ μm) made up of inverted-taper antennas with no directors to steer the beam in a 30º range. The

calculated directivity of a single antenna in the *XZ* plane is shown in Figure S9a. In addition,using the previous formulas, we calculated the radiation diagrams of the array factor (Figure S9b) and of the complete array (Figure S9c) for the values of α associated with θ_{max} = 75º (α = -143º)

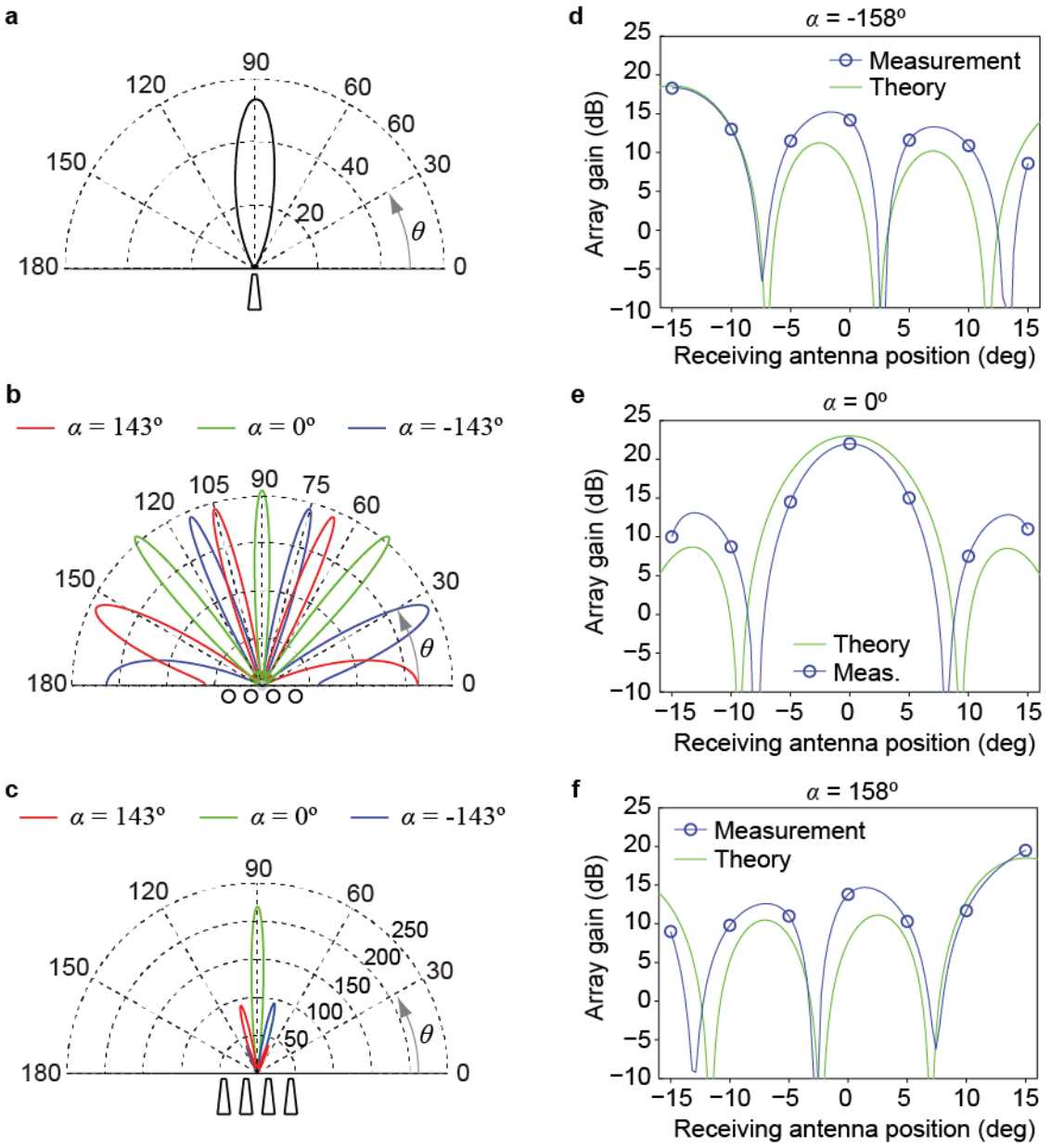

Figure S9: Reconfigurable beam steering device. **a,** Directivity of a single inverted-taper transmitting antenna. **b**, Directivity of the array factor with d_A= 1.65 µm for three different values of α. **c**, Total directivity. **d-f**, Theoretical expected gain (green line) compared with the one measured at the receiving antennas (blue circles) placed at angles -75º, 80º, 85º, 90º, 95º, 100º and 105º, for α = -158º (**d**), α = 0º (**e**), and α = 158º (**f**). The measurements have been interpolated (blue line) for visual clarity.

and θ_{max} = 105º (α = 143º), as obtained from Eq. (2). Note that, in practice, the actual direction in which the total directivity of the array reaches its maximum for a given value of α usually deviates from the value of θ_{max} used in Eq. (2), since the direction of maximum radiated intensity of the array factor is modified by the radiation diagram of a single antenna. To correct this

deviation, we performed full-wave simulations to calculate the total directivity of the array, taking into account the influence of the substrate and the top SiO_2 layer, as well as the interaction between antennas. As a result, we found that the actual values of α that yield a maximum radiation intensity in the directions θ_{max} = 75º and θ_{max} = 105º are α = -158º and α = -158º, respectively. Finally, the theoretical total array gain was obtained by multiplying the directivity by the total antenna efficiency retrieved from the simulations. In Figures S9d-f we compare this theoretical gain with the measured one for the three values of α (0, -158º and 158º), finding an excellent agreement.

Beam Focusing

Two-dimensionally focused spots at a certain focal point (x_0, y_0) can be created by setting a hyperbolic phase profile given by the formula

$$\varphi_i = \frac{2\pi}{\lambda}\left(\sqrt{\left(x_i - x_0\right)^2 + \left(y_i - y_0\right)^2} - C\right),$$

where φ_i is the phase of the *i*-th antenna [located at (x_i, y_i)] and C is a constant that does not alter the focusing effect and that is usually taken to be $C = d_0 = (x_0^2 + y_0^2)^{1/2}$.

REFERENCES

1. Coppola G, Sirleto L, Rendina I, Iodice M. Advance in thermo-optical switches: principles, material, design, and device structure. *Opt Eng* 2011; **50**: 071112.
2. Watts MR, Sun J, DeRose C, Trotter DC, Young RW *et al*. Adiabatic thermo-optic Mach-Zehnder switch. *Opt Lett* 2013; **38**: 733-735.
3. Li X, Xu H, Xiao X, Li Z, Yu Y *et al*. Fast and efficient silicon thermo-optic switching base on reverse breakdown of pn junction. *Opt Lett* 2014; **39**: 751-753.
4. Wang XB, Sun J, Liu YF, Sun JW, Chen CM *et al*. 650-nm 1 × 2 polymeric thermo-optic switch with low power consumption. *Opt Express* 2014; **22**: 11119-11128.
5. Balanis CA. *Antenna Theory: Analysis and Desig*n. New York: Wiley, 1982.
6. 145-2013 - IEEE Standard for Definitions of Terms for Antennas
7. Uda S. High angle radiation of short electric waves. *Proc. IRE* 1927; **15**: 377-385.
8. Novotny L, van Hulst N. Antennas for light. *Nat Photonics* 2011; **5**: 83-90.
9. Dregely D, Taubert R, Dorfmüller J, Vogelgesang R, Kern K *et al.* 3D optical Yagi-Uda nanoantenna array. *Nat Commun* 2011; **2**: 267.
10. Solís DM, Taboada JM, Obelleiro F, Landesa L. Optimization of an optical wireless nanolink using directive nanoantennas. *Opt Express* 2013; **21**: 2369-2377.

PAPER B. HIGH SIGNAL-TO-NOISE RATIO ULTRA-COMPACT LAB-ON-A-CHIP MICROFLOW CYTOMETER ENABLED BY SILICON OPTICAL ANTENNAS

High signal-to-noise ratio ultra-compact lab-on-a-chip microflow cytometer enabled by silicon optical antennas

Sergio Lechago, Carlos García-Meca, Amadeu Griol, Nuria Sánchez-Losilla and Javier Martí

Nanophotonics Technology Center, Universitat Politècnica de València, 46022 Valencia, Spain.
Correspondence: S. Lechago, Email: serlecbu@ntc.upv.es

ABSTRACT

We experimentally demonstrate an all-silicon nanoantenna-based micro-optofluidic cytometer showing a combination of high signal-to-noise ratio (SNR) > 14 dB and ultra-compact size. Thanks to the ultra-high directivity of the antennas (>150), which enables a state-of-the-art sub-micron resolution, we are able to avoid the use of the bulky devices typically employed to collimate light on chip (such as lenses or fibers). The nm-scale antenna cross section allows a dramatic reduction of the optical system footprint, from the mm-scale of previous approaches to a few μm^2, yielding a notable reduction in the fabrication costs. This scheme paves the way to ultra-compact lab-on-a-chip devices that may enable new applications with potential impact on all branches of biological and health science.

INTRODUCTION

The relentless progress of photonic integrated technology has enabled a vast catalogue of new applications able to bring solutions not only in the traditional fields of communications or computing, but also in other areas such as spectroscopy (1), beam shaping and advanced material processing (2), or biomedicine (3). Along this line, we have witnessed how this technology has sparked the development of metadevices (4) and point-of-care (POC) lab-on-a-chip sensors (5), amongst many others. Traditionally, photonic circuits are built upon waveguide-based layout implementations, an acceptable feature for many systems (6), but that in turn provide harsh design rules and usually lead to complex and non-compact device footprints. Additionally, the inherent confined nature of the electromagnetic fields travelling within or over photonic wires limits their ability to interact with the surrounding medium at far-field distances. This stringent characteristic prevents their use in several kinds of biosensors and devices (7), as well as in other applications as, for instance, those related to dynamic microparticle control (8).

The possibility of using wireless devices on a chip has been proposed as an alternative to the typically widespread waveguide-based schemes (9–17). These new wireless systems usually rely on the use of optical nanoantennas, which are able to radiate within a chip, aping the behavior of radiofrequency or microwave antennas. Most of the wireless implementations found in the

literature are based on the use of plasmonic nanoantennas (11–14), a suitable solution to concentrate optical energy in the visible or near-infrared spectrum. Moreover, these devices would potentially enable a bridge to quantum systems or single-photon sources (13), showing a better efficiency than plasmonic nanowires. However, these wireless devices still display strong absorption losses and a poor radiation performance in high frequency bands. Other approaches employ dielectric antennas in grating coupler (15, 16) configurations, only suitable for off-chip interconnects.

Very recently, a new kind of on-chip photonic silicon antenna with a tremendously improved radiation performance was proposed, showing directivities higher than 150 (linear units) and total efficiencies close to 90% (17). Moreover, these dielectric antennas provide low losses and a wide working bandwidth at the telecom wavelengths, while the use of silicon as the constituent material assures their compatibility with the complementary metal-oxide-semiconductor (CMOS) technology. These devices have experimentally proved their suitability as the main building block in several experimental applications ranging from dynamically-reconfigurable wireless pathways to lab-on-a-chip flow cytometers, the object of the present study. Flow cytometry allows the rapid and simultaneous analysis of multiple parameters of live cells in a heterogeneous mix as they flow in a stream through optical or electric signals. This technique has become an essential tool in cell sorting and analysis, with a paramount importance in the treatment of diseases such as AIDS or cancer (18). However, traditional flow cytometers are expensive (with a price that can be of the order of 100.000 US$ for a single unit (19)) and require the presence of specialized staff in their use, implying additional indirect costs. Moreover, traditional flow cytometers demand large amounts of expensive reagents, with complicated processing steps, feature that also entails high maintenance costs (5). Lab-on-a-chip technology is a promising alternative for reducing the cost of biomedical equipment while presenting, at the same time, additional advantages such as yielding more compact implementations (20, 21). As a consequence, there has been an intense research activity to achieve integrated lab-on-a-chip cytometers that use microfluidic technology (microflow cytometers) during the last 15 years (5, 20).

Flow and microflow cytometry usually relies on the use of optical- or impedance-based technology (5, 22). While both schemes offer valuable and complementary information (22), impedance-based systems present some disadvantages as compared to optical ones. For instance, an impedance-based multiparametric analysis can only be performed by using alternating electric current signals with different frequencies, which requires the presence of external function generators and amplifiers (23). In contrast, this can be achieved with optical cytometers just by scanning different angles at a single frequency. Moreover, the use of electric currents entails the possibility of damaging the analyte (24). Additionally, impedance microflow cytometers require the integration of electrodes into the microfluidic channel, which increases the cost and complexity of the device as compared to optical approaches (20). Furthermore, the metals

commonly used to fabricate the electrodes, such as platinum (23) are not CMOS compatible. Most of the current approaches to on-chip microflow cytometry are based on optofluidic devices (5), which synergistically combine integrated photonics with microfluidics in a single chip (termed optofluidic chip) to count, sort or analyze flows of live cells. Within the optical approach, fluorescence and scattering cytometry have been extensively discussed in the literature (5). Fluorescence-based flow cytometry has proved to be a reliable technique to identify and classify biotargets. However, current trends in microflow cytometry are leading to label-free systems (25), as they avoid the cost, time, and required training associated with the labelling process, as well as the use of fluorescent biomarkers that could potentially damage the analyte. To a large extent, research efforts along this line have addressed the miniaturization and the improvement of the integration level of the optical and fluidic subsystems, in order to reduce the cost and enhance portability.

Regarding the optical subsystem, on which we focus in this paper, state-of-the-art on-chip optofluidic microcytometers rely on the use of fibers or microlenses to illuminate the sample and collect the scattered light (5), as this avoids the use of expensive external optical elements and facilitates the alignment of the different system components, as well as the sought size reduction, all of which contribute to minimize costs. Despite the fact that fiber-based devices suppose a notable advance in portability and cost reduction with respect to standard cytometers, the use of fibers requires complex fabrication and packaging steps that hamper the automation of the fabrication process, limiting the cost reduction. Moreover, optical fibers are a source of potential losses and failure at discrete component interfaces. The key to achieve a drastic cost reduction would be to develop devices that can be completely fabricated using standard wafer-scale manufacturing approaches, such as the CMOS technology employed for the production of integrated circuits, which relies on planar processes that allow the automatic fabrication of many devices in parallel (26). Microlens-based optical subsystems are compatible with this approach, representing a lower cost option than fiber-based cytometers (27).

Furthermore, in wafer-scale manufacturing, a reduction of the size of the chip directly decreases its fabrication cost (as well as indirectly, since the tolerance to fabrication defects increases) (26). In this sense, the solution proposed in (17) is based on integrated silicon nanoantennas with a footprint as small as $0.64 \times 14\ \mu m^2$, representing, to our knowledge, the most compact optical subsystem for a microflow cytometer to date, with a notable size reduction (up to four orders of magnitude) with respect to previous approaches (5). This feature, together with the fact that the proposed structures can be fabricated using standard CMOS-compatible silicon-on-insulator (SOI) technology (28, 29) (the best planar fabrication technology for optical chips in many aspects (30)), shows the low-cost nature of this approach. Achieving this level of miniaturization is also important to improve portability, as well as to increase the number of parallel analyses that can be performed within the same chip, and enables a fine angular field

sampling. Moreover, the ultra-directive nature of these structures renders a state-of-the-art particle resolution, exemplified by the experimental characterization and classification of polystyrene microspheres with a diameter as small as 1 μm. Obviously, employing fully integrated antennas inherently avoids the use of fibers and external bulky optical elements usually employed to focus light on chip (31–34). As a consequence, these silicon nanoantennas emerge as an interesting alternative that may supersede microlenses and optical fibers for the realization of low-cost lab-on-a-chip microflow cytometers. Here, taking this previous work a step further, we design and experimentally demonstrate an on-chip microfluidic nanoantenna-based microflow cytometer with a significantly improved SNR (a fundamental parameter that establishes the ability of the device to resolve targets from the noise level), outperforming most previous integrated microflow cytometers (5). To this end, we looked for the reception antenna angle that maximizes the SNR, finding a good agreement between simulations and experiments. The employed configuration constitutes a much more compact version than previous designs (5, 31–34) and competes with the best state-of-the- art SNR shown so far with a label-free detection scheme. Additionally, this implementation provides a very low coefficient of variation (CV) for specific angular directions. All designs and experiments correspond to a wavelength λ = 1550 nm.

THEORETICAL RESULTS AND DISCUSSION

We start by reviewing the working principle of the employed all-silicon nanoantennas, upon which the optical subsystem of the device is built. In particular, we used the antennas proposed (17), which are based on open-ended strip waveguides. The directivity of these structures was modelled via Huygens' principle, following the method typically used in classic microwave and radiofrequency theory (35). This approach directly links the nanowire radiation pattern with the Fourier transform of its mode transverse electric and magnetic fields. A straightforward implication is that less confined modes lead to higher directivities, since the angular extension of the radiation vectors decreases as the spatial extension of the mode increases (17). It was proved that by varying the transverse dimension of these strip wires, the mode confinement can be tuned, thus providing an easy way of tailoring the final directivity of the waveguide-based antenna. In the final configuration of the microflow cytometer we use an antenna consisting of a transition from a standard 450-nm-width 220-nm-height strip silicon wire to a 150-nm-width silicon tip through an inverted taper, which already achieves a directivity as high as 54 (linear units), see Fig. 1(a). Several additional elements (the so-called directors) were placed in front of the antenna to further improve its directivity (17, 36). Fig. 1(a) shows the impact of the number of directors on the antenna directivity. The final configuration is an inverted taper nanoantenna with two directors, see Fig. 1(b), yielding a directivity of 114, enough to fulfil the requirements of our upcoming experiments.

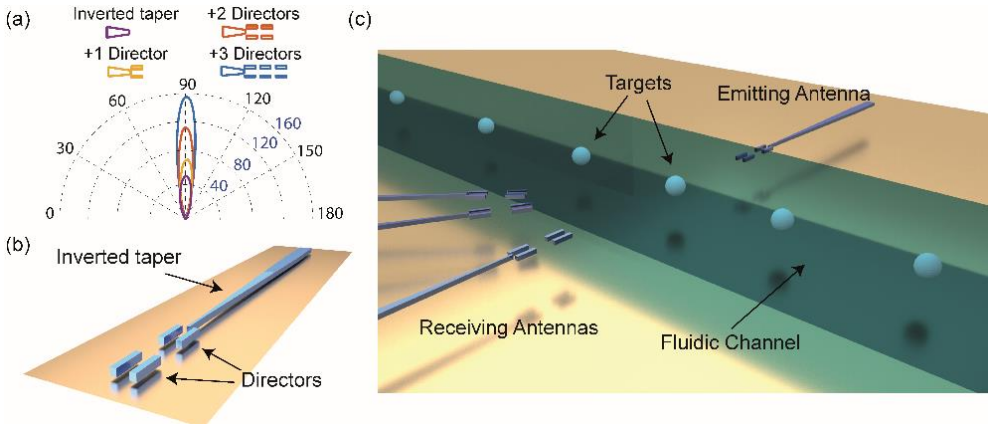

Figure 1. (**a**) Polar directivity diagram of the designed antennas as a function of the number of directors. Blue numbers represent the directivity value while black numbers account for the angular directions. (**b**) Artwork displaying the final antenna configuration used for the experimental microflow cytometer, made up of a silicon inverted taper nanoantenna and two directors. A 2-µm thick layer of SiO_2 covered the antennas in the experiments. (**c**) Scheme of the proposed microflow cytometer based on the use of the designed silicon antennas. The targets flow within the microchannel and the characteristic scattered pulse is retrieved at the receiving set of antennas.

As mentioned before, the ultra-high directive nature of this structure, able to radiate most of the power in a small range of angular directions, avoids the need for bulky devices, such as lenses or multimode interference devices, to produce the needle-like beams required in high-resolution flow cytometry. This outstanding feature provides a reduced footprint in the µm-scale (versus the mm-scale lateral sizes of previous designs (37)), offering a versatile and ultra-compact approach for building microflow cytometers through the scheme shown in Fig. 1(c) (17). In order to determine the quality and performance of flow cytometry-based devices, two of the most relevant parameters are the SNR and the CV. The SNR quantifies the variation in the retrieved signal (voltage or power) when a target is illuminated by a light beam, in relation to a baseline configuration with no targets (noise). On the other hand, the CV stands for the ratio of the standard deviation to the mean of the light signal intensity retrieved for all the events detected during a time lapse for a single direction (5). While the SNR is altered by the experimental performance of the microfluidic and optical subsystems as well as by the electronic devices handling the data processing, numerical simulations can provide accurate qualitative and quantitative information regarding this parameter. However, it must be pointed out that attaining the CV via simulations would be useless since the standard deviation of the scattered light signal of a particle in a single direction will always be zero, yielding an ideal (and unreal in experiments) CV = 0% (hence, this parameter was only retrieved from experimental data). It is well-known that a given particle scatters light differently in each direction. Therefore, the power intensity detected by the receiving antenna depends on the angle at which it is placed. One of the goals of this work was to optimize this angle in order to maximize the SNR.

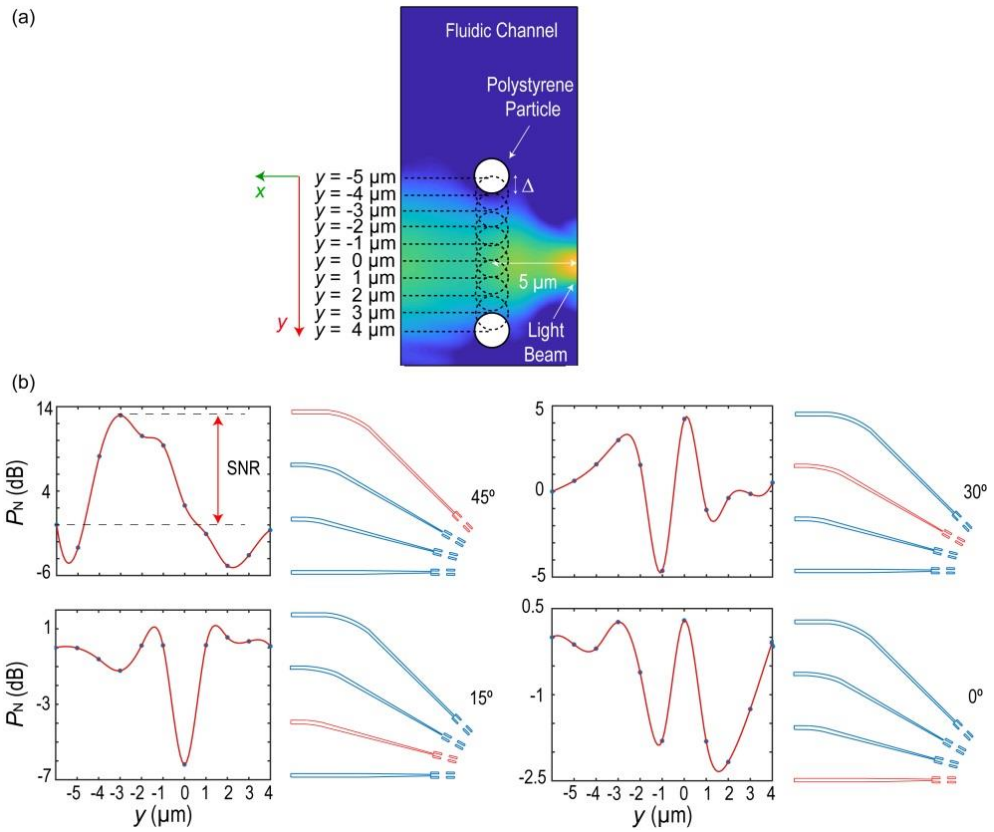

Figure 2. 3D simulations of the electromagnetic power scattered by polysterene microspheres performed with the CST Microwave Studio Suite commercial software. (**a**) Schematic top view of a microfluidic channel where a polystyrene bead is flowing. The light beam radiated by the emitting antenna illuminates the targets (at the center of the channel in the transverse or *x*-direction) for ten different longitudinal positions, from y = -5 µm to y = 4 µm, with steps of Δ = 1 µm. In an experiment, a flowing particle will be in a different position at each instant. Therefore, the pulse obtained by simulating the power received as a function of these set of positions represents a discretized version of the pulse received at the detector as a function of time as a microsphere passes in front of the antenna (up to a horizontal scale factor that depends on the particle speed). (**b**) The power P scattered from the target at each of the 10 positions shown in Fig. 2(a) (events) is retrieved for each receiving antenna. The value of $P_N = 10 \cdot \log10\ (P/P_B)$ associated with each event is represented as a solid circle (P_B accounts for the power of the baseline configuration when no targets are within the channel). The resulting set of circles is interpolated by a red curve, obtaining a different characteristic pulse shape for each of the analyzed reception angles.

To this end, we simulated the power received in a set of antennas placed at different angular directions, which were normalized to the power received in the baseline configuration (*i.e.*, that in which there is no particle in the channel between antennas). The complete considered system consists of an emitting antenna, a 10-µm-wide 4-µm-deep fluidic channel filled with an aqueous solution through which particles flow, and the aforementioned set of receiving antennas. To find the optimal system configuration, we explored the scattered-power signature of polystyrene microspheres (with a diameter of 2 µm), the standard test beads in flow cytometry. In particular, we considered a hub of antennas with an angular separation of 15 degrees (taking the center of the microchannel as the origin). While the study of more angular steps could provide a more accurate estimation of the optimum angle, the particularly time-consuming 3D simulations required to this end (besides the large 3D simulation domain containing all the involved optical

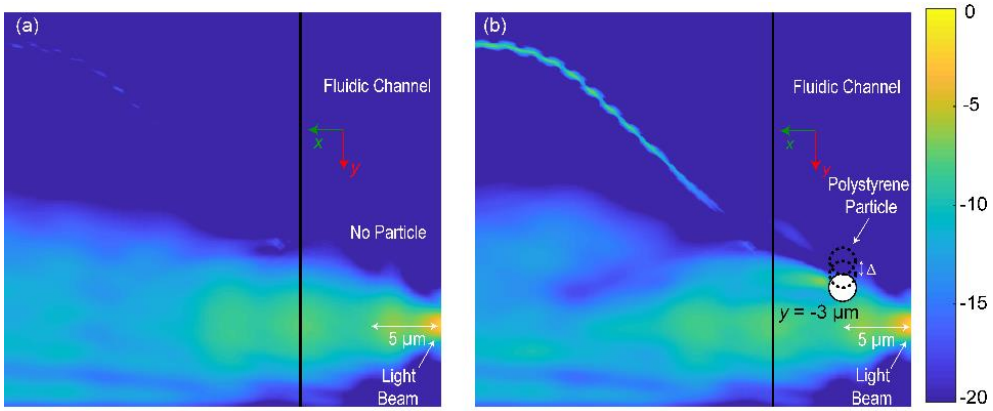

Figure 3. Two-dimensional distribution of the power intensity when no targets are flowing through the channel (**a**) and when the target is located at y = -3 μm for the 45º receiving antenna configuration (**b**). Note that the color bar stands for the power intensity (dB) normalized to the maximum power displayed in these 2D cross sections.

elements, one has to calculate the fields for a considerable number of microparticle positions for each receiving direction) led us to consider this assumable set of directions, which, as we will show below, is enough to obtain a dramatic enhancement of the SNR. Additionally, from an experimental perspective, the chosen step helps us to avoid fabrication limitations and potential errors. Using the configuration shown in Fig. 1(c), polystyrene beads were placed in the middle of the microfluidic channel (x- and z-direction), while different positions in the flowing direction (y-axis) were considered, starting 5 μm away from the emitting antenna position, see Fig. 2(a). At y = ±5 μm, the received power approximately corresponds to the noise level (no microparticle), with further distances providing similar results.

The power scattered at the previously mentioned set of antennas placed at 0º, 15º, 30º and 45º, was numerically retrieved for bead positions from y = -5 μm to y = 4 μm in small increments of Δ = 1 μm, see Fig. 2(b). Regarding the antenna placed at 60º, an extremely low level of intensity below the measurable noise threshold of our laboratory equipment was attained for the baseline configuration, leading us to dismiss this option (and larger angles) in the final set of receiving antennas. Moreover, as obviously expected, antennas placed in a mirrored configuration with respect to the emitting antenna (-15º, -30º and -45º), yielded very similar pulse shapes to those measured for their positive-angle counterparts, not providing additional information of the targets. This feature reduced the angles to be explored to the four previously mentioned directions. As can be seen in Fig. 2(b), there are different and characteristic pulses depending on the direction from which the scattered field of the particle is retrieved. Clearly, the better SNR was attained for the 30º and 45º directions, with a value of ≈ 5 dB for the former and an outstanding ≈ 13-dB figure for the latter. The amplitude and well-defined pulse shape associated with this direction promises to provide the most efficient target identification, yielding unequivocal time-dependent signatures. In particular, it approximately provides a 10-dB enhancement with respect to our

previous design, in which a 30º angle was considered for the receiving antenna (17). This numerical enhancement turned out to be slightly better at the experimental level (see below). To better understand how the particles scatter light when passing through the radiated beam, we numerically calculated the two-dimensional power distribution on the *xy* plane (centered along the *z*-direction with respect to the antennas) associated with polystyrene beads located at several positions for the 45º configuration; see Figs. 3(a) and 3(b). The enhancement of the signal at the receiving antennas is notable for a certain target location (y = -3 µm), justifying the results of Fig. 2. While the subsequent experimental results suggest that particles approximately flow along the channel center line, in order to analyze the influence of a possible offset of the particle position in the *x* and *z* directions, we performed additional simulations in which the particle center was assumed to move along a line with coordinates $x = x_0$ and $z = z_0$ ($x_0 \neq 0$ or $z_0 \neq 0$), for both the 30º and 45º cases. Fig. 4 shows the corresponding simulated pulses. As can be seen, the pulse shape is similar to that of the $x_0 = 0$, $z_0 = 0$ case for some offset values, but varies significantly for other ones. To avoid this variation, the particle must be forced to flow as close as possible to the channel center. This is a basic requirement for flow cytometers, as it also ensures that particles flow in line, preventing multiple particles from going through the light beam simultaneously. It has been demonstrated that this feature can be readily achieved in microflow cytometry via hydrodynamic focusing, based, *e.g.*, on the concept of Dean flow and the use of curved microfluidic channels, which can be fabricated using standard soft lithography (19) and seamlessly incorporated to the studied cytometer.

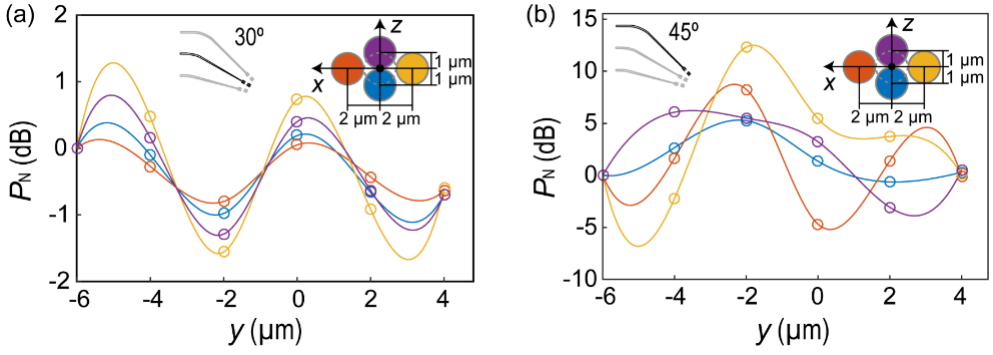

Figure 4. 3D simulations of the electromagnetic power scattered by 2-µm polysterene spheres, with $x_0 \neq 0$ or $z_0 \neq 0$. Four different cases were considered: x_0 = 2 µm, z_0 = 0 µm (orange); x_0 = -2 µm, z_0 = 0 µm (yellow); x_0 = 0 µm, z_0 = 1 µm (purple); x_0 = 0 µm, z_0 = -1 µm (blue). (**a**) Power received at the 30º antenna. (**b**) Power received at the 45º antenna

EXPERIMENTAL RESULTS

Taking into account the previous discussion, we conducted an experiment to demonstrate the large SNR values of the proposed microflow cytometer. In our final device, the wireless deployment is made up of the highly-directive emitting antenna considered above and two other

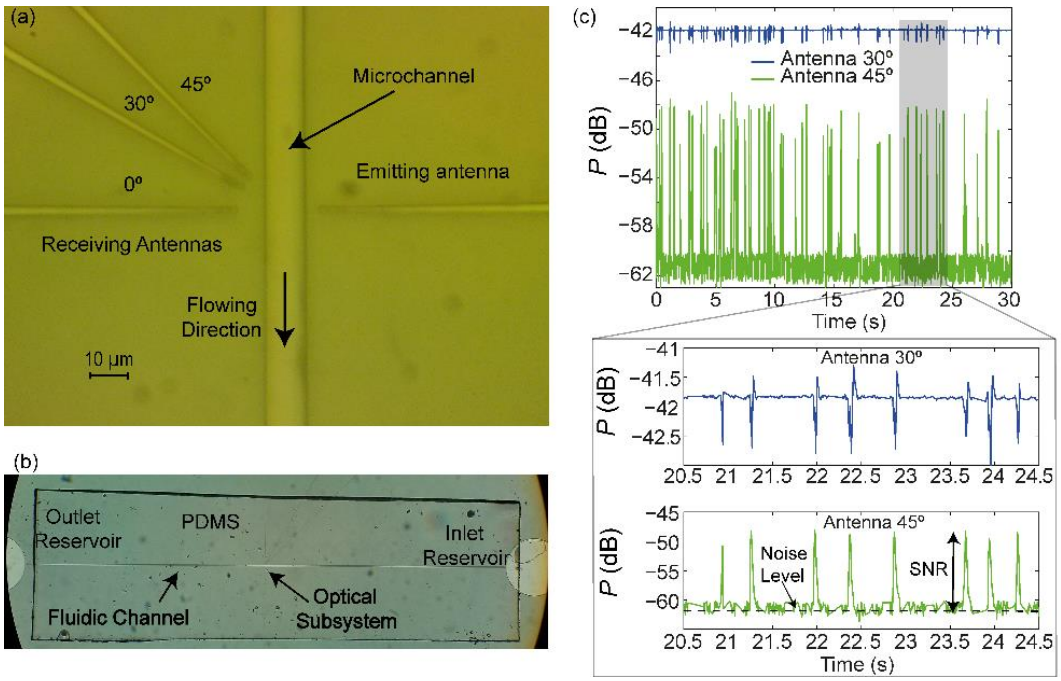

Figure 5. (**a**) Optical microscope image of the fabricated microflow cytometer. (**b**) Optical microscope image of the complete device (except for the grating couplers), including the reservoirs and the microfluidic channel. The border of the top PDMS layer is also displayed. Note that, at this scale, the position of the optical system is not visible. (**c**) Power efficiency (P) simultaneously measured at 30º and 45º during a four-second interval. In this case, $P = 10 \cdot \log 10\ (P_{RX}/P_{TX})$, where P_{TX} is the power injected to the emitting antenna, and P_{RX} is the power retrieved at the receiving antennas. Very similar pulse shapes are measured if compared with those calculated numerically (Fig. 2). The SNR level for the 45º configuration also matches the results anticipated by the simulations.

identical antennas measuring the scattered field at 30º and 45º (the angles for which a better numerical SNR was obtained), see Fig. 5(a). Another antenna placed at 0º was included for calibration purposes. Input and output grating couplers enabled vertical light injection (extraction) to (from) the chip (38). To build the fluidic subsystem, a 10-µm-wide 4-µm-deep trench was directly opened in the SiO_2 region in between the antennas (see the fabrication section below for more details). This subsystem is completed with the incorporation of two inlet and outlet reservoirs; see Fig. 5(b). These structures enable the casting of the solutions within the microfluidic channel, allowing the particles to flow in front of the nanoantennas. Finally, a 150-µm-thick polydimethylsiloxane (PDMS) layer was placed atop this configuration, sealing the device and assuring that the targets do not overflow the fluidic path.

As a consequence, capillary forces ensure that the solution reaches the microchannel and flow the targets between the antennas. To test the device, we used the aforementioned 2-µm polystyrene microspheres in an aqueous solution (10 µl volume, concentration of 0.1 % solids). As noted above, the reason for using this kind of particle is that they are usually employed as benchmarks for calibrating commercial flow cytometers. Particles were injected into the microfluidic channel by means of a manual drop casting on the inlet reservoir with a high-precision micropipette. Since the aim of this work was to improve the SNR by exploring the target time-dependent scattering signature at different angles, achieving high flow rates was unnecessary

(note that the employed scheme does not impose an upper limit for the flow rate, as the scattered power pattern is not affected by the particle speed). Therefore, we designed a basic microfluidic system not including an automated syringe-based pumping flow control. Nevertheless, an external pumping system could be easily included in our device. With this addition, and using a standard high-speed acquisition system (sampling rate in the MHz range) (19), throughput values of the order of thousands of particles per second can be potentially achieved under the conditions of this study (5,19). On the other hand, a high particle concentration could affect the scattered radiation pattern if two consecutive particles in close proximity go through the light beam. Thus, this parameter should be kept under a certain threshold. Another possibility would be to train the classification system (see below) to recognize multi-particle events. The two receiving antennas located at 30º and 45º simultaneously retrieved the characteristic time-dependent scattered-field pulses of these beads as passing in front of the emitting antenna. Focusing on the 45º direction, a well-defined pulse is displayed at each detection event, see Fig. 5(c), yielding SNR figures as high as 14 dB (noise level of -62 dB). Outstandingly, there is an almost qualitative and quantitative perfect agreement between the simulations and the experimental results.

Regarding the 30º direction, the time-dependent shape of the measured pulses was very similar to that of the previous numerical analysis. In particular, the pulse slightly grows at the beginning, then displays a pronounced inverted ramp, and finally grows again; see Fig. 5(c). The qualitative agreement between both simulations and experiment is clear, while displaying some amplitude differences. These results show the importance of choosing a suitable angle for the receiving antenna. In particular, we obtain an SNR improvement of more than 10 dB with respect to our previous experiment just by changing this angle from 30º to 45º. In addition, we calculated the experimental CV for both cases, yielding values of 28.17% and 6.64% in the 45º and 30º directions, respectively. This last figure entails a record regarding the reported CV for previous microflow cytometers where the light signal is retrieved on-chip. Outstandingly, the conducted experiments prove that the ultra-directive beams radiated by the employed nanoantennas are crucial to resolve very small particles, offering a simple route towards sub-micron POC biotarget analysis. Moreover, the obtained state-of-the-art figures of SNR and CV demonstrate that this

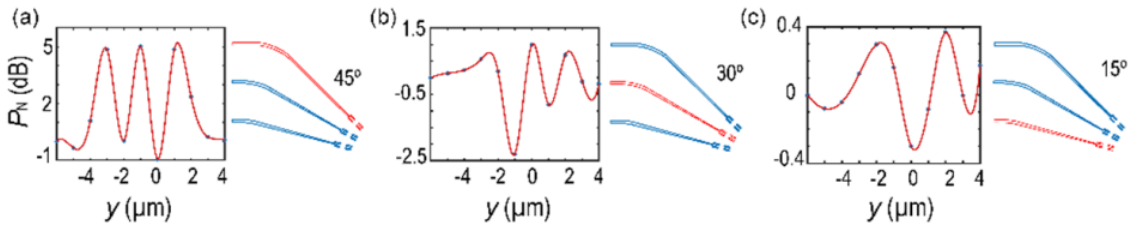

Figure 6. (**a**), (**b**), (**c**) Different pulse shapes were simulated at different angles for 1-μm polystyrene targets, in analogy to the 2-μm microspheres case shown in Fig. 2(b).

device might be a suitable solution in the field of ultra-integrated low-cost flow cytometers, in contrast to current large-footprint on-chip versions or bulky and expensive commercial devices.

Finally, we additionally retrieved the characteristic pulse shape at different angles for 1-µm polystyrene microparticles, proving that, despite being optimized for 2-µm microspheres, the 45º configuration also renders the best performance in terms of SNR for various types of particles, see Fig. 6. The unique scattering signature of a given kind of particle can be used to achieve a highly-selective (ultimately specific, defined as 100% selective) detection, *i.e.*, to detect such kind of particle in mixtures without interferences from other components of similar behavior. Depending on the case, the mentioned signature can be inferred from the information obtained at a single angle, while more angles could be required in matrices with complex populations. Usually, the scattering is sampled at one or two angles, known as the forward scattering and the side scattering (5, 32). In both cases, the present study would allow us to select the angles that maximize the SNR. There exist different algorithms to classify the flowing particles from the retrieved scattering information, such as supervised machine learning (25). Here, the signatures of a set of particles (representative of the populations of interest) whose class is known a priori would be used to train and test the classifier. After this process, the device is able to predict the class of each component in a real sample. Other algorithms employed in classification include principal component analysis and linear discriminant analysis (39).

MATERIALS AND METHODS

The silicon antennas, waveguides and grating couplers were fabricated on standard SOI samples from SOITEC wafers with a top silicon layer thickness of 220 nm (resistivity ρ ~1-10 $\Omega \cdot cm^{-1}$, with a lightly p-type background doping of ~10^{15} cm^3) and a buried oxide layer thickness of 2 µm. The fabrication is based on an electron-beam direct-writing process performed on a coated 100 nm hydrogen silsesquioxane (HSQ) resist film. The mentioned electron-beam exposure, performed with a Raith150 tool, was optimized in order to reach the required dimensions employing an acceleration voltage of 30 KeV and an aperture size of 30 µm. After developing the HSQ resist using tetramethylammonium hydroxide, the resist patterns were transferred into the SOI samples employing an optimized Inductively Coupled Plasma-Reactive Ion Etching process with fluoride gases. Finally, a two-micron-thickness silicon dioxide upper cladding was deposited on the SOI sample by using a Plasma Enhanced Chemical Vapour Deposition system from Applied Materials. Regarding the fabrication of the fluidic channel, a Cr layer of 35 nm was first deposited on the SOI sample by using electron beam metal evaporation. Next step consist of a direct writing electron beam exposure of the channel on a layer of 100 nm of PMMA 950K positive resist. After resist developing, Cr was removed from the channel area using a wet Cr etchant process based on CR-7 ($HClO_4$ + $C(NH_4)_2(NO_3)_6$ + H_2O). Subsequently,

an ICP-process was carried out to dig the channel through the SiO_2. Finally, the sample was cleaned to remove the organic residues by a mixture of H_2SO_4 and H_2O_2 (3:1) during 20 minutes and then washed by deionized water (DIW). This cleaning procedure was also used to regenerate the device after sensing experiments. To prepare the 150-μm thick PDMS substrates (Sylgard 184 Silicone Elastomer Down Corning), the PDMS mixture (10:1) was spin-coated on glass cover slides and cured at 60°C during 1 hour to obtain the aforementioned PDMS layer on the glass slide. In order to clean the surface, after the healing process, the PDMS was peeled off from a glass slide and washed in absolute ethanol. Finally, the PDMS substrate was positioned and aligned atop the fluidic channel granting its sealing.

It is worth mentioning that, while e-beam lithography (employed here to provide a device proof of concept) is not a cost-effective large-scale production approach, other techniques such as nanoimprint lithography can also achieve the resolution required to fabricate the proposed microflow cytometer and are suitable for mass manufacturing (40).

CONCLUSIONS

In this work, we have experimentally demonstrated the realization of an on-chip silicon photonic antenna-based microflow cytometer with a notably improved SNR in the target detection, yielding figures as high as 14 dB. Outstandingly, this design is achieved with a dramatically reduced footprint (0.64×14 μm^2 for a single antenna), when compared with current state-of-the-art approaches (5). This feature becomes especially relevant in the future realization of integrated multi-testing systems (41), allowing a cell/biotarget to flow along several analysis stages on the same chip. As a reference, we can compare some of the most relevant parameters of the device here proposed with the typical specifications of standard commercial devices. For instance, the flow cytometers of the Beckman Coulter FC 500 series (used for benchmarking *e.g.* in (19)) are able to resolve 0.5 μm particles (a value achievable with our device thanks to the aforementioned high directivity of the employed nanoantennas), show a CV between 2% and 4% (the best result for our device is $\approx$ 6%), and offer a maximum acquisition rate of 3300 events/second (potentially reachable by the studied cytometer, see our discussion above). In this respect, our device shows a competitive performance in comparison with commercial cytometers. Moreover, the use of the SOI platform in the fabrication of the antennas readily ensures the mass production of these devices.

Nevertheless, besides improving the microfluidic system to incorporate the aforementioned advanced features, reaching the commercial stage would still entail a series of steps, including chip packaging as well as the development of the required control/processing electronics and of the appropriate application-specific classification algorithms.

The combination of the proposed antenna-based photonic subsystem together with integrated microfluidic set-ups paves the way to the realization of ultra-compact low-cost lab-on-a-chip flow cytometers and POC sensing devices with a direct impact for biological, chemical and medical diagnosis. Additionally, nanoparticle-counting systems (42, 43), which are also related to allergen detection or industrial food processing tests, might be tremendously improved thanks to these cost-effective ultra-integrated devices.

FUNDING

Funding from grant TEC2015-63838-C3-1-R OPTONANOSENS (MINECO/ FEDER, UE) is acknowledged. C.G.-M. acknowledges support from project TEC2015-73581-JIN PHUTURE (AEI/FEDER, UE). This work was also supported by the EU-funded projects FP7-ICT PHOXTROT (No.318240), the EU-funded H2020-FET-HPC EXANEST (No.671553) and the Generalitat Valenciana's PROMETEO grant NANOMET PLUS (PROMETEO II/2014/34)

ACKNOWLEDGMENTS

We thank David Zurita for his help in the design of the data acquisition code for the sensing application.

REFERENCES

1. Redding B, Liew SF, Sarma R *et al*. Compact spectrometer based on a disordered photonic chip. *Nat. Photon.* **7**, 746–751 (2013).
2. Malinauskas M, Žukauskas A, Hasegawa S. Ultrafast laser processing of material: from science to industry. *Light Sci. Appl.* **5**, e16133 (2016).
3. Fan XD, White IM. Optofluidic microsystems for chemical and biological analysis. *Nat. Photon.* **5**, 591–597 (2011).
4. Zheludev NI, Kivshar YS. From metamaterials to metadevices. *Nat. Mater.* **11**, 917–924 (2012).
5. Zhang YS, Watts BR, Guo TY *et al*. Optofluidic device based microflow cytometers for particle/cell detection: a review. *Micromachines* **7**, 70 (2016).
6. Chen X, Li C, Tsang HK. Device engineering for silicon photonics. *NPG Asia Mater.* **3**, 34–40 (2011).
7. Luka G, Ahmadi A, Najjaran H *et al*. Microfluidics Integrated Biosensors: A Leading Technology towards Lab-on-a-Chip and Sensing Applications. *Sensors* **15**, 30011–30031 (2015).
8. Padgett M, Bowman R. Tweezers with a twist. *Nat. Photon.* **5**, 343–348 (2011).
9. Shiau Y. Dielectric Rod Antennas for Millimeter-Wave Integrated Circuits. *IEEE Trans. Microw. Theory Tech.* **24**, 869– 872(1976).
10. Zhou H, Li Z, Shang L *et al*. On-Chip Wireless Optical Broadcast Interconnection Network. *J. Light. Technol.* **28**, 3569–3577 (2010).

11. Brongersma ML. Plasmonics: Engineering optical antennas. *Nat. Photon.* **2**, 270–272 (2008).
12. Alù A, Engheta N. Wireless at the Nanoscale: Optical Interconnects using Matched Nanoantennas. *Phys. Rev. Lett.* **104**, 213902 (2010).
13. Novotny L, van Hulst N. Antennas for light. *Nat. Photon.* **5**, 83–90 (2011).
14. Giannini V, Fernández-Domínguez AI, Heck SC *et al*. Plasmonic Nanoantennas: Fundamentals and Their Use in Controlling the Radiative Properties of Nanoemitters. *Chem. Rev.* **111**, 3888–3912 (2011).
15. Sun J, Timurdogan E, Yaacobi A *et al*. Large-scale nanophotonic phased array. *Nature* **493**, 195–199 (2013).
16. Van Acoleyen K, Rogier H, Baets R. Two-dimensional optical phased array antenna on silicon-on-insulator. *Opt. Express* **18**, 13655–13660 (2010).
17. C. García-Meca, S. Lechago, A. Brimont *et al*. On-chip wireless silicon photonics: from reconfigurable interconnects to lab-on-chip devices. *Light Sci. Appl.* **6**, e17053 (2017).
18. Robinson JP, Roederer M. Flow cytometry strikes gold. *Science* **350**, 739–740 (2015).
19. Mao XL, Nawaz AA, Lin SC *et al*. An integrated, multiparametric flow cytometry chip using 'microfluidic drifting' based three-dimensional hydrodynamic focusing. *Biomicrofluidics* **6**, 024113 (2012).
20. Huang NT, Zhang HI, Chung MT *et al*. Recent advancements in optofluidics-based single-cell analysis: optical on-chip cellular manipulation, treatment, and property detection. *Lab Chip* **14**, 1230–1245 (2014).
21. Psaltis D, Quake SR, Yang C. Developing optofluidic technology through the fusion of microfluidics and optics. *Nature* **442**, 381–386 (2006).
22. Cheung KC, Di Berardino M, Schade-Kampmann G *et al*. Microfluidic Impedance-Based Flow Cytometry. *Cytom. Part A* **77A**, 648–666 (2005).
23. Cheung KC, Gawad S, Renaud P. Impedance Spectroscopy Flow Cytometry: On-Chip Label-Free Cell Differentiation. *Cytom. Part A* **65A**(2), 124–132 (2005).
24. Xie X, Cheng Z, Xu Y *et al*. A sheath-less electric impedance micro-flow cytometry device for rapid label-free cell classification and viability testing. *Anal. Methods* **9**, 1201–1212 (2017).
25. Blasi T, Hennig H, Summers HD *et al*. Label-free cell cycle analysis for high-throughput imaging flow cytometry. *Nat. Comms.* **7**, 10256 (2015).
26. Van Zant P. *Microchip Fabrication: A Practical Guide to Semiconductor Processing* (McGraw Hill Education, 2014).
27. Voelkel R. Wafer-scale micro-optics fabrication. *Adv. Opt. Technol.* **1**, 135–150 (2012).
28. Soref R. The Past, Present, and Future of Silicon Photonics. *IEEE J. Quantum. Electron.* **12**, 1678–1687 (2006).
29. Kononchuk O, Nguyen BY. *Silicon-on-insulator (SOI) technology: Manufacture and applications* (Elsevier, 2014).
30. Baets R, Dumon P, Bogaerts W *et al*. Silicon-on-insulator based nano-photonics: Why, How, What for?. *2nd IEEE International Conference Group IV Photonics* (IEEE, 2005), pp. 168–170.
31. Frankowski M, Theisen J, Kummrow A *et al*. Microflow Cytometers with Integrated Hydrodinamic Focusing. *Sensors* **13**, 4674–4693 (2013).

32. Barat D, Spencer D, Benazzi G *et al*. Simultaneous high speed optical and impedance analysis of single particles with a microfluidic cytometer. *Lab Chip* **12**, 118–126 (2012).
33. Testa G, Persichetti G, Bernini G. Micro flow cytometer with self-aligned 3D hydrodynamic focusing. *Bio. Opt. Express* **6**, 54–62 (2015).
34. Etcheverry S, Faridi A, Ramachandraiah H *et al*. High performance micro-flow cytometer based on optical fibres. *Sci. Rep.* **7**, 5628 (2017).
35. Balanis CA, *Antenna Theory: Analysis and Design* (Wiley, 1982).
36. Kosako T, Kadoya Y, Hofmann HF. Directional control of light by a nano-optical Yagi-Uda antenna. *Nat. Photon.* **4**, 312–315 (2010).
37. Kotz KT, Petrofsky AC, Haghgooie R *et al*. Inertial focusing cytometer with integrated optics for particle characterization. *Technology* (Singap. World Sci.) **1**, 27–36 (2013).
38. Taillaert D, Van Laere F, Ayre M *et al*. Grating Couplers for Coupling between Optical Fibers and Nanophotonic Waveguides. *Jpn. J. Appl. Phys.* **45**, 6071–6077 (2006).
39. Potcoava MC, Futia GL, Aughenbaugh J *et al*. Raman and coherent anti-Stokes Raman scattering microscopy studies of changes in lipid content and composition in hormone-treated breast and prostate cancer cells. *J. Biomed. Opt.* **19**, 111605 (2014).
40. Traub MC, Longsine W, Truskett VN. Advances in Nanoimprint Lithography. *Annu. Rev. Chem. Biomol. Eng.* **7**, 583–604 (2016).
41. Xu BB, Zhang YL, Xia H *et al*. Fabrication and multifunction integration of microfluidic chips by femtosecond laser direct writing. *Lab Chip* **13**, 1677–1690 (2013).
42. Zucker RM, Ortenzio JNR, Boyes WK. Characterization, Detection, and counting of Metal Nanoparticles Using Flow Cytometry. *Cytometry A* **89**, 169–183 (2016).
43. Kowalczyk B, Lagzi I, Grzybowski BA. Nanoseparation: Strategies for size and/or shape-selective purification of nanoparticles. *Curr. Opin. Colloid. Interface Sci.* **16**, 135–148 (2011).

PAPER C. ALL-SILICON ON-CHIP OPTICAL NANOANTENNAS AS EFFICIENT INTERFACES FOR PLASMONIC DEVICES

All-Silicon On-chip Optical Nanoantennas As Efficient Interfaces for Plasmonic Devices

Sergio Lechago, Carlos García-Meca, Amadeu Griol,
Miroslavna Kovylina, Laurent Bellieres and Javier Martí

Nanophotonics Technology Center, Universitat Politècnica de València, 46022 Valencia, Spain.
Correspondence: S. Lechago, Email: serlecbu@ntc.upv.es

ABSTRACT

Plasmonic technology promises to unfold new advanced on-chip functionalities with direct applications in photovoltaics, light matter interaction and the miniaturization of optical interconnects at the nanoscale. In this scenario, it is crucial to efficiently drive light to/from plasmonic devices. However, typically-used plasmonic wires introduce prohibitive losses, hampering their use for many applications. Recently, plasmonic nanoantennas have been proposed to overcome this drawback, not only providing a notable loss reduction, but also an enhanced on-chip flexibility and reconfigurability. Nevertheless, these devices still perform poorly for long-reach interconnects, owing to their low-directive radiation and low efficiency. Here, we introduce a class of slot-waveguide-based silicon nanoantennas that lift all these limitations, and show their feasibility to be connected directly and efficiently to plasmonic devices. To test the performance of these antennae, an on-chip plasmonic-dielectric interconnect is experimentally demonstrated over distances as high as 100 μm. In an outstanding manner, our wireless scheme clearly outperforms previous plasmonic approaches in terms of link efficiency and effective gain. This work paves the way to the development of ultra-fast on-chip wireless reconfigurable and flexible interconnects, and additionally opens new avenues in optical manipulation and sensing applications.

INTRODUCTION

Plasmonic devices have enabled the development of important applications in fields such as spectroscopy, near-field optical microscopy or biosensing (1) thanks to their unique ability to engineer light at the nanoscale. Within integrated on-chip communications, plasmonic approaches offer the potential for the realization of ultra-compact low-cost devices (modulators, detectors or nanoscale chip sources (1)) able to perform at very high operation speeds with a low power consumption (2). The natural way for interconnecting these devices on the optical chip is the use of metallic nanowires. Nevertheless, guiding light over long distances via plasmonic waveguides results in prohibitive propagation losses (3), (4). An alternative to mitigate this loss relies on the use of dielectric couplers (5), able to interface plasmonic devices with typical silicon waveguides. In contrast, these dielectric-metallic wired schemes still provide stringent limitations in terms of flexibility and reconfigurability at the photonic layer (6). Recently, the emergence of

plasmonic nanoantennas (7), (8), (9), (10) has also demonstrated their suitability to reduce propagation losses as compared to metallic nanowires (3). This allows, for instance, the implementation of unguided interconnects with interferenceless crossing paths on the same layer (thus avoiding multilayer geometries (9)), compact reconfigurable devices and more flexible on-chip networks (6), (10), (11). These features lessen the presence of waveguides, leading to simpler on-chip layouts (6), (11). Additionally, the interaction with the medium at far-field distances enabled by antennas, paves the way to less complex networks for communications (11) and new functionalities for sensing applications (6), (12), (13) and microparticle control (6), hardly achievable with wired-based approaches. However, while improving the performance of their wired counterparts, plasmonic nanoantennas yield low directivity values and high losses (10), (14) because of their strong field confinement and the metallic absorption in the optical regime (15), hindering their application for practical on-chip wireless links. On the other hand, nanoantennas based on dielectric nanoparticles (16), (17) have emerged, presenting better radiation efficiencies due to their low-loss nature and higher directivity than metallic structures, not always compromising the usual higher compactness of plasmonic approaches. Nevertheless, the complexity in the fabrication of these nanoparticles has prevented their practical implementation for wireless interconnects. Other approaches with enhanced directivities relies on the use of non-compact systems as dielectric arrays (18), (19), more suitable for off-plane interconnects. More recently, it was demonstrated that most of the aforesaid disadvantages can be overcome by using strip-waveguide-based silicon nanoantennas, which have enabled the realization of long-reach dynamically-reconfigurable on-chip wireless interconnects, as well as of different lab-on-a-chip sensors (6), (13). It is then natural to ask whether these kind of dielectric antenna might interface plasmonic systems to boost a new variety of high-performance applications. However, although strip dielectric waveguides can be theoretically connected to slot plasmonic waveguides with a very high efficiency, this requires quite complex transitions between the plasmonic and dielectric structures, leading to a difficult error-sensitive implementation and large footprints, with a notable reduction of the experimental efficiency with respect to theoretical estimations (20).

In this letter, we explore a different wireless system built upon slot-waveguide-based silicon optical antennas able to be efficiently and directly connected to plasmonic slot wires. The simplicity of this dielectric-to-plasmonic transition allows us to obtain experimental coupling efficiencies surpassing those obtained with sophisticated strip-to-slot couplers. Through this hybrid design, we are able to combine the advantages provided by both dielectric and plasmonic technology to produce high-performance on-chip devices, boosting the development of new applications at the nanoscale.

RESULTS AND DISCUSSION

As a starting point, we consider the system shown in Figure 1a. On the left, a semi-infinite plasmonic slot waveguide (PSW) is connected to a finite dielectric slot waveguide (DSW). With the suitable dimensions, the open end of the DSW behaves as an efficient aperture antenna (6), while the PSW acts as a bridge to

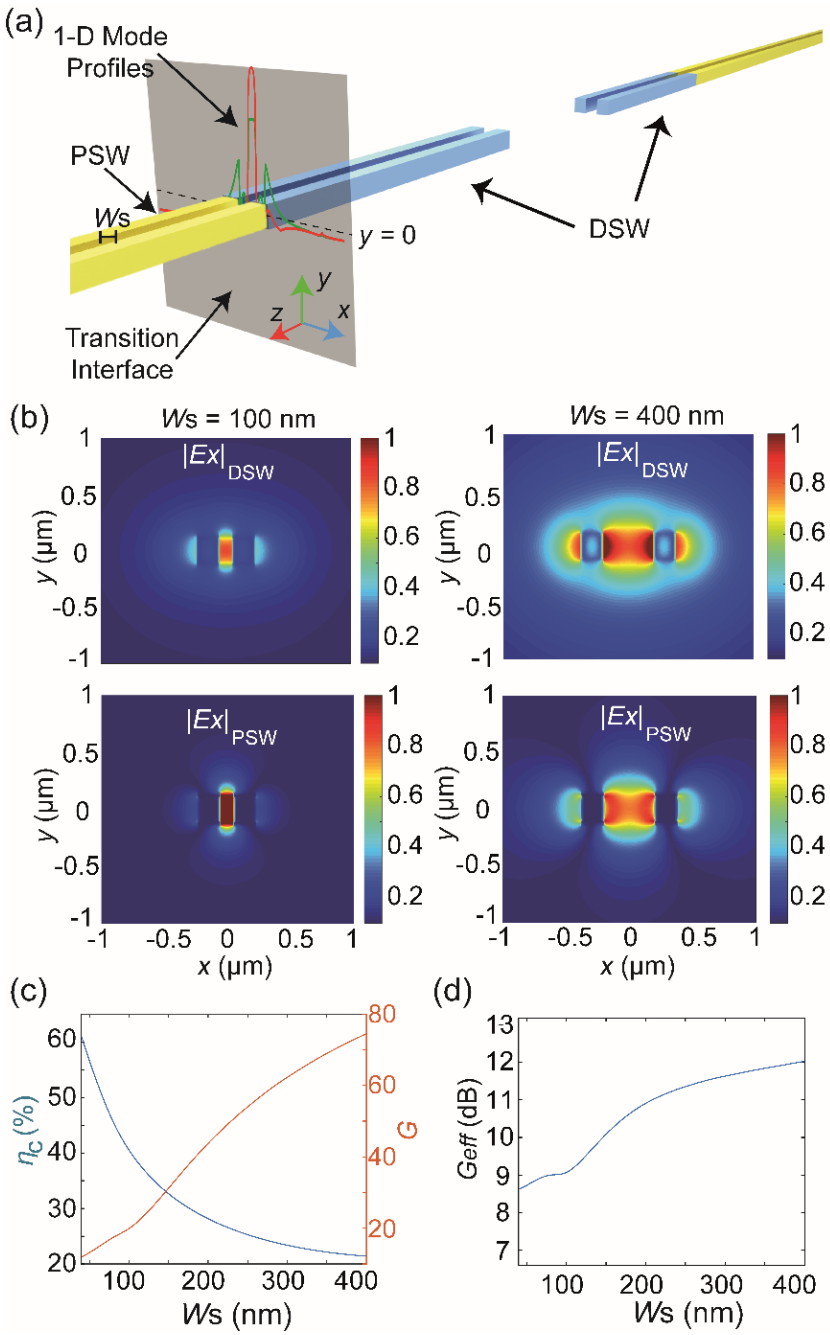

Figure 1. (**a**) Artwork depicting the coupling between plasmonic and dielectric waveguides. The corresponding mode profiles at $y = 0$ are displayed on the transition interface (shaded region). (**b**) E-field intensity distributions of the TE modes excited at the dielectric (top) and plasmonic (bottom) waveguides for $w_S = 100$ nm and $w_S = 400$ nm. Calculations were carried out at the telecom wavelength $\lambda = 1550$ nm. (**c**) Coupling efficiency (blue) and DSW-based antenna gain (red) as a function of w_S. The dielectric and metallic waveguides were assumed to be made of Si and Au, respectively. A Drude model was employed for Au (21). (**d**) Effective gain of the DSW-based antenna.

connect this antenna with a plasmonic device. Therefore, a plasmonic mode guided by the PSW is converted to a guided mode in the subsequent DSW and radiated at its open end. An equal DSW-PSW hybrid device receives the radiated wave on the right and transforms it back to a plasmonic mode. It is worth mentioning that the plasmonic interconnect is not necessarily a long section of plasmonic wire, since a short waveguide section (with very low losses) would readily connect the wireless antennas with the

plasmonic system for communications, sensing or other purposes. Our goal is to maximize the total power efficiency η of the system, which is basically given by the product $\eta = (\eta_C GR)^2$ for the proposed configuration. Here, η_C is the PSW-to-DSW coupling efficiency, G is the gain of the DSW aperture antenna (including directivity, radiation efficiency and reflection coefficient) and $R = \lambda/(4\pi d)$ accounts for the free-space propagation loss associated with a link distance d. The product $G_{eff} = \eta_C G$ can be considered as the effective gain of the DSW-based antenna. Since R is fixed, we need to find the optimal system geometrical parameters providing the combination of η_C and G that maximizes η. Driven by technological feasibility, we constrained the height of all structures to 220 nm, assuring their compatibility with standard silicon-on-insulator (SOI) wafers. Furthermore, note that for a given slot width w_S, the width of the arms of the DSW and the PSW has a small influence on the profile of the corresponding TE modes, since the field is mainly concentrated on the waveguide slots. Consequently, w_S becomes the key design parameter to be engineered. We started by studying the influence of w_S on η_C, which was numerically calculated using the commercial software CST Microwave Studio. As can be seen in Figure 1b, the fundamental TE modes of both structures are quite similar for low values of w_S. However, they become progressively different as w_S increases; the DSW mode becomes rapidly unconfined as w_S increases, whilst the PSW gap plasmon remains concentrated in the slot up to larger values. Consequently, the best figures of η_C are retrieved for low values of w_S as shown in Figure 1c, in consonance with the mode likeness at both structures. The next step was to analyze the influence of w_S on G. We used Huygens' principle to model this structure as an aperture antenna, following the method typically employed in classic microwave and radiofrequency theory (22). This approach directly links the DSW radiation pattern with the Fourier transform of its mode transverse electric and magnetic fields. A straightforward implication is that less confined modes lead to higher directivities, since the angular extension of the radiation vectors decreases as the spatial extension of the mode increases (6). Figure 1b shows that the DSW fundamental TE mode is less confined as w_S increases, explaining why G grows as a function of this parameter, reaching very high values not achievable with previous plasmonic nanoantennas, see Figure 1c. It is noteworthy that the directivity of the DSW-based antenna can be easily tuned just by adjusting w_S. Moreover, the propagation constant (*e.g.*, $\beta = 6.35362 \cdot 10^6$ m^{-1} for $w_S = 180$ nm, which provides an effective refractive index $n_{eff} = 1.567$) associated with these less confined modes is close to that of the surrounding medium (SiO_2 with refractive index $n = 1.45$), favoring impedance matching and avoiding undesired reflections. Figure 1d depicts G_{eff} as a function of w_S, showing that there is a large region ($w_S > 160$ nm) for which G_{eff} is higher than 10 dB, slowly increasing with w_S. This feature provides us with an ample design flexibility. That is, w_S can be adjusted to suit applications requiring lower reflections (*e.g.* to improve source protection) or higher directivities (*e.g.*, to minimize radiation interference with adjacent devices), while keeping a similar performance in terms of overall power efficiency without any coupling structure. Limiting ourselves to typical w_S values (20-200 nm (20), (23)), we decided to work with $w_S = 180$ nm, which already shows a gain $G \approx 40$. Furthermore, we could combine the advantages associated with a small w_S value (enhanced η_C) and a high w_S value

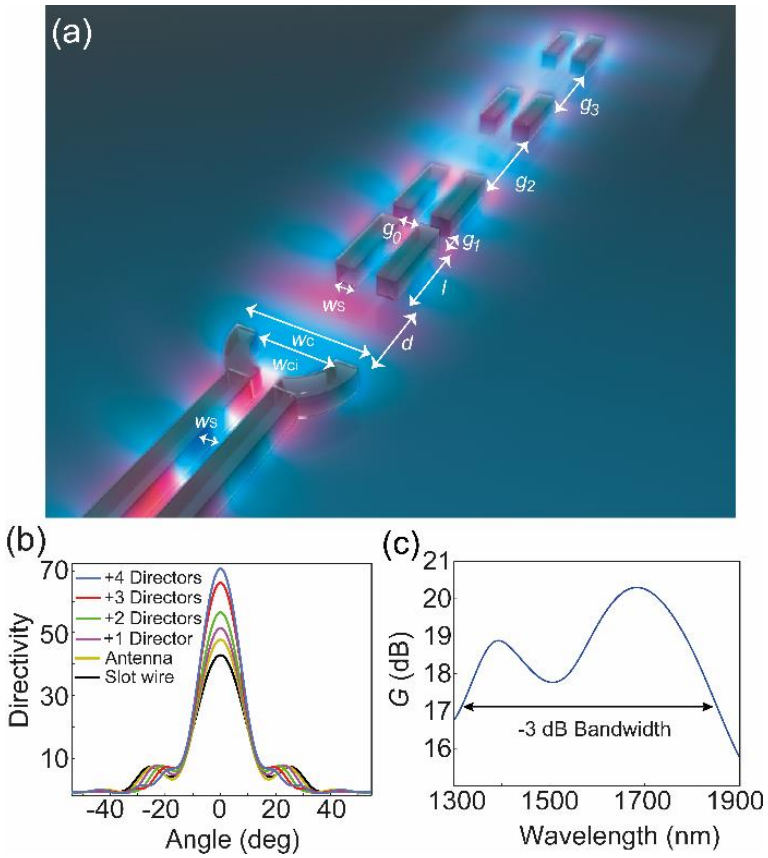

Figure 2. (**a**) Schematic picture of the nanoantenna and the directors with their corresponding dimensions where w_S = 180 nm, w_{Ci} = 640 nm, w_C = 1000 nm, d = 500 nm, l = 800 nm, g_0 = 340 nm, g_1 = 200 nm, and g_2 = g_3 =1000 nm. CST Microwave Studio was employed to perform the optimization and all the numerical calculations of this work. (**b**) Simulated directivity of the designed slot waveguide with and without C antenna and directors. (**c**) Simulated gain of the C antenna. The -3 dB Bandwidth is highlighted, demonstrating the broadband behavior of this design.

(enhanced G) just by using a simple and compact silicon PSW-DSW transition (see supporting information, section 1), which already yields η_C = 0.47 and $G \approx 40$ in a footprint of approximately 1 μm^2. Note that higher coupling efficiencies could be attained by further optimizing the plasmonic-to-dielectric waveguide transition. For example, a longer taper would approach the 62% efficiency value for w_S = 40 nm. However, although such transitions play an important role in the system, its optimization is out of the scope of this work, which focuses on showing that dielectric antennas can act as high-performance wireless interfaces for plasmonic devices (outperforming previous all-plasmonic approaches), while keeping the design as simple as possible. Additionally, the directivity can also be further enhanced by modifying the DSW radiating end and by adding some specific extra dielectric elements. In particular, we explored different modifications inspired by V-antenna designs (24), see supporting information, section 2. The best improvement was achieved with a smoothed (C-shaped) version of this kind of structure, see Figure 2a, with a directivity improvement of the order of an 11%, see Figure 2b. Moreover, we studied the influence of adding further elements (directors) to the C-antenna design. By analogy with typical metallic Yagi-Uda configurations (25), (26), (27) in which the directors are basically passive antennas of the same type as the principal one (usually dipoles), we considered directors consisting of couples of silicon strips, similar to DSW pieces, see Figure 2a. The number of directors as well as their location and dimensions were

optimized through numerical simulations to maximize the directivity in an on-chip footprint as constrained as possible, see supporting information, section 3. The impact of the C-antenna and a varying number of directors on the directivity is shown in Figure 2b. Our final configuration includes four directors, since additional elements provide small improvements while considerably increasing size, see Figure 2b. In this case, a full single antenna (C nanostructure with four directors) achieves a directivity of 71 [previous dielectric nanoparticle antennas reach values up to 12 (16), (17)] and a gain $G = 65$ at $\lambda = 1550$ nm [$G > 100$ (linear units) is achieved at longer wavelengths, see Figure 2c]. The corresponding effective gain of this device is $G_{eff} = 0.30 \cdot 65 = 19.5$ ($G_{eff} = 0.47 \cdot 65 = 30.5$ when using the aforementioned coupler).

Although devices operating at different wavelengths cannot be directly compared (the optical properties of metals are frequency-dependent), we take the work in (11) as a reference (which was designed for a wavelength of 650 nm), since, to date (and for the best of our knowledge), it provides the highest efficiency for a plasmonic link in any spectral band, setting the bar for current research in this area. Particularly, the plasmonic nanoantenna designed therein yields a gain of 6.8. Hence, the proposed optical antenna in the present work provides a notable improvement with respect to this previous design. Nonetheless, it is worth mentioning that this improvement comes at the cost of a considerably higher footprint than that of typical plasmonic antennas. Along this line, to compare the overall goodness of different optical antennas, we have defined a figure of merit that takes into account both gain and footprint (see supporting information section 4), according to which, in spite of their larger footprint, the proposed DSW-based antennas clearly outperform previous designs. In addition, we have compared the power efficiency of a plasmonic wired link with that of a wireless one based on the proposed antennas (see supporting information section 5), showing that the wireless scheme exhibits a higher efficiency than the waveguide-based interconnect for distances exceeding 55 μm (as an example, the improvements achieved at 100 μm and 200 μm are higher than 15 and 55 dB, respectively). Moreover, the proposed device possesses a working bandwidth of approximately 600 nm, see Figure 2c, since DSW-based antennas do not rely on resonant phenomena. On the contrary, they display almost perfect impedance matching with the cladding in a wide spectral region (the reflection coefficient of the DSW-based antenna is below 0.03). Thus, unlike in typical plasmonic schemes, auxiliary resonant matching elements (28) are not necessary, avoiding the bandwidth limitation they introduce.

To provide a proof of concept of the proposed approach, we fabricated and characterized different devices using Au as the constituent material for the plasmonic wires. In the experiments, we inject/collect light to/from the chips via standard silicon grating couplers and waveguides. Therefore, we have a second dielectric-plasmonic transition at each link end (between the exciting/collecting Si waveguide and the corresponding plasmonic waveguide, see Figure 3) as compared to the structures shown in Figure 1, in which a single dielectric-plasmonic transition per link end is assumed (this could actually be the case in a practical application). With this

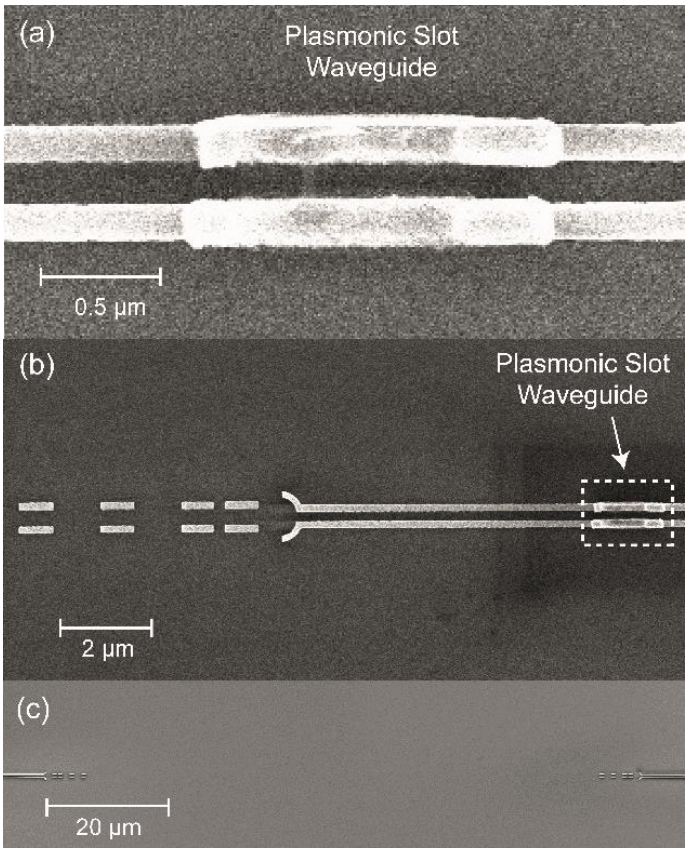

Figure 3. (**a**) Scanning electron microscope (SEM) image of the fabricated gold slot waveguide section in between the silicon wires. (**b**) SEM image of the DSW-based antenna connected to a 1-μm length plasmonic slot waveguide. (**c**) SEM image of a 100-μm-long link consisting of two antennas as the one shown in (b). All the samples were covered with a 2-μm-thick layer of SiO_2.

consideration in mind, and following the work in (20), we first fabricated a sample in which a plasmonic slot waveguide section was inserted in between two dielectric slot waveguides (see Figure 3a and Methods), in order to experimentally obtain the value of the PSW-to-DSW coupling efficiency η_C (this configuration includes no wireless link). Note that light goes through two PSW-to-DSW facets in this structure. Consequently, Fabry-Pérot resonances arising from the presence of the cavity formed by the plasmonic waveguide in between the silicon wires may alter the power transmission efficiency of the system (with respect to a single Si-Au transition), depending on λ and the cavity length d_C. Specifically, with the employed scheme (d_C = 1 μm), the Si-Au-Si transition power efficiency is $\eta_{FP} \approx 0.45$ at λ = 1550 nm (or, equivalently, it possesses an insertion loss, IL, of 3.43 dB), which is higher than the previously calculated $\eta_C = 0.3$ for a single Au-Si transition (as confirmed by the simulations, compare Figures 1c and 4a). The numerically-calculated efficiency η_{FP} of this Si-Au-Si transition (IL = 3.24 dB) is in very good agreement with the measurements (see Figure 4a). For fixed values of d_C and λ, η_{FP} is only a function of η_C (and of the theoretically known plasmonic waveguide complex wavenumber). Therefore, the good agreement between the numerically and experimentally obtained IL values for this device at λ = 1550 nm (Figure 4a), implies that $\eta_C \approx 0.3$ is also the coupling efficiency of each single Au-Si

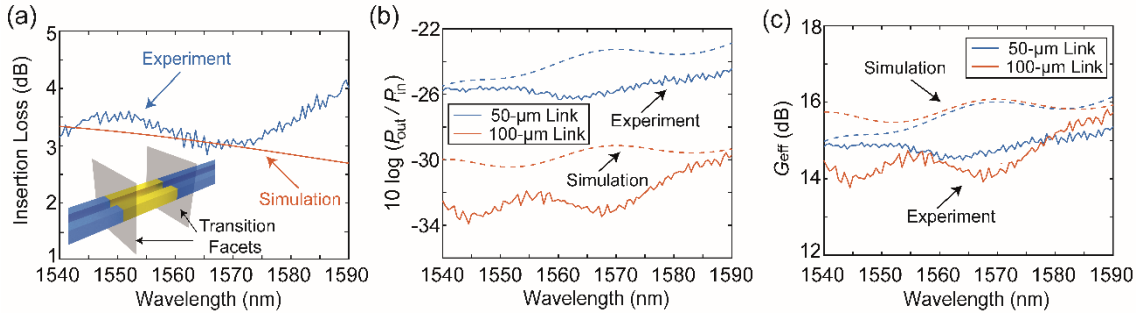

Figure 4. (**a**) Simulated (red) and experimental (blue) normalized insertion loss of a 1-µm length gold slot waveguide. Shaded areas represent the transition facets of the plasmonic wire with the silicon waveguides from which light is injected (collected) via grating couplers, see supporting information, section 7. At a wavelength of λ = 1550, the experimental IL = 3.43 dB. (**b**) Comparison of the experimental (solid lines) versus simulated (dashed lines) normalized link power efficiency corresponding to the links with d = 50 µm and d = 100 µm. (**c**) Comparison of the simulated and measured nanoantenna gain. In the worst case, G_{eff} = 14.14 dB at λ = 1550 nm. The effective gain was retrieved from the measured power efficiency, which in our experiment is $\eta = G_{eff}^2 \cdot \eta_G^2 \cdot \eta_{PROP}^2$, where η_G stands for the experimental grating coupler insertion loss, and $\eta_{PROP} = \lambda \cdot (4\pi d)^{-1}$, represents the propagation loss in the link (see supporting information, section 7 for the values of η_G).

transition in the fabricated Si-Au-Si structure (note that we do not directly measure this parameter). The experimental and theoretical values of IL as a function of wavelength for this structure are shown in Figure 4a (the E-field distribution of the Si-Au-Si scheme is available in the supporting information, section 6). Notably, the measured insertion loss for a very similar Si-Au-Si scheme based on dielectric strip waveguide to plasmonic slot waveguide transitions (also with a 1-µm-long plasmonic slot waveguide) was IL ≈ 14 dB (20), with a dielectric-to-plasmonic footprint of approximately 8 µm^2 (the coupler footprint is virtually zero in our case). Next, we fabricated two different samples including full wireless links consisting of two DSW-based antennas, each connected to a 1-µm-long plasmonic slot waveguide section, with distances d of 50 and 100 µm (see Figures 3b, 3c and Methods). For the sake of simplicity, we focused our experimental efforts on the direct butt-coupling between a plasmonic and a dielectric slot wire with w_S = 180 nm, see Figure 3b (*i.e.*, we do not include the theoretically-analyzed taper shown in the supporting information, section 1). To test the wireless interconnects, we measured the link efficiency for both distances (50 and 100 µm), attaining a very good agreement with the simulations (see Figure 4b), although small discrepancies arise from waveguide shape imperfections inherent to the fabrication process. A similar behavior to that predicted by the Friis transmission equation (22) can be observed in Figure 4b between the 50- and 100-µm links, which results in an increase of approximately 6 dB in the overall link loss as doubling distances between antennas. In addition, we retrieved the antenna gain from the experimental measurements, finding again a good agreement with the numerical results (see Figure 4c). Remarkably, the link is able to radiate with a similar performance within the whole measured optical bandwidth, spanning 50 nm. It must be pointed out that both the experimentally- and numerically-retrieved values of G_{eff} depicted in Figure 4 for the links including the 1-um-long plasmonic waveguide are slightly higher than the numerically calculated value for a link with single Au-Si transitions, due to the fact that the IL of the Si-Au-Si transition is lower than that of a single Au-Si transition, as mentioned above. Finally, to further test the proposed DSW-based antennas, we

carried out an additional experiment in which data streams of 40 Gbit·s^{-1} were transmitted over 20-µm-length links (see supporting information, section 8).

CONCLUSION

We have demonstrated a long-reach wireless plasmonic-dielectric optical interconnect based on silicon nanoantennas able to be directly and efficiently connected to plasmonic systems. Specifically, the numerical study of the modes supported by plasmonic and dielectric slot waveguides with equal slot widths revealed that an efficient direct butt-coupling between these structures is possible. The proper combination of this feature with the development of a new kind of DSW-based nanoantenna proves the utility of these dielectric structures as efficient interfaces for plasmonic devices. In order to test the performance of the proposed nanoantennas, we experimentally demonstrated power transmissions at link distances as long as 100 µm. Despite the fact that the DSW-based antennas here demonstrated exhibit less compact footprints than most of the previous metallic schemes, our hybrid design widely outperforms its plasmonic counterparts in terms of directivity, efficiency and planar reach. Moreover, such a combination merges the ability of silicon nanoantennas to achieve long-reach wireless communications, reconfigurable interconnects, beam-shaping elements, and lab-on-a-chip devices (6), with the advantages of plasmonic structures for ultra-fast data conversion and light concentration and manipulation. Finally, this hybrid configuration might enable the implementation of new sensing applications and microwave plasmonic devices in the THz band (6), (29).

METHODS

The fabrication of the dielectric links was based on the use of standard SOI samples from SOITEC wafers with a top silicon layer thickness of 220 nm (resistivity ρ ~1-10 $\Omega \cdot cm^{-1}$, with a lightly p-type background doping of ~10^{15} cm^{-3}). The fabrication is based on an electron beam direct writing process performed on a coated 100 nm hydrogen silsesquioxane (HSQ) resist film. The mentioned electron beam exposure, performed with a Raith150 tool, was optimized in order to reach the required dimensions employing an acceleration voltage of 30 KeV and an aperture size of 30 µm. After developing the HSQ resist using TetraMethylAmmoniumHyrdoxide (TMAH) as developer, the resist patterns were transferred into the SOI samples employing an optimized Inductively Coupled Plasma- Reactive Ion Etching (ICP-RIE) process with fluoride gases (SF_6 and CF_4). Once the dielectric waveguides and antennas were fabricated, the plasmonic structures were placed inside the silicon waveguides gaps by means of a second e-beam lithography process. This new lithography was performed again with the Raith150 tool (10 KeV, aperture 30 µm) prior to a new metal evaporation (220 nm of gold + 5 nm of titanium for adhesion enhancement) performed with a Pfeiffer Classic 500 tool. Finally, a soft lift-off process (leaving the sample in acetone for

8 hours) was used to define the plasmonic waveguides. To ensure the right positioning of the plasmonic structures, different alignment marks were created in the previous silicon etching level, guiding us in an iterative exposure process to achieve the best alignment. The plasmonic structures placement during final exposure was adjusted according to this iterative process in order to compensate e-beam drifts. Finally, a SiO_2 upper cladding (2-µm thickness) was deposited atop the SOI sample by Plasma Enhanced Chemical Vapor Deposition (PECVD) performed with a Centura 5200 tool from Applied Materials.

ASSOCIATED CONTENT

Supporting Information

Section 1. Silicon coupler for enhanced coupling efficiency. Section 2. Modelling of the C-Shaped antenna. Section 3. Design of antenna directors. Section 4. Power efficiency of wireless versus plasmonic links. Section 5. Figure of merit of the wireless interconnect. Section 6. E-field distribution in the Si-Au-Si transition. Section 7. Experimental grating coupling efficiency. Section 8. Data transmission experimental test.

ACKNOWLEDGEMENT

This work was supported by project TEC2015-73581-JIN PHUTURE (AEI/FEDER, UE) and Generalitat Valenciana's PROMETEO grant NANOMET PLUS (PROMETEO II/2014/34).

CONFLICT OF INTEREST

The authors declare no competing financial interest.

REFERENCES

1. Brongersma ML, Shalaev VM. The Case for Plasmonics. *Science* **328**, 440−441 (2010).
2. Haffner C, Heni W, Fedoryshyn Y *et al*. All-plasmonic Mach–Zehnder modulator enabling optical high-speed communication at the microscale. *Nat. Photon.* **9**, 525−528 (2015).
3. Alù A, Engheta N. Wireless at the Nanoscale: Optical Interconnects using Matched Nanoantennas. *Phys. Rev. Lett.* **104**, 213902 (2010).
4. Khurgin JB. How to deal with the loss in plasmonics and metamaterials. *Nat. Nanotech.* **10**, 2–6 (2015).
5. Briggs RM, Grandidier J, Burgos SP *et al*. Efficient Coupling between Dielectric-Loaded Plasmonic and Silicon Photonic Waveguides. *Nano Lett.* **10**, 4851−4857 (2010).
6. García-Meca C, Lechago S, Brimont A *et al*. On-chip wireless silicon photonics: from reconfigurable interconnects to lab-on-chip devices. *Light Sci. Appl.* **6**, e17053 (2017).

7. Novotny L, van Hulst N. Antennas for light. *Nat. Photon.* **5**, 83−90 (2011).
8. Bharadwaj P, Deutsch B, Novotny L. Optical Antennas. *Adv. Opt. Photon.* **1**, 438−483 (2009).
9. Ni X, Emani NK, Kildishev AV *et al*. Broadband Light Bending with Plasmonic Nanoantennas. *Science* **335**, 427 (2012).
10. Dregely D, Lindfors K, Lippitz M *et al*. Imaging and steering an optical wireless nanoantenna link. *Nat. Commun.* **5**, 4354 (2014).
11. Yang Y, Li Q, Qiu M. Broadband nanophotonic wireless links and networks using on-chip integrated plasmonic antennas. *Sci. Rep*. **6**, 19490 (2016).
12. Zhang YS, Watts BR, Guo TY *et al*. Optofluidic Device Based Microflow Cytometers for Particle/Cell Detection: A Review. *Micromachines* **7**, 70 (2016).
13. Lechago S, García-Meca C, Sánchez-Losilla N *et al*. High signal-to-noise ratio ultra-compact lab-on-a-chip microflow cytometer enabled by silicon optical antennas. *Opt. Express* **26**, 25645−25656 (2018).
14. Solís DM, Taboada JM, Obelleiro F *et al*. Optimization of an optical wireless nanolink using directive nanoantennas. *Opt. Express* **21**, 2369−2377 (2013).
15. Zhao Y, Engheta N, Alù A. Effects of shape and loading of optical nanoantennas on their sensitivity and radiation properties. *J. Opt. Soc. Am. B* **28**, 1266 (2011).
16. Filonov DS, Krasnok AE, Slobozhanyuk AP *et al*. Experimental verification of the concept of all-dielectric nanoantennas. *Appl. Phys. Lett.* **100**, 201113 (2012).
17. Krasnok AE, Miroshnichenko AE, Belov PA *et al*. All-dielectric optical nanoantennas. *Opt. Express* **20**, 20599−20604 (2012).
18. Van Acoleyen K, Rogier H, Baets R. Two-dimensional optical phased array antenna on silicon-on-insulator. *Opt. Express* **18**, 13655−13660 (2010).
19. Sun J, Timurdogan E, Yaacobi A *et al*. Large-scale nanophotonic phased array. *Nature* **493**, 195−199 (2013).
20. Tian J, Yu S, Yan W *et al*. Broadband high-efficiency surface-plasmon-polariton coupler with silicon-metal interface. *Appl. Phys. Lett.* **95**, 013504 (2009).
21. Johnson PB, Christy RW. Optical Constants of the Noble Metals. *Phys. Rev. B* **6**, 4370 (1972).
22. Balanis C. *Antenna Theory: Analysis and Design.* John Wiley & Sons, New Jersey, pp 94–96 (2005).
23. Veronis G, Fan S. Modes of Subwavelength Plasmonic Slot Waveguides. *J. Light. Technol.* **25**, 2511−2521 (2007).
24. Klemm M. Novel Directional Nanoantennas for Single-Emitter Sources and Wireless Nano-Links. *Int. J. Opt.* **2012**, 348306 (2012).
25. Curto AG, Volpe G, Taminiau TH *et al*. Unidirectional Emission of a Quantum Dot Coupled to a Nanoantenna. *Science* **329**, 930−933 (2010).
26. Dregely D, Taubert R, Dorfmüller J *et al*. 3D optical Yagi–Uda nanoantenna array. *Nat. Commun.* **2**, 267 (2011).
27. Coenen T, Vesseur EJR, Polman A *et al*. Directional Emission from Plasmonic Yagi–Uda Antennas Probed by Angle-Resolved Cathodoluminescence Spectroscopy. *Nano Lett.* **11**, 3779−3784 (2011).
28. Alù A, Engheta N. Input Impedance, Nanocircuit Loading, and Radiation Tuning of Optical Nanoantennas. *Phys. Rev. Lett.* **101**, 043901 (2008).
29. Burla M, Bonjour R, Salamin Y *et al*. 2016 IEEE International Topical Meeting on Microwave Photonics (MWP), **259** (2016).

Supporting Information

All-Silicon On-chip Optical Nanoantennas As Efficient Interfaces for Plasmonic Devices

Sergio Lechago *, Carlos García-Meca, Amadeu Griol, Miroslavna Kovylina, Laurent Bellieres and Javier Martí

Nanophotonics Technology Center, Universitat Politècnica de València, 46022 Valencia, Spain.
Correspondence: S. Lechago, Email: serlecbu@ntc.upv.es

1. Silicon coupler for enhanced coupling efficiency

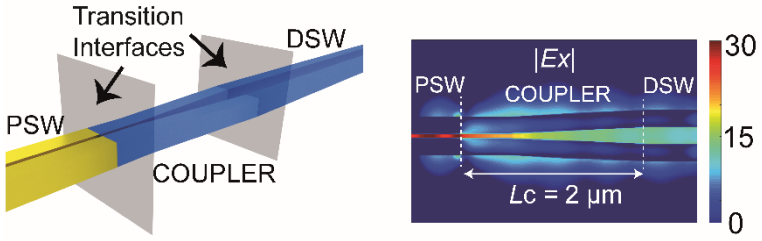

Figure S1. On the left, a 3D artwork representing the silicon coupler and the transition facets on both the PSW (w_S = 40 nm) and DSW (w_S = 180 nm). On the right, the top view of the E-field intensity distribution (dB) in the coupler with a length L_C = 2 µm. This configuration was just theoretically studied.

2. Modelling of the C-Shaped antenna

We studied the impact that simple modifications at the output facet of a slot waveguide could provide on the final directivity of the antenna. Inspired by previous V-antenna designs, we started by bending the arms of the slot wire in several angular directions (θ) and retrieving the corresponding directivity. As a point of departure, we established an arm length (l_{ARM}) of 0.5 µm. Clearly, large angles yield a poorer directivity, see Figure S2. The best directivity value is achieved for an arm bending angle of 20º, which, on the other hand, slightly increases the final footprint of a bare slot antenna. Using this last design as a basis, we heuristically smoothed this V-configuration towards a C-shaped scheme, keeping the V-antenna arm width and setting the outer radius (R) to the same value as l_{ARM} (0.5 µm), in order to obtain a more gradual transition, feature which also has a reduced impact on the footprint, see shaded inset in Figure S2. With this simple modification, we obtained a directivity enhancement of 9.7%, from 44.12 to 48.39. Additionally, we studied the influence of increasing the value of R on the directivity, achieving very low improvements at a cost of having much larger footprints. Thus, to enhance the directivity

to higher figures, we decided to keep this C-shaped design and analyze the impact of adding directors to this configuration, as explained in next section.

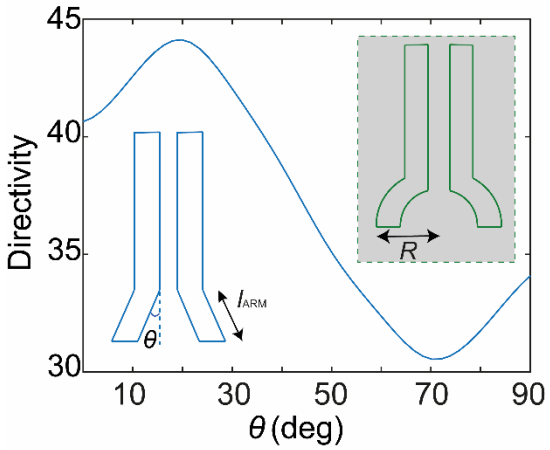

Figure S2. Directivity dependence on the bending angle θ. The maximum directivity values are achieved for $\theta \sim 20^{o}$. Shaded region in the graph depicts the final C-shaped antenna design.

3. Design of antenna directors

Based on the approach shown in the supplementary material of Ref. 6 in the manuscript, we studied the influence of placing different silicon slot planar pieces in front of the C-Antenna, mimicking the behavior of the well-known directors from classical antenna theory. Firstly, we studied the impact of the director length in terms of directivity in a configuration 'antenna + director'. For $l_{DMAX} \approx 7$ µm, as depicted in Figure S3, the system reaches its maximum directivity value (~60), setting up an important design rule to establish the maximum director length. Trying to achieve a footprint as constrained as possible, we restricted ourselves to this maximum length and split the slot director into several pieces to enhance this directivity.

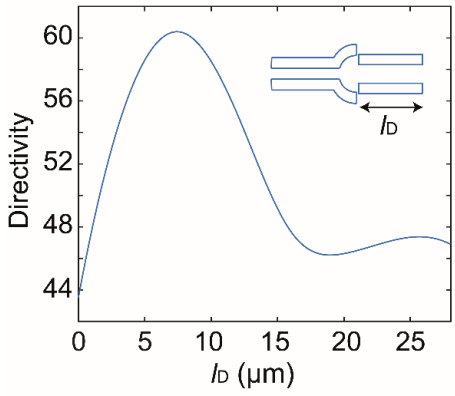

Figure S3. Influence of l_D on the directivity. The maximum value is achieved for $l_D \approx 7$ µm.

We started by placing 4 directors with $l_{DP} = l_{DC} = 1$ µm in front of the antenna, yielding an arrangement with a global $l_{DMAX} = 7$ µm (see Figure S4a). This first configuration rendered a directivity (D) of 62, a slight improvement with respect to the optimal antenna + director system.

To further enhance this figure, we then focused on optimizing l_{DC} and l_{DP} in a one-cut configuration (depicted as the shaded area in Figure S4a) with a sequential procedure, optimizing one variable at a time and maintaining the same l_{DP} value for both directors. As a result of the multiple geometrical variables that can be simultaneously studied in a full-wave 3D optimization, we kept w_D = 0.18 µm and w_G = 0.34 µm from our previous analysis. Since the best improvement was achieved for l_{DP} = 1.5 µm and l_{DC} = 0 (resulting in a single 3-µm length director), we introduced an extra degree of freedom in the optimization area by adding a second cut at the output facet of the antenna, see shaded region in Figure S4b. A good trade-off was achieved with l_{DC1} = 0.5 µm, l_{DC2} = 0.2 µm and l_{DPF} = 0.8 µm, improving the directivity from the initial figure of 51 (structure within the green square in Figure S4a) to 57 (structure within the green square in Figure S4b). Once we determined the optimal value for this two-cut configuration, we analyzed the impact of adding the two extra directors with l_{DC} = 1 µm to achieve the initial 4-director scheme, yielding the final directivity of 71. The inclusion of additional directors hardly improved the directivity while increasing the final footprint. While the optimization of more geometrical variables might provide schemes with an enhanced directivity, we decided to keep the 4-director configuration of Figure S4b, since it largely outperformed previous plasmonic approaches

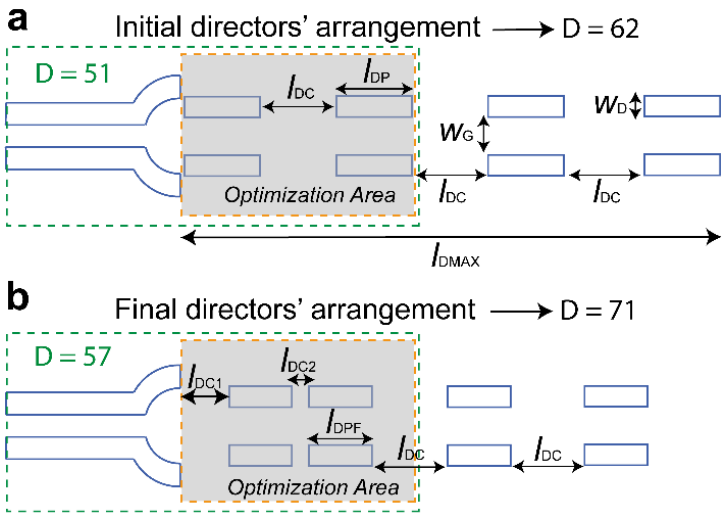

Figure S4. (**a**) Initial directors' arrangement that served as a basis from which starting the optimization. (**b**) Final configuration that includes the C-shaped antenna and 4 directors after the optimization procedure.

4. Figure of merit of the wireless interconnect

In order to assess the goodness of a given wireless interconnect and carry out a comparison as fair as possible, we have defined a simple figure of merit (FOM) that takes into account all the relevant features of an antenna, as explained below. For that purpose, the Friis transmission equation is used as a point of departure:

$$P_{RX} = P_{TX} G_{TX} G_{RX} \left(\frac{\lambda}{4\pi d} \right)^2$$

In addition to wavelength λ and link distance d (fixed parameters for a given application), this equation includes, through the gain of the transmitting and receiving antennas G_{TX} and G_{RX}, all the system parameters that determine the received power P_{RX} as a function of the transmitted power P_{TX} (radiation efficiency, reflection coefficient, polarization efficiency, directivity…). Since large gain values are desirable, the FOM of the system should be proportional to it. On the other hand, achieving a *compact design* is a desirable feature in photonic structures and thus the FOM should be inversely proportional to the footprint S (units of area) of the device. Finally, for the FOM to be dimensionless, length should be given in units of wavelength. As a result, we define the following expression for the FOM

$$\text{FOM} = 4\pi^{-2} \frac{G_{TX} G_{RX}}{S/\lambda^2} = \frac{\eta_P d^2}{S}$$

where $\eta_P = P_{RX}/P_{TX}$ (expressed in linear units). Note that the FOM only depends on antenna gain and footprint. Nonetheless, the use of Friis' equation allows us to rewrite it in terms of the experimentally measurable values η_P, d and S [the factor $(4\pi)^{-2}$ is introduced to simplify the final expression]. Using this formula, we can compare the performance of our wireless link with two of the most relevant previous works (Ref. 1 for being one of the few experimental works on plasmonic links, and Ref. 2 for providing the best power efficiency for a plasmonic link to date, to our knowledge). Their corresponding FOM, together with the one we obtained for our wireless interconnect are included in the following table:

	Reference 1	**Reference 2**	**Our design**
η_P **(dB)**	**-62**	**-40**	**-25.76**
d **(μm)**	**60**	**60**	**50**
S **(μm^2)**	**0.066**	**4.3**	**6.4**
FOM	**0.035**	**0.07**	**1.04**

Table S1. Figure of merit of our design versus other approaches.

The final footprint of our design may represent a drawback if we consider this value as an isolated figure from the rest of fundamental parameters that establish the goodness of any interconnect. However, despite having a larger footprint than that shown in previous plasmonic works, we discover a notably improved FOM as a result of the high gain values achieved with the designed antenna (not achievable so far via plasmonic approaches). Furthermore, it must be emphasized that the radiating systems of Ref. 1 require an off-chip nanoantenna excitation, feature which

hinders a future planar integration of this kind of system. Along this line, these plasmonic elements are not antennas in the sense of converting radiated waves into guided waves (or vice versa), but in the sense of reradiating incoming waves in another direction, which can be extremely useful, but for different applications from those of our proposal. Notably, our FOM was experimentally retrieved, in contrast to the previous on-chip wireless plasmonic approaches (those not requiring off-chip excitation), which just provided theoretical values.

5. Power efficiency of wireless versus plasmonic links

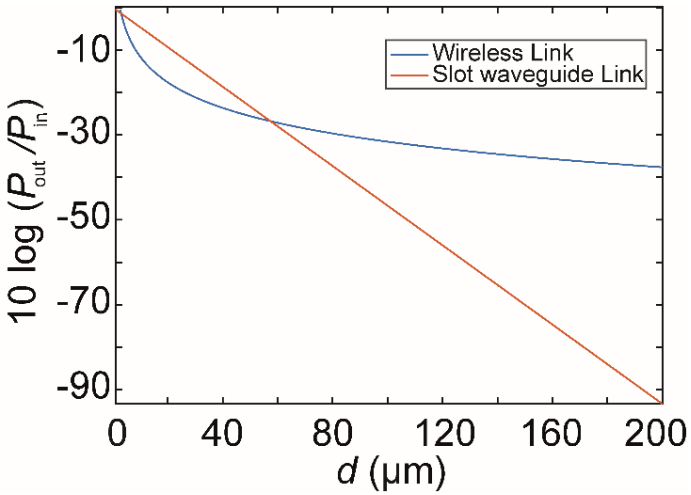

Figure S5. Comparison of the interconnect loss (expressed in dB) between a wireless link built upon the C-Antenna + 4 directors system and a straight plasmonic slot waveguide (w_D = 0.18 μm and w_G = 0.34 μm), as a function of the link distance *d*.

6. E-field distribution in the Si-Au-Si transition

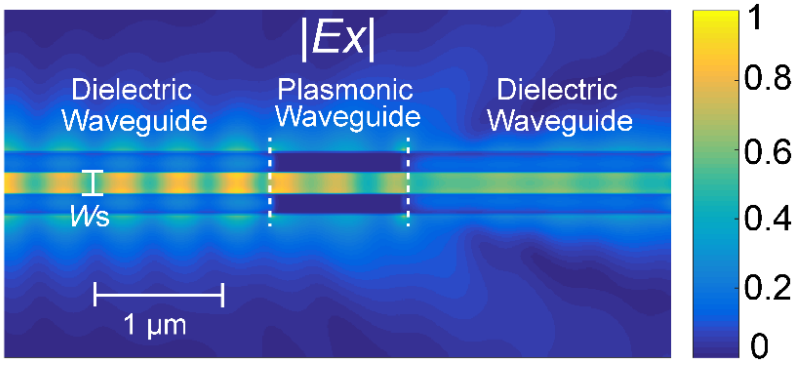

Figure S6.Top view of the E-field distribution (linear units) in the Si-Au-Si transition. Light is injected in the system from the left.

7. Experimental grating coupling efficiency

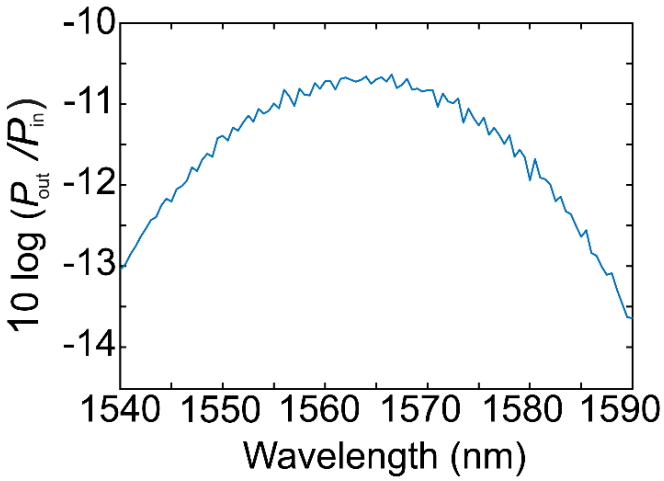

Figure S7. Grating coupling efficiency. Experimental measurements depicted in Figure 4 of the manuscript were normalized to the values here shown. This graph includes the combined loss of the input and output dielectric coupling sections of a wireless nanolink (excluding the plasmonic slot transitions and the silicon antennas).

8. Data transmission experimental test

A digital data transmission over a 20 μm-length wireless dielectric link was demonstrated using a commercial $LiNiBO_3$ modulator fed with a 40 Gbit·s^{-1} non-return to zero (NRZ) pseudo-random bit sequence (PRBS 2^{31}-1) delivered by a bit pattern generator (SHF BPG 44E), see Figure S8. The electrical signal of the BPG was amplified through a broad bandwidth driver amplifier (DC to 40 GHz) to achieve a voltage swing of ~5 V_{pp} and combined to a 1.7 V DC offset to ensure that the modulator is biased at quadrature. The input 40 Gbit·s^{-1} modulated signal was then coupled in and out the silicon chip (DUT) containing the wireless interconnect via grating couplers. The signal transmitted through the nanoantennas was then photodetected by a 40 GHz Digital Communication Analyzer (Infiniium DCA-J 86100C).

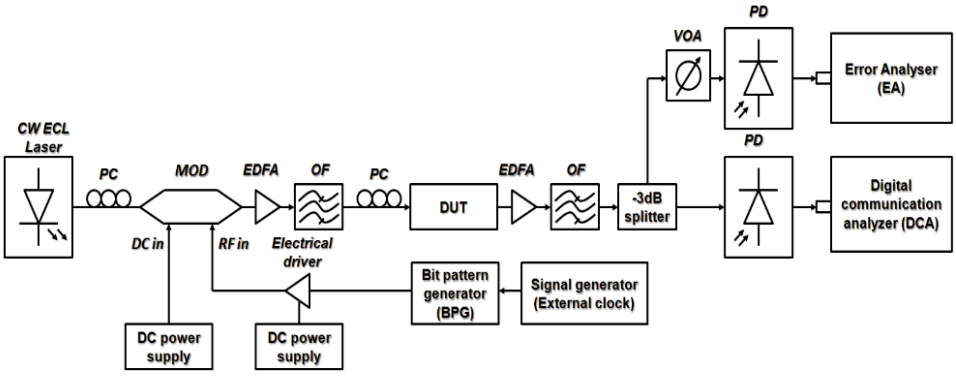

Figure S8. Experimental set-up for the data transmission test.

The bit-error rate (BER) was measured at an operation wavelength of λ = 1558.8 nm (injected into the system with a continuous wave laser, Yenista ECL-1560/P6) by a 75 GHz photodiode (PD) connected to an Error Analyzer (SHF EA 44) and evaluated as a function of the optical power received at the above-mentioned photodetector, see Figure S9. This BER value is

sufficiently low to rule out forward-error correction schemes often related to an increase in chip complexity. This promising on-chip wireless transmission performance together with the scalability of silicon photonics components, may enable sets of multiplexed wavelengths spanning 40 nm (1.6 nm wavelength separation) modulated by 40 Gbit·s^{-1} data streams to be transmitted over longer link distances, feature which potentially paves the way towards Tbit·s^{-1} on-chip optical communications (3).

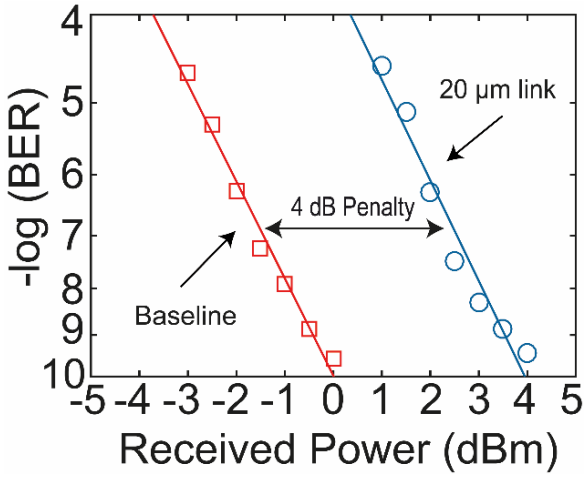

Figure S9. BER as a function of the received power at the photodetector. In order to evaluate the power penalty introduced by the wireless link, the BER in a baseline configuration (in which a straight silicon waveguide replaces the 20 μm-length nanolink) was measured, establishing the reference of the system. The 20 μm-length link showed a 4 dB penalty with respect to the baseline configuration. We achieved a $1 \cdot 10^{-9}$ BER, meaning that only 1 out of 10^9 bits was sent with errors.

References:

(1) Dregely, D.; Lindfors, K.; Lippitz, M.; Engheta, N.; Totzeck, M.; Giessen, H. Imaging and steering an optical wireless nanoantenna link. *Nat. Commun*. **2014**, 5, 4354.

(2) Yang, Y.; Li Q.; Qiu, M. Broadband nanophotonic wireless links and networks using on-chip integrated plasmonic antennas. *Sci. Rep*. **2016**, 6, 19490.

(3) Doany, F. E.; Schow, C. L.; Lee, B. G.; Budd, R.; Baks, C.; Libsch, F. L.; Carver, C.; Jianzhuang, H.; Bajkowski, D. *Electronic Components and Technology Conference (ECTC)*. **2011**, 790.

Chapter 4

General discussion and conclusions

Taking as a reference some pioneering works on plasmonic nanoantennas [15–25], this thesis was initially conceived as a study of the possibilities offered by on-chip wireless devices and their potential applications to implement interconnects at the nanoscale. As already explained in Chapter 1, the use of plasmonic-based nanoantennas was a solution to overcome the limiting losses of metallic wires, usually employed to interconnect the different parts and devices at the photonic layer. Studying more in depth the literature, we realized that while it is true that plasmonic nanoantennas have a better performance than metallic waveguides, they still have a poor behavior when acting as radiating elements. In this sense, plasmonic nanoantennas present limited figures in terms of directivity and radiation efficiency, leading us to explore other alternatives, specifically, focusing on the use of waveguide-based silicon antennas. These dielectric structures have proved to be key building blocks from which experimentally demonstrating a series of applications hardly achievable via previous wired or wireless approaches. Thanks to this, we have contributed to the evolution of not only nanoscale communications but also to the development of new lab-on-a-chip biosensors, as well as to the implementation of novel interfaces for plasmonic systems. In the next lines, we specify and assess the main achievements of these years of work together with some remaining challenges.

Within the field of optical communications, the major highlight of this thesis is the creation of an on-chip wireless platform based on the use of silicon antennas able to provide a total electromagnetic control over radiated fields. Thanks to this platform, we were able to experimentally demonstrate for the first time an on-chip wireless photonic link, transmitting data streams with a bit rate as high as 160 $Gbit \cdot s^{-1}$ over mm-scales. These results spark the possibility of attaining terabit-per-second communications by using wavelength multiplexing, and expanded

the flexibility within the scope of on- and inter-chip networks. Moreover, we implemented the first electrically-tunable on-chip beam steering device and its application to achieve reconfigurable pathways for fast, energy-efficient, and low-cross-talk switching, showing the potential of our approach for future optical reconfigurable networks. Furthermore, thanks to the ability of the nanoantennas to enable interferenceless crossing paths, we experimentally developed a 12-port wireless crossing device, with an extremely improved performance in terms of crosstalk with respect to guided multiport versions. Finally, in order to show the total control over radiated beams that can be achieved via antenna-based schemes, we theoretically developed a device able to generate reconfigurable tailor-made electromagnetic spots. This kind of device, which might be used for communication purposes, additionally opens the door to on-chip 2D-space mapping, 2D-selective optical detection schemes (as opposed to the 1D-selective capacities of beam-steering devices) and the capacity of radiating behind "obstacles".

The importance of these results collected in PAPER A was pointed out in the journal *Nature Photonics* (Pile DFP. *Nat. Photon*. **11**, 684 (2017)) **as a research highlight**. In the article it is stated that 'Carlos García-Meca, Sergio Lechago and colleagues from the Universitat Politècnica de València in Spain have done away with conventional interconnecting waveguides, demonstrating reconfigurable 'optical wireless' links between ports on an integrated optical chip'.

The study of integrated on-chip biodevices occupied an important part in the development of this dissertation. Here, our main achievement was the demonstration of a label-free micro-optofluidic on-chip cytometer, exhibiting an unprecedented combination of SNR and an ultra-compact footprint. Particularly, in PAPER B, we optimized the wireless optical subsystem with respect to the previous design in PAPER A, achieving SNR figures able to compete with the best on-chip designs realized so far —typically with a much less compact size. On the other hand, the needle-like beams radiated by the proposed nanoantennas allowed a state-of-the-art sub-micron resolution, feature which avoids the widespread use of bulky elements to collimate light within the chip, such as fibers or lenses. Thanks to the ultra-compact antenna size, with a cross section in the nm-scale, a dramatic reduction in the final footprint of the optical system (several orders of magnitude with respect to previous designs) is obtained, from the mm-scale to the μm-scale. This feature, together with the use of a fully-integrated CMOS compatible approach and a top class device performance, entails two main advantages:

- A notable reduction in the fabrication expenses, assuring a cost-effective mass-producible LOC model.

- The possibility of retrieving a significantly larger amount of detailed target information (via the implementation of several optical stages) and of performing a higher number of simultaneous analyses of multiple samples in a single chip.

Consequently, the results reported in this work are a considerable leap forward towards the development and universalization of flow cytometry, with a direct impact on biological, chemical and medical applications, such as point-of-care early diagnostics and mass screening for different diseases. As a final comment, we would like to highlight that **the results of PAPER B were recognized with an Editor's pick selection in the journal *Optics Express***.

The final part of this work dealt with the possibility of creating more advanced devices at the nanoscale by interfacing on-chip optical nanoantennas with plasmonic systems. So far, this work had focused on all-dielectric wireless structures using silicon as the basic constituent material. While it is true that plasmonics presents unavoidable shortcomings for far-field wireless implementations, it is nonetheless true that this field has ultimately given room to the development of spectroscopy or near-field microscopy, as well as to new ultra-compact devices such as modulators or detectors for ultra-fast nanoscale communications. Those were strong reasons that led us to try to combine these two platforms (wireless silicon photonics and plasmonics) in an efficient way. In PAPER C, taking advantage of a new class of slot-waveguide-based silicon nanoantenna, we experimentally demonstrate the first hybrid plasmonic-dielectric link for long-reach on-chip communications. Thanks to the geometry of the proposed antennas, we were able to directly and efficiently couple them to plasmonic slotted waveguides, thus avoiding complex transition structures to produce the aforementioned coupling. By doing this, we enable a hybrid dielectric-plasmonic system able to put together the advantages of high-performance wireless schemes for long-reach on-chip communications, beam-shaping tailoring or lab-on-a-chip sensors, with the advantages of plasmonic structures for nanoscale light manipulation and concentration. With this kind of scheme, we propose to shift the solely plasmonic paradigm into smartly-engineered dielectric-plasmonic configurations. **The potential impact of these results was highlighted in the journal *ACS Photonics*, with our paper being chosen as the front cover of the 2019 May issue.**

As future work, we would like to pay attention to some important challenges. For instance, our current efforts are aimed at carrying out the experimental demonstration of the beam-focusing device that was theoretically set out in PAPER A. Other challenging questions to be explored in reconfigurable systems would be the implementation of the amplitude control for nanoantenna arrays to enable an even more advanced beam pattern generation, or the possibility of taming optical forces at the nanoscale with tweezing-like applications [12–14]. Furthermore, since we have witnessed an increasing interest in the development of applications based on the use of metasurfaces [94, 95] or those working in the microwave band [96] (the so-called microwave photonics) as well as in the mid-infrared [97], we want to explore the

possibilities offered by on-chip wireless silicon photonics in these areas. Those are emerging and appealing research lines on which to work in the near future within the frame of wireless integrated architectures.

With respect to the field of integrated biodevices, we focused this thesis on the development of wireless microflow cytometers, but other interesting approaches such as dynamic light scattering, Raman spectroscopy and gas chromatography might be boosted using our results as a basis in the scope of lab-on-a-chip devices. On the other hand, while it is true that the use of the SOI platform assures a mass production of these devices, it is also clear that major advances in the miniaturization of on-chip light sources and detectors, as well as the microfluidics of future biochips, is still necessary to enable the universalization of low-cost point-of-care applications. In this sense, major efforts must be done to provide marketable products among the public at large, by basically improving the strategies of chip packaging as well as the development of the required control/processing electronics and of the appropriate application-specific classification algorithms to quickly retrieve the required data for biomedical purposes.

Bibliography

1. Kirchain R and Kimerling L. A roadmap for nanophotonics. *Nat. Photon.* **1**, 303–305 (2007).

2. Yu R, Cheung S, Li Y, Okamoto K, Proietti R, Yin Y and Yoo SJB. A scalable silicon photonic chip-scale optical switch for high performance computing systems. *Opt. Express* **21**, 32655–32667 (2013).

3. Haurylau M, Chen G, Chen H, Zhang J, Nelson NA, Albonesi DH, Friedman EG, and Fauchet PM. On-chip optical interconnect roadmap: challenges and critical directions. *IEEE J. Select. Top Quantum. Electron.* **12**, 1699–1705 (2006).

4. Chan JN, Hendry G, Biberman A and Bergman K. Architectural exploration of chip-scale photonic interconnection network designs using physical-layer analysis. *J. Lightw. Technol.* **28**, 1305–1315 (2010).

5. Subbaraman H, Xu X, Hosseini A, Zhang X, Zhang Y, Kwong D and Chen RT. Recent advances in silicon-based passive and active optical interconnects. *Opt. Express* **23**, 2487–2511 (2015).

6. Chrostowski L and Iniewski K. *High-Speed Photonics Interconnects*. Boca Raton: USA, CRC Press (2017).

7. Fan XD and White IM. Optofluidic microsystems for chemical and biological analysis. *Nat. Photon.* **5**, 591–597 (2011).

8. Lee BG, Rylyakov AV, Green WMJ, Assefa S, Baks CW, Rimolo-Donadio R, Kuchta DM, Khater MH, Barwicz T, Reinholm C, Kiewra E, Shank SM, Schow CL and Vlasov YA. Monolithic silicon integration of scaled photonic switch fabrics, CMOS logic, and device driver circuits. *J. Lightw. Technol.* **32**, 743–751 (2014).

9. Condrat C, Kalla P and Blair S. Crossing-aware channel routing for integrated optics. *IEEE Trans. Comput-Aided Design Integr. Circuits Syst.* **33**, 814–825 (2014).

10. Robinson JP and Roederer M. Flow cytometry strikes gold. *Science* **350**, 739–740 (2015).

11. Schurr JM. Dynamic light scattering of biopolymers and biocolloids. *CRC Crit. Rev. Biochem.* **4**, 371–431 (1977).

12. Righini M, Volpe G, Girard C, Petrov D and Quidant R. Surface plasmon optical tweezers: tunable optical manipulation in the femtonewton range. *Phys. Rev. Lett.* **100**, 186804 (2008).

13. Padgett M and Bowman R. Tweezers with a twist. *Nat. Photon.* **5**, 343–348 (2011).

14. Juan ML, Righini M and Quidant R. Plasmon nano-optical tweezers. Nat. Photon. **5**, 349–356 (2011).

15. Alù A and Engheta N. A hertzian plasmonic nanodimer as an efficient optical nanoantenna. *Phys. Rev. B.* **78**, 195111 (2008).

16. Polman A. Plasmonics applied. *Science* **322**, 868–869 (2008).

17. Brongersma ML. Plasmonics: Engineering optical antennas. *Nat. Photon.* **2**, 270–272 (2008).

18. Fischer H and Martin OJF. Engineering the optical response of plasmonic nanoantennas. *Opt. Express* **16**, 9144–9154 (2008).

19. Bharadwaj P, Deutsch B and Novotny L. Optical Antennas. *Adv. Opt. Photon.* **1**, 438–483 (2009).

20. Alù A and Engheta N. Wireless at the nanoscale: optical interconnects using matched nanoantennas. *Phys. Rev. Lett.* **104**, 213902 (2010).

21. Novotny L and van Hulst N. Antennas for light. *Nat. Photon.* **5**, 83–90 (2011).

22. Ni X, Emani NK, Kildishev AV, Boltasseva A and Shalaev VM. Broadband Light Bending with Plasmonic Nanoantennas. *Science* **335**, 427 (2012).

23. Dregely D, Lindfors K, Lippitz M, Engheta N, Totzeck M and Giessen H. Imaging and steering an optical wireless nanoantenna link. *Nat. Commun.* **5**, 4354 (2014).

24. Koenderink AF, Alù A and Polman A. Nanophotonics: Shrinking light-based technology. *Science* **348**, 516-521 (2015).

25. Yang Y, Li Q and Qiu M. Broadband nanophotonic wireless links and networks using on-chip integrated plasmonic antennas. *Sci. Rep.* **6**, 19490 (2016).

26. Krasnok AE, Miroshnichenko AE, Belov PA and Kivshar YS. All-dielectric optical nanoantennas. *Opt. Express* **20**, 20599–20604 (2012).

27. Filonov DS, Krasnok AE, Slobozhanyuk AP, Kapitanova PV, Nenasheva EA, Kivshar YS and Belov PA. Experimental verification of the concept of all-dielectric nanoantennas. *Appl. Phys. Lett.* **100**, 201113 (2012).

28. Van Acoleyen K, Bogaerts W, Jágerská J, Le Thomas N, Houdré R and Baets R. Off-chip beam steering with a one-dimensional optical phased array on silicon-on-insulator. *Opt. Lett.* **34**, 1477–1479 (2009).

29. Van Acoleyen K, Rogier H and Baets R. Two-dimensional Optical Phased Array Antenna on Silicon-On-Insulator. *Opt. Express.* **23**, 13655–13660 (2010).

30. Sun J, Timurdogan E, Yaacobi A, Hosseini ES and Watts MR. Large-scale nanophotonic phased array. *Nature* **493**, 195–199 (2013).

31. Moore GE. Cramming more components onto integrated circuits. *Electronics* **38**, 114–117 (1965).

32. Waldrop MM. More than Moore. *Nature* **530**, 145–147 (2016).

33. Thomson D, Zilkie A, Bowers JE, Komljenovic T, Reed GT, Vivien L, Marris-Morini D, Cassan E, Virot L, Fédéli JM, Hartmann JM, Schmid JH, Xu DX, Boeuf F, O'Brien P, Mashanovich GZ and Nedeljkovic M. Roadmap on silicon photonics. *J. Opt.* **18**, 073003 (2016).

34. Zhu W, Esteban R, Borisov AG, Baumberg JJ, Nordlander P, Lezec HJ, Aizpurua J and Crozier KB. Quantum mechanical effects in plasmonic structures with subnanometre gaps. *Nat. Commun.* **7**, 11495 (2016).

35. Fitzgerald JM, Narang P, Craster RV, Maier SA, and Giannini V. Quantum Plasmonics. *Proc. IEEE* **104**, 1–16 (2016).

36. Soref RA. Single-crystal silicon: a new material for 1.3 and 1.6 μm integrated-optical components. *Electron. Lett.* **21**, 953–954 (1985).

37. Soref RA. Electrooptical effects in silicon. *IEEE J. Quantum Electron.* **23**, 123–129 (1987).

38. Xu Q, Schmidt B, Pradhan S and Lipson M. Micrometre-scale silicon electro-optic modulator. *Nature* **435**, 325–327 (2005).

39. Cui KY, Zhao Q, Feng X, Liu F, Huang Y and Zhang W. Ultra-compact and broadband 1×4 thermo-optic switch based on W2 photonic crystal waveguides. *Proceedings of 2005 Opto-Electronics and Communications Conference*; IEEE: Shanghai (2005).

40. Chu T, Yamada H, Ishida S and Arakawa Y. Compact 1 × N thermo-optic switches based on silicon photonic wire waveguides. *Opt. Express* **13**, 10109–10114 (2005).

41. Tanabe T, Nishiguchi K, Kuramochi E and Notomi M. Low power and fast electro-optic silicon modulator with lateral p-i-n embedded photonic crystal nanocavity. *Opt. Express* **17**, 22505–22513 (2009).

42. Wang WJ, Zhao Y, Zhou H, Hao Y, Yang J, Wang M and Jiang X. CMOS-Compatible 1 × 3 silicon electrooptic switch with low crosstalk. *IEEE Photon. Technol. Lett.* **23**, 751–753 (2011).

43. Coppola G, Sirleto L, Rendina I and Iodice M. Advance in thermo-optical switches: principles, material, design, and device structure. *Opt. Eng.* **50**, 071112 (2011).

44. Watts MR, Sun J, DeRose C, Trotter DC, Young RW and Nielson GN. Adiabatic thermo-optic Mach-Zehnder switch. *Opt. Lett.* **38**, 733–735 (2013).

45. Li X, Xu H, Xiao X, Li Z, Yu Y and Yu J. Fast and efficient silicon thermo-optic switching base on reverse breakdown of pn junction. *Opt. Lett.* **39**, 751–753 (2014).

46. Bogaerts W, Dumon P, Taillaert D, Wiaux V, Beckx S, Luyssaert B, Van Campenhout J, Van Thourhout D and Baets R. SOI nanophotonic waveguide structures fabricated with deep UV lithography. *Photonics and Nanostructures - Fundamentals and Applications* **2**, 81–86 (2004).

47. Baets R, Dumon P, Bogaerts W, Roelkens G, Taillaert D, Luyssaert B, Priem G, Morthier G, Bienstman P and Van Thourhout D. Silicon-on-insulator based nano-photonics: Why, How, What for?. *2nd IEEE International Conference Group IV Photonics* IEEE, 168–170 (2005).

48. Soref RA. The Past, Present, and Future of Silicon Photonics. *IEEE J. Quantum. Electron.* **12**, 1678–1687 (2006).

49. Voelkel R. Wafer-scale micro-optics fabrication. *Adv. Opt. Technol.* **1**, 135–150 (2012).

50. Kononchuk O and Nguyen BY. *Silicon-on-insulator (SOI) technology: Manufacture and applications*. Amsterdam: The Netherlands, Elsevier (2014).

51. Van Zant P. *Microchip Fabrication: A Practical Guide to Semiconductor Processing*. New York: USA, McGraw Hill Education (2014).

52. Dai D, Bauters J and Bowers JE. Passive technologies for future large-scale photonic integrated circuits on silicon: polarization handling, light non-reciprocity and loss reduction. *Light Sci. Appl.* **1**, e1 (2012).

53. Zhuang LM, Roeloffzen CGH, Meijerink A, Burla M, Marpaung DAI, Leinse A, Hoekman M, Heideman RG and van Etten W. Novel ring resonator-based integrated photonic beamformer for broadband phased array receive antennas—Part II: experimental prototype. *J. Lightw. Technol.* **28**, 19–31 (2010).

54. Bogaerts W, DeHeyn P, Van Vaerenbergh T, DeVos K, Selvaraja SK, Claes T, Dumon P, Bienstman P, VanThourhout D and Baets R. Silicon microring resonators. *Laser Photon. Rev.* **6**, 47–73 (2012).

55. Sanchis P, Villalba P, Cuesta F, Håkansson A, Griol A, Galán JV, Brimont A and Martí J. Highly efficient crossing structure for silicon-on-insulator waveguides. *Opt. Lett*. **34**, 2760–2762 (2009).

56. Ma Y, Zhang Y, Yang S, Novack A, Ding R, Eu-Jin Lim A, Lo GQ, Baehr-Jones T and Hochberg M. Ultralow loss single layer submicron silicon waveguide crossing for SOI optical interconnect. *Opt. Express* **21**, 29374–29382 (2013).

57. Akihama Y and Hane K. Single and multiple optical switches that use freestanding silicon nanowire waveguide couplers. *Light Sci. Appl.* **1**, e16 (2012).

58. Lu Z, Yun H, Wang Y, Chen Z, Zhang F, Jaeger NAF and Chrostowski L. Broadband silicon photonic directional coupler using asymmetric-waveguide based phase control. *Opt. Express* **23**, 3795–3808 (2015).

59. Psaltis D, Quake SR and Yang C. Developing optofluidic technology through the fusion of microfluidics and optics. *Nature* 442, 381–386 (2006).

60. Mao XL, Nawaz AA, Lin SC, Lapsley MI, Zhao Y, McCoy JP, El-Deiry WS and Huang TJ . An integrated, multiparametric flow cytometry chip using "microfluidic drifting" based three-dimensional hydrodynamic focusing. *Biomicrofluidics* **6**, 024113 (2012).

61. Huang NT, Zhang HL, Chung MT, Seo JH and Kurabayashi K. Recent advancements in optofluidics-based single-cell analysis: optical on-chip cellular manipulation, treatment, and property detection. *Lab Chip* 14, 1230–1245 (2014).

62. Blasi T, Hennig H, Summers HD, Theis FJ, Cerveira J, Patterson JO, Davies D, Filby A, Carpenter AE and Rees P. Label-free cell cycle analysis for high-throughput imaging flow cytometry. *Nat. Comms.* **7**, 10256 (2015).

63. Zhang YS, Watts BR, Guo T, Zhang Z, Xu C and Fang Q. Optofluidic device based microflow cytometers for particle/cell detection: a review. *Micromachines* **7**, 70 (2016).

64. García-Meca C, Lechago S, Brimont A, Griol A, Mas S, Sánchez L, Bellieres L, Losilla NS and Martí J. On-chip wireless silicon photonics: from reconfigurable interconnects to lab-on-chip devices. *Light Sci. Appl.* **6**, e17053 (2017).

65. Lechago S, García-Meca C, Sánchez-Losilla N, Griol A and Martí J. High signal-to-noise ratio ultra-compact lab-on-a-chip microflow cytometer enabled by silicon optical antennas. *Opt. Express* **26**, 25645–25656 (2018).

66. Lechago S, García-Meca C, Griol A, Kovylina M, Bellieres L and Martí J. All-Silicon on-chip optical nanoantennas as efficient interfaces for plasmonic devices. *ACS Photon.* **6**, 1094–1099 (2019).

67. Melati D, Morichetti F, Gentili GG and Melloni A. Optical radiative crosstalk in integrated photonic waveguides. *Opt. Lett.* **39**, 3982–3985 (2014).

68. Song WW, Gatdula R, Abbaslou S, Lu M, Stein A, Lai WY-C, Provine J, Pease RFW, Christodoulides DN and Jiang W. High-density waveguide superlattices with low crosstalk. *Nat. Commun.* **6**, 7027 (2015).

69. Potcoava MC, Futia GL, Aughenbaugh J, Schlaepfer IR, Gibson EA. Raman and coherent anti-Stokes Raman scattering microscopy studies of changes in lipid content and composition in hormone-treated breast and prostate cancer cells. *J. Biomed. Opt.* **19**, 111605 (2014).

70. Zhao Y, Engheta N and Alù A. Effects of shape and loading of optical nanoantennas on their sensitivity and radiation properties. *J. Opt. Soc. Am.* **28**, 1266–1274 (2011).

71. Balanis CA. *Antenna Theory: Analysis and Design*. New York: USA, Wiley (1982).

72. Raether H. *Surface Plasmons on Smooth Surfaces*. New York: USA, Springer-Verlag (1988).

73. Barnes WL, Dereux A and Ebbesen TW. Surface plasmon subwavelength optics. *Nature* **424**, 824–830 (2003).

74. Zayats AV, Smolyaninov II, Maradudin AA. Nano-optics of surface plasmon polaritons. *Phys. Rep.* **408**, 131–314 (2005).

75. Pitarke JM, Silkin VM, Chulkov EV and Echenique PM. Theory of surface plasmons and surface-plasmon polaritons. *Rep. Progr. Phys.* **70**, 1–87 (2007).

76. Maier SA. *Plasmonics: Fundamentals and Applications*. New York: USA, Springer-Verlag (2007).

77. Brongersma ML and Shalaev VM. The Case for Plasmonics. *Science* **328**, 440−441 (2010).

78. Mie G. Beiträge zur Optik trüber Medien, speziell kolloidaler Metallösungen. *Ann. Phys.* **25**, 377−445 (1908).

79. Zhao Q, Zhou J, Zhang F and Lippens D. Mie resonance-based dielectric metamaterials. *Mat. Today* **12**, 60−69 (2009)**.**

80. Ritchie RH. Plasma Losses by Fast Electrons in Thin Films. *Phys. Rev.* **106**, 874 (1957).

81. Maier SA, Brongersma ML, Kik PG, Meltzer S, Requicha AAG and Atwater HA. Plasmonics−A Route to Nanoscale Optical Devices. *Adv. Mater.* **13**, (2001).

82. Haffner C, Heni W, Fedoryshyn Y, Niegemann J, Melikyan A, Elder DL, Baeuerle B, Salamin Y, Josten A, Koch U, Hoessbacher C, Ducry F, Juchli L, Emboras A, Hillerkuss D, Kohl M, Dalton LR, Hafner C and Leuthold J. All-plasmonic Mach–Zehnder modulator enabling optical high-speed communication at the microscale. *Nat. Photon.* **9**, 525−528 (2015).

83. Roh S, Chung T and Lee B. Overview of the Characteristics of Micro- and Nano-Structured Surface Plasmon Resonance Sensors. *Sensors*, **11**, 1565−1588 (2011).

84. Tong L, Wei H, Zhang S and Xu H. Recent Advances in Plasmonic Sensors. *Sensors*, **14**, 7959−7973 (2014).

85. Mock JJ, Smith DR and Schultz S. Local Refractive Index Dependence of Plasmon Resonance Spectra from Individual Nanoparticles. *Nano Lett.* **3**, 485−491 (2003).

86. Novotny L and Stranick SJ. Near-field optical microscopy and spectroscopy with pointed probes. *Annu. Rev. Phys. Chem.* **57**, 303−331 (2006).

87. Hammond JL, Bhalla N, Rafiee SD and Estrela P. Localized Surface Plasmon Resonance as a Biosensing Platform for Developing Countries. *Biosensors*, **4**, 172−188 (2014).

88. Rothenhäusler B and Knoll W. Surface-plasmon microscopy. *Nature*, **332**, 615–617 (1988).

89. 145-2013 - IEEE Standard for Definitions of Terms for Antennas. DOI: *10.1109/IEEESTD.2014.6758443* (2013).

90. Cardama A, Jofre L, Rius JM, Romeu J, Blanch S and Ferrando M. Antenas. Barcelona: España, Edicions UPC, (2002).

91. Cocorullo G, Della Corte FG, Rendina I and Sarro PM. Thermo-optic effect exploitation in silicon microstructures. *Sens. Actuators A Phys.***71**, 19−26 (1998)

92. Della Corte FG, Esposito-Montefusco M, Moretti L, Rendina I and Cocorullo G. Temperature dependence analysis of the thermo-optic effect in silicon by single and double oscillator models. *J. Appl. Phys.* **88**, 7115−7119 (2000).

93. Komma J, Schwarz C, Hofmann G, Heinert D and Nawrodt R. Thermo-optic coefficient of silicon at 1550 nm and cryogenic temperatures. *Appl. Phys. Lett.* **101**, 041905 (2012).

94. Kildishev AV, Boltasseva A and Shalaev VM. Planar Photonics with Metasurfaces. *Science* **339**, 1289−1295 (2013).

95. Yu NF and Capasso F. Flat optics with designer metasurfaces. *Nat. Mater.* **13**, 139−150 (2014).

96. Zhang W and Yao J. Silicon-Based Integrated Microwave Photonics. *IEEE J. Quantum Electron.* **52**, 0600412, (2016).

97. Soref RA. Mid-infrared photonics in silicon and germanium. *Nat. Photon.* **4**, 495–497 (2010).

Peer-reviewed publications

Main contributions

- **[PAPER A]** Carlos García-Meca[1], Sergio Lechago[1], Antoine Brimont, Amadeu Griol, Sara Mas, Luis Sánchez, Laurent Bellieres, Nuria S. Losilla and Javier Martí. 'On-chip wireless silicon photonics: From Reconfigurable Interconnects to Lab-on-Chip Devices', *Nature's Light Sci. Appl.* **6**, e17053 (2017). (**RESEARCH HIGHLIGHT**: *Nature Photonics* **11**, 684 (2017)).

- **[PAPER B]** Sergio Lechago, Carlos García-Meca, Amadeu Griol, Nuria S. Losilla and Javier Martí. 'High signal-to-noise ratio ultra-compact lab-on-a-chip microflow cytometer enabled by silicon optical antennas'. *Opt. Express* **26**, 25645–25656 (2018). (**JOURNAL EDITOR'S PICK**).

- **[PAPER C]** Sergio Lechago, Carlos García-Meca, Amadeu Griol, Miroslavna Kovylina, Laurent Bellieres and Javier Martí. 'All-Silicon On-chip Optical Nanoantennas As Efficient Interfaces for Plasmonic Devices'. *ACS Photon.* **6**, 1094–1099 (2019). (**FRONT COVER OF MAY 2019**).

Other contributions

- [PAPER D1] S. Mas, J. Palací, P. Pérez-Millán, S. Lechago, D. Monzón-Hernández and J. Martí. 'All-fiber processing of terahertz-bandwidth signals based on cascaded tapered fibers' *Opt. Lett.* **38**, 4954–4957 (2013).

- [PAPER D2] L. Sánchez, A. Griol, S. Lechago, A. Brimont and P. Sanchis. 'Low-Power Operation in a Silicon Switch Based on an Asymmetric Mach-Zehnder Interferometer' *IEEE Photon. Journal* **7**, 6900308 (2015).

- [PAPER D3] L. Sánchez, S. Lechago and P. Sanchis. 'Ultra-compact TE and TM pass polarizers based on vanadium dioxide on silicon' *Opt. Lett.* **40**, 1452–1455 (2015).

[1] These authors contributed equally to this work

- [PAPER D4] L. Sánchez, S. Lechago, A.M. Gutiérrez-Campo and P. Sanchis. 'Analysis and design optimization of a hybrid VO2/Silicon 2 × 2 microring switch' *IEEE Photon. Journal* **8**, 7802709 (2016).

- [PAPER D5] F.J. Díaz-Fernández, E. Pinilla-Cienfugos, C. García-Meca, S. Lechago, A. Griol and J. Martí. 'Characterisation of on-chip wireless interconnects based on silicon nanoantennas via near-field scanning optical microscopy' *IET Optoelectron.* **13**, 72–76 (2018).

Conferences

Main contributions

- **[CONF A]** Sergio Lechago, Carlos García-Meca, Amadeu Griol and Javier Martí. 'Controlling on-chip optical radiation with all-dielectric antennas: reconfigurable interconnects and lab-on-a-chip devices' *Nanophotonics and Micro/Nano Optics International Conference (NANOP 2017)*, Barcelona, Spain. (**Oral Contribution**).

- **[CONF B]** Sergio Lechago, Carlos García-Meca and Javier Martí. 'All-Dielectric antennas enabling wireless silicon photonics' *X Reunión del Grupo Especializado de Física del Estado Sólido (GEFES 2018)*, Valencia, Spain. (**Oral Contribution**).

- **[CONF C]** Sergio Lechago, Carlos García-Meca and Javier Martí. 'Ultra-compact label-free silicon-nanoantenna-based optofluidic microflow cytometer with a high signal-to-noise ratio' *20th European Conference on Integrated Optics (ECIO 2018)*, Valencia, Spain. (**Oral Contribution**).

- **[CONF D]** Sergio Lechago, Carlos García-Meca and Javier Martí. 'Photonic Integrated Wireless Systems: A new platform enabled by silicon nanoantennas' *European Physics Conference (EPC 2018)* Valencia, Spain. (**Keynote Speaker**).

- **[CONF E]** Sergio Lechago, Carlos García-Meca and Javier Martí. 'Efficiently interfacing plasmonic devices via all-silicon on-chip optical nanoantennas' *Nanophotonics and Micro/Nano Optics International Conference (NANOP 2019)*, Munich, Germany. (**Accepted Oral Contribution**).

Other contributions

- [CONF E1] L. Sánchez, S. Lechago, A. Brimont and P. Sanchis. 'A silicon Mach Zehnder comb switch for low power operation in on-chip optical data communications' *SPIE Photonics Europe Conference 2014. Photonics, Optics, Lasers, Micro- and Nanotechnologies*, Brussels, Belgium.

- [CONF E2] J. Puche-Lara, S. Lechago, S. Petit, M.E. Gómez-Requena and J. Sahuquillo. 'Accurately Modeling a Photonic NoC in a Detailed CMP Simulation Framework' *International Conference on High Performance Computing & Simulation (HPCS 2016)* Innsbruck, Austria.

- [CONF E3] J. Puche-Lara, S. Lechago, S. Petit, M.E. Gómez-Requena and J. Sahuquillo. 'Modelado realista de una NoC fotónica en un entorno de simulación CMP detallado' *XXVII Jornadas de Paralelismo. Jornadas SARTECO 2016*, Salamanca, Spain.

- [CONF E4] M. Katevenis, N. Chrysos, M. Marazakis, I. Mavroidis, F. Chaix, N. Kallimanis, J. Navaridas, J. Goodacre, P. Vicini, A. Biagioni, P. S. Paolucci, A. Lonardo, E. Pastorelli, F. Lo Cicero, R. Ammendola, P. Hopton, P. Coates, G. Taffoni, S. Cozzini, M. Kersten, Y. Zhang, J. Sahuquillo, S. Lechago, C. Pinto, B. Lietzow, D. Everett, and G. Perna. 'The ExaNeSt Project: Interconnects, Storage, and Packaging for Exascale Systems' Euromicro Conference on Digital System Design (DSD 2016) Limassol, Cyprus.

- [CONF E5] F.J. Díaz-Fernández, E. Pinilla-Cienfuegos, C. García-Meca, S. Lechago, A. Griol and J. Martí. 'Near-Field Scanning Optical Microscope Measurements of On-Chip Wireless Interconnects Based on Silicon Nanoantennas' *X Reunión del Grupo Especializado de Física del Estado Sólido (GEFES 2018)*, Valencia, Spain.

- [CONF E6] F.J. Díaz-Fernández, E. Pinilla-Cienfuegos, C. García-Meca, S. Lechago, A. Griol and J. Martí. 'Characterization of On-Chip Wireless Interconnects Based on Silicon Nanoantennas via Near-Field Scanning Optical Microscopy' *20th European Conference on Integrated Optics (ECIO 2018)*, Valencia, Spain.